GROWTH AND CHARACTERIZATION OF III-NITRIDE MATERIALS FOR HIGH EFFICIENCY OPTOELECTRONIC DEVICES BY METALORGANIC CHEMICAL VAPOR DEPOSITION

A Dissertation

Presented to

The Academic Faculty

by

Suk Choi

Georgia Institute of Technology

December 2012

GROWTH AND CHARACTERIZATION OF III-NITRIDE MATERIALS FOR HIGH EFFICIENCY OPTOELECTRONIC DEVICES BY METALORGANIC CHEMICAL VAPOR DEPOSITION

Approved by:

Dr. Russell Dupuis, Advisor
School of Electrical and Computer Engineering
Georgia Institute of Technology

Dr. Paul A. Kohl
School of Chemical and Biomolecular Engineering
Georgia Institute of Technology

Dr. Bernard Kippelen
School of Electrical and Computer Engineering
Georgia Institute of Technology

Dr. Shyh-Chiang Shen
School of Electrical and Computer Engineering
Georgia Institute of Technology

Dr. Benjamin Klein
School of Electrical and Computer Engineering
Georgia Institute of Technology

Date Approved: August 23, 2012

ACKNOWLEDGEMENTS

I would like to express my sincerest gratitude to my advisors Dr. Russell Dupuis for providing the valuable opportunity in the field of MOCVD, and extending continuous encouragement, support, and guidance during this research. I am very proud of the fact that I was one of his students and I studied MOCVD in his research group.

I am thankful to my committee members, Dr. Kippelen, Dr. Klein, Dr. Kohl, and Dr. Shen for their very useful and valuable comments and suggestions. It is my honor to have your names on my thesis.

I want to thanks to past and current members of the Advanced Materials and Devices Group, Dr. Yong Huang, Dr. Jianping Liu, Zac Lochner, Jeomoh Kim, Mihee Ji, and Xiaohang Li for their help and cooperation in the research, and valuable friendship during my Ph.D student life. I will not forget Andrea Wympie, who was devoted to support every member of Advanced Materials and Devices Group (AMDG). I was also lucky to have the members of Dr. Shen's research group whom I have had the pleasure of working with: Tsung-Ting (Louis) Kao, Yi-Che (Steven) Lee, Bravishma Narayan, Cheng-Yin (Sam) Wang, and Yun Zhang.

I am very grateful to Dr. Jae-Hyun Ryou for being a great mentor, not only on research and study, but also on life, the universe, and everything. It was one of the most valuable experiences in my life to work with him.

I would like to thank my family for all of their support. I will never be able to thank my parents, Dr. Suk Doo Choi and Young-Soon Chung enough, because they gave me everything to be where I am today. I also thank my brother Seol Choi for his encouragement.

Finally, I owe much to my wife, Dr. Hee Jin Kim. It was a great pleasure and an inspiring experience to work with her at AMDG. She is a good colleague, a great researcher, and a lovely wife. Without her, I could never have done anything.

TABLE OF CONTENTS

LIST OF TABLES

LIST OF FIGURES

SUMMARY

During the last few decades, semiconductor optoelectronic devices such as light emitting diodes (LEDs), laser diodes (LDs), and photodiodes (PDs) have become of a great commercial success with their low energy consumption, long lifetime, environmental stability and compactness. Among the various candidate material systems for semiconductor optoelectronic devices in many applications, the Group III-nitride semiconductor system is the most promising as they have a direct- and wide-bandgap nature, high intrinsic carrier mobility, and the capability of forming heterostructures. With an increasing demand on the mass production of high-quality materials and device structures, metalorganic chemical vapor phase deposition (MOCVD) has been a dominant growth technology for both academic and industrial applications because of its versatility and scalability.

As a result of the lack of widely available bulk GaN (or AlN) substrates, III-nitride materials are often grown on foreign substrates whose lattice constants and thermal expansion coefficients show large mismatch relative to those of the III-nitride materials. However, the use of various foreign and native substrates in the epitaxial growth of the III-nitride semiconductors introduces several technical challenges that are generally not observed in other III-V semiconductors. The difference in the thermal conductivity and the thickness of the substrates results in the different temperature at the growing-surface that is a critical process parameter in determining the quality, composition, and the growth rate of the epitaxial layer. However, the prediction of the growing surface temperature is not very straightforward, because the surface temperature during the layer growth is a function of various parameters including the thermal conductivity of the substrate and the surface heat loss by forced convection that is a function of the chamber design and the flow rate of a carrier gas. An extensive study by using a finite-element method (FEM) calculation predicts that the use of different substrates under a high carrier-gas-flow environment can cause a significant growth-surface temperature difference to impact on the growth results of the AlGaN or InGaN layers. This prediction was

confirmed by the growth of AlN/AlGaN superlattices on bulk AlN substrates and an AlN/sapphire templates/substrates under the same growth conditions. The AlGaN layers grown on different substrates show an aluminum composition difference of 15%, indicating that the thermal properties of the substrates are an important factor in determining the growing-surface temperature.

In spite of the recent significant improvement in the emission efficiency of the Group III-nitride semiconductor based light-emitting diodes (LEDs), there are many technical challenges to be addressed in order for high-brightness and high-power LEDs to be competitive in the general-lighting field in terms of performance and manufacturing costs. One of the critical technical challenges for the LEDs to be competitive in terms of their performance and the cost is the reduction of efficiency droop. Among several suggested origins of the efficiency droop of III-N LEDs, the carrier spill-over theory is widely accepted by industry researchers as well as by academic investigators as the most convincing origin of the efficiency droop problem. The insertion of a wide-bandgap AlGaN material between the active region and the *p*-type hole-injection layer as an electron-blocking layer (EBL) is the most common technique to reduce the carrier spill-over phenomena. However, a typical AlGaN EBL (with x_{Al}~0.2) cannot provide a sufficient electron-confinement because of the polarization effect. Also, an AlGaN EBL may not be compatible with all visible LEDs because of its relatively high optimum growth temperature. Therefore, we have proposed and demonstrated $In_{0.19}Al_{0.81}N$ as an alternative high-quality EBL material for a higher electron-confinement effect with its lower growth temperature, wider bandgap, and lattice-matching capability to GaN.

The performance improvement by the InAlN EBL is confirmed by growing and comparing various blue LED structures without an EBL, with an $Al_{0.2}Ga_{0.8}N$ EBL, and with an $In_{0.19}Al_{0.81}N$ EBL. The electroluminescence (EL) measurement results showed that the LEDs with an $In_{0.19}Al_{0.81}N$ EBL show higher light output and much less efficiency droop than the LEDs without an EBL and the LEDs having a conventional $Al_{0.2}Ga_{0.8}N$ EBL. The performance enhancement of the LEDs with an $In_{0.19}Al_{0.81}N$ EBL over the LEDs with a conventional $Al_{0.2}Ga_{0.8}N$ EBL was over 30%, indicating that

the $In_{0.19}Al_{0.81}N$ EBL provides more effective electron-confinement and smaller carrier spill-over current.

However, the use of an $In_{0.19}Al_{0.81}N$ EBL leads to the formation of a high hole-blocking barrier in the valence band of the LED structure. The deficiency of the hole concentration in the active region is reported to be a major origin of the efficiency droop. Therefore, we analyzed the hole-blocking effect of the $In_{0.19}Al_{0.81}N$ EBL by using a quantum-efficiency model. For an analysis, the hole-blocking effect of the $In_{0.19}Al_{0.81}N$ EBL is controlled by changing the thickness of the $In_{0.19}Al_{0.81}N$ EBL. Blue LEDs with $In_{0.19}Al_{0.81}N$ EBLs with different thicknesses were grown and fabricated for quantum-efficiency comparisons. The quantum-efficiency vs. current density curves of the LEDs were analyzed by the "extended ABC model" to obtain the estimated spill-over current density and the hole density. The proposed model explained the observation of the highest quantum efficiency of the LEDs with a 15 nm $In_{0.19}Al_{0.81}N$ EBL as a result of low hole blocking effect of the 15 nm thick EBL. The observation also suggests that the hole-blocking effect is an important factor in realizing high light output and efficiency performance from LEDs operated at high current densities.

To enhance the hole-injection efficiency, a strain-engineered $In_xAl_{1-x}N$ EBL is proposed. The strain-engineered $In_xAl_{1-x}N$ EBL with indium composition higher than 19% has a reduced band bending because of the compensation of the overall polarization field by the piezoelectric polarization. As a result, the effective height of the electron-blocking barrier is maintained while the height of the hole-blocking barrier is decreased under a forward bias condition. The effect of the strain-engineered $In_xAl_{1-x}N$ EBL is examined by growing and measuring the LEDs with $In_xAl_{1-x}N$ EBLs with indium composition from 19% to 24%. The quantum-efficiency model was applied on the measured quantum-efficiency curves to analyze the hole-blocking effect of the strain-engineered $In_xAl_{1-x}N$ EBLs. The analysis results showed that the strain-engineered $In_xAl_{1-x}N$ EBL is effective in reducing the hole-blocking barrier. However, the light output of the LEDs with $In_xAl_{1-x}N$ EBLs with indium composition higher than 19% is observed to be lower than that of the LED with an $In_{0.19}Al_{0.81}N$ EBL

because of the lower electrical performance of the EBL grown at lower temperature. Therefore, an alternative growth condition for InAlN with high indium composition is necessary to demonstrate the performance enhancement of the LED with a strain-engineered $In_xAl_{1-x}N$ EBL.

Another strategy for improving the hole-injection efficiency is the compositional grading. The grading from the last InGaN QW to the $In_{0.19}Al_{0.81}N$ EBL will remove the sharp spike in the valence band at the active region – EBL interface, significantly improving the hole-injection efficiency. In the EL measurement results, the LEDs with a graded $In_{0.19}Al_{0.81}N$ EBLs show higher light output than the LEDs with an abrupt $In_{0.19}Al_{0.81}N$ EBL in spite of the greater thickness of the graded EBL. This result implies the compositionally graded EBL delivers a high improvement in terms of the hole-injection efficiency. However, more detailed and quantitative analysis on the effect of the compositionally graded $In_{0.19}Al_{0.81}N$ EBL on the hole injection and the electron-blocking effect is necessary.

Also, various EBL techniques can be combined each other for a further improvement in the LED performance. The employment of multiple EBL strategies may maximize their advantages while minimizing the drawbacks of each technique. Therefore, further study on the integration of the multiple EBL scheme is required.

CHAPTER 1 INTRODUCTION TO THE GROUP III-NITRIDE MATERIALS

1.1 Introduction

In the past ten years, semiconductor optoelectronic devices such as light emitting diodes (LEDs), laser diodes (LDs), and photodiodes (PDs) have had a great commercial success and dramatically improved performance. The enhanced output power and the high operation speed of semiconductor optoelectronic devices operating at a wavelength of 1.55 μm enables optical fiber communications with a transfer rate of several terabits per second. Short-wavelength LDs emitting at a blue-violet wavelength (405 nm) used with high-density optical media, such as Blu-ray discs, that provide high-definition movies and large-volume data storage. Visible LEDs are actively expanding their application into the area of display devices. LEDs have smaller size, higher energy efficiency, and longer lifetime compared to conventional light sources such as ultra-high-pressure (UHP) mercury lamps and cold-cathode fluorescent lamps (CCFLs). Especially, the white light produced by either a white-light LED or the combination of red, green, and blue LEDs has a higher color purity than that produced from conventional lamp light sources. These advantages of the visible LEDs enable energy-efficient and compact display devices with a wider color reproduction range. High-performance white-light LEDs are also expected to be used in general lighting applications in near the future, replacing incandescent bulbs and fluorescent lamps.

Among the various candidate material systems for the semiconductor optoelectronic devices, the Group III-nitride semiconductor system is the most promising as they have a direct- and wide-bandgap structure, intrinsic high carrier mobility, and the capability of forming heterostructures. The bandgap energy of the III-nitride semiconductors can be tunable from 0.78 eV to 6.23 eV by alloying AlN or InN with GaN. This range of bandgap energy covers wide wavelength from the deep ultraviolet (200 nm) to the infrared (1700 nm) region in addition to the entire visible spectral range.

Also, their superior thermal- and chemical-stability makes the III-nitride semiconductor-based devices attractive as high-voltage and high-temperature devices suitable for operating in hostile environments. For example, their superior radiation hardness over the narrow-bandgap semiconductors such as Si or GaAs allows the III-nitride semiconductors to be incorporated into the space applications.

1.2 Materials Properties

The III-nitride semiconductors have a tetrahedral atomic arrangement of. In the tetrahedral structure, each atom has four nearest neighbors occupying the vertices of a tetrahedron. GaN, AlN, or InN can have two alternative crystalline phases: a wurtzite phase and a zinc-blende phase. The wurtzite crystal structure consists of two interpenetrating hexagonal close packed sub-lattices, and each sub-lattice is shifted along the *c*-axis by 3/8 of its cell height. Also, the wurtzite structure belongs to the $P6_3mc$ space group. This group is consists of a 6-fold screw-axis along the *c*-axis, a mirror plane parallel to the *c*-axis and *a*-axis, and a glide plane along the *c*-axis. On the other hand, the zinc-blende cubic structure belongs to the $F\bar{4}3m$ space group that has the cubic F Bravais lattice and consists of a combined 4-fold inversion axis along the *c*-axis and 3-fold axis, and six mirror planes (tetrahedron symmetry). The III-nitride semiconductors usually take the wurtzite structure that is thermodynamically more stable than the zinc-blende structure. However, the zinc-blende structure has several advantages over the wurtzite structure, including higher carrier mobility, easier cleaving for LD fabrication, and higher thermal conductivity [1], and many studies on the growth and application of the zinc-blende III-nitride semiconductors have been reported [2]. Figure 1-1 shows the unit cells of the wurtzite and zinc-blende cubic structure.

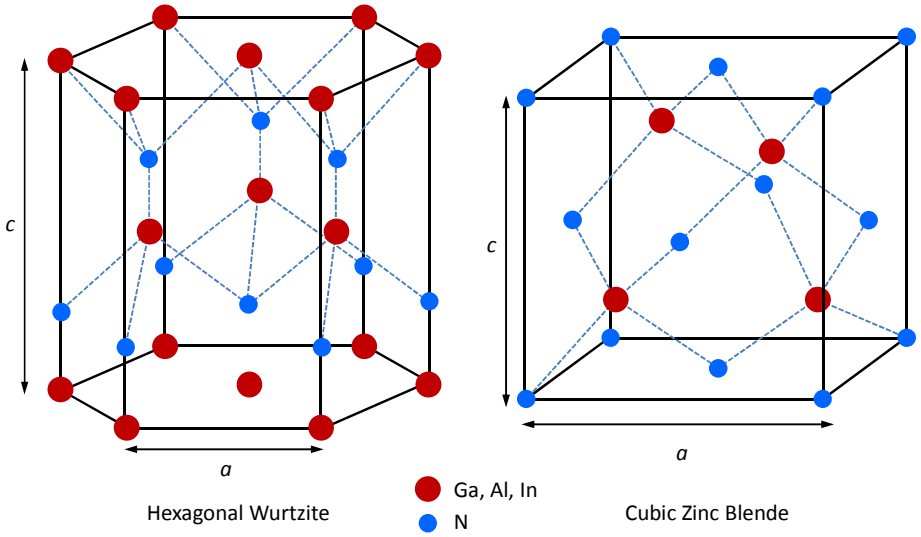

Figure 1-1. Unit cells of the hexagonal wurtzite structure (left) and the zinc-blende cubic structure (right).

In an ideal wurtzite structure, the ratio between *c/a* is 8/3 = 1.633. However, this ratio will be altered by the electronegativity difference between the Group III and the Group V atoms when they combine each other. As a result, the *c/a* ratio of AlN is 1.601, while that of GaN and InN is 1.627 and 1.612, respectively. These deviations and variations of the ratio are also related to the generation of a dipole, which results in a polarization charge. A nitrogen atom has the strongest electronegativity among the Group V atoms, and it adds a strong ionic bonding component to the covalent bonding between the Group III atoms. Therefore, the III-nitride semiconductors have a very tight bonding with a high bonding energy. The bonding energy of InN, GaN, and AlN is 7.7 eV/atom, 8.9 eV/atom, and 11.5 eV/atom, respectively [3]. These high bonding energies contribute to the superior thermal- and chemical-stability of the III-nitride semiconductors as well as to the short chemical bonding lengths as shown in Figure 1-2. The chemical bonding lengths of the III-nitride semiconductors are less than 22 nm, and they are shorter than those of most semiconductor materials. In addition, the strong electron affinity of a nitrogen atom helps the charge carriers being localized in the valence band of the III-nitride semiconductors. These characteristics play an important role in making the III-nitride

semiconductors a promising candidate for electronic- and optoelectronic-devices operating under high-power and high-temperature environments.

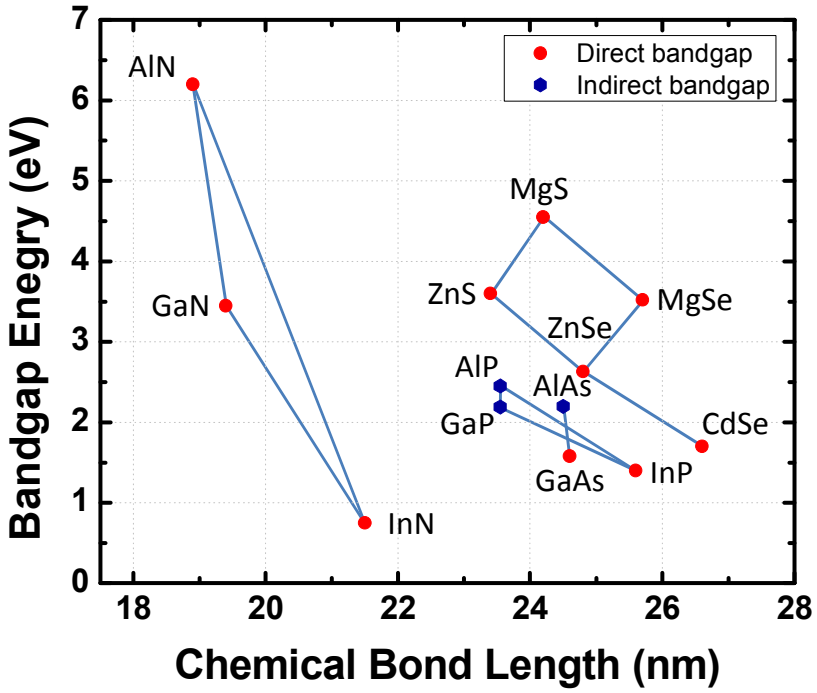

Figure 1-2. Bandgap and chemical bond-length of the III-nitride semiconductors and various semiconductors.

All III-nitride semiconductors in a wurtzite crystal structure exhibit a direct bandgap. The fundamental bandgap energy of each III-nitride binary compounds is 0.78 eV, 3.4 eV, and 6.23 eV for InN, GaN, and AlN, respectively. Therefore, the bandgap energy is tunable from 6.23 eV (~200 nm, deep UV region) to 0.78 eV (~1700 nm, infrared region) by forming binary or ternary compounds with AlN or InN. This is a big advantage of the III-nitride system over other material systems, as a very wide range of wavelengths can be covered solely by the III-nitride alloys and combining different material systems is not needed. Figure 1-3 shows the bandgap energy of the III-nitride semiconductor alloys in the wurtzite structure as a function of the *a*-axis lattice constant.

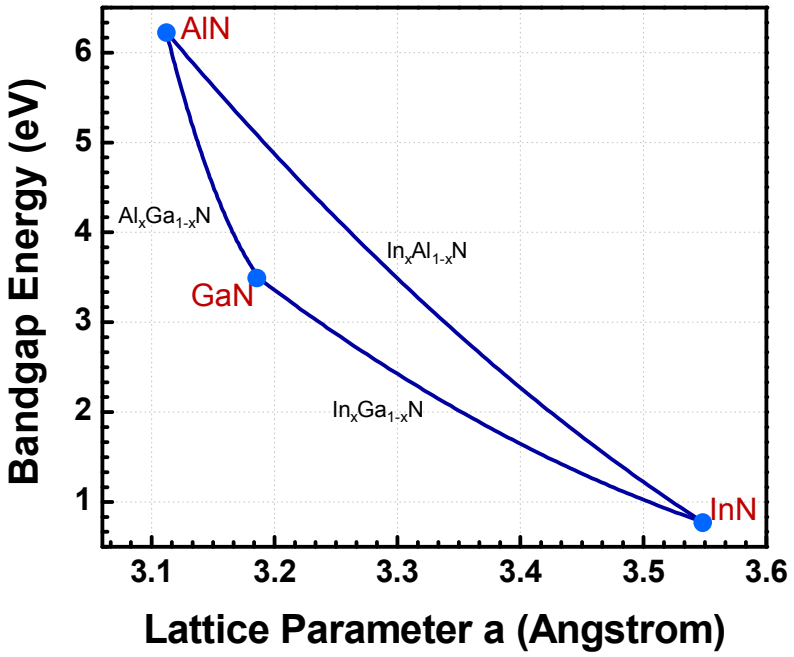

Figure 1-3. Bandgap energy as a function of the lattice constant for the III-nitride semiconductors in the wurtzite structure.

The bandgap energy of the ternary III-nitride alloy can be described by Vegard's Law with the alloy composition and bandgap energies of the binary alloys:

$$E_g^{AB}(x) = xE_g^A + (1-x)E_g^B - bx(1-x)\ , \qquad (1\text{-}1)$$

where x is the alloy composition and b is the bowing parameter. The bowing parameters of the AlN-GaN and InN-GaN systems are relatively well known to be 1.4 eV and 1.0 eV, respectively [4,5]. The InN-AlN system, however, does not have a well determined bowing parameter. Various values ranging from 3 to 5 eV have been suggested [6,7,8], but recent reports consider the bowing parameter of the InN-AlN system as large as 6 eV [9,10,11]. One of the technical difficulties in the growth of the III-nitride semiconductors is the lack of a lattice-matched substrate. Availability of bulk GaN or AlN substrates is still limited by their high manufacturing costs. Consequently, *c*-plane sapphire (α-Al_2O_3) substrates are widely used with their readily available low-price and high thermal stability, in

spite of their relatively large *a*-axis lattice mismatch of ~14.8% over the wurtzite GaN. In addition, the lattice mismatch between AlN and InN is around 13%, and InAlN is the only ternary alloy that is lattice matching to GaN. Therefore, the layer strain and dislocation induced by the lattice mismatch is an inevitable factor that should be considered in the growth of the III-nitride semiconductors.

As discussed earlier, the *c/a* ratio of the III-nitride in the wurtzite structure deviates from its ideal value of 3/8 due to the electronegativity difference between atoms. The deviation leads to the dipole formation and the polarization generation. Figure 1-4 shows the direction of the polarization field of the Ga- and N-polar AlGaN/GaN heterostructures under strained and relaxed status. The Figure 1-4 also shows the formation of the two-dimensional sheet charge induced by the polarization field.

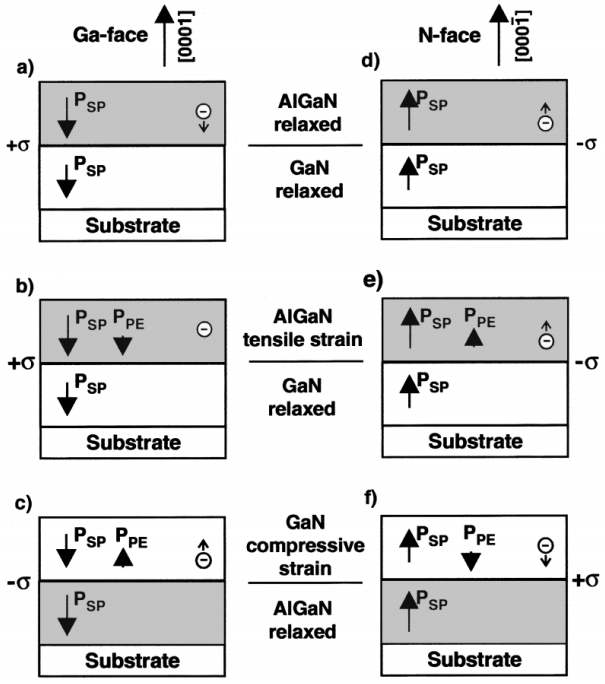

Figure 1-4. Directions of the spontaneous- and piezoelectric-polarization field and two-dimensional sheet charge density of the Ga- and N-polar AlGaN/GaN heterostructures under the strained and relaxed status [12].

In Figure 1-4, the polarization field is consisted with the spontaneous polarization field (P_{sp}) and the piezoelectric polarization field (P_{pe}). The size of the spontaneous polarization field is a material-specific property while the direction of the spontaneous polarization field is always aligned from Ga-(or other Group III atoms) face toward N- face. The overall spontaneous polarization field at the heterointerface is determined by the sum of the fields of the interfacing layers.

On the other hand, the piezoelectric polarization field of the III-nitride system originates from the $P6_3mc$ space group that the material system belongs to. The layer strain induced by the lattice mismatch between the III-nitride materials or foreign substrates is the main driving force for the generation of the piezoelectric polarization field. Its direction is determined by the direction of the layer strain. A tensile strain of the layer will produce a piezoelectric field with a direction antiparallel to the *c*-axis, and vice versa. The total polarization field over the layer is equal to the sum of the spontaneous polarization field and the piezoelectric polarization field. Therefore, the size and direction of the total polarization field are functions of the strain status and alloy composition of the layer.

The refractive index of the semiconductor material is a critical optical parameter which is closely related to the bandgap energy of the material. Reddy and Anjaneyulu proposed the following relationship between the refractive index and the bandgap energy [13]:

$$E_g e^n = 36.3 \, . \qquad (1\text{-}2)$$

Because of their wide bandgap, the III-nitride semiconductors have rather small refractive indices from 1.8 (for AlN) to 2.9 (for InN). For most III-nitride based optoelectronic devices operate in a visible wavelength region, InGaN is commonly used as an active layer material because of its appropriate bandgap energy. Therefore, a cladding layer to confine and guide generated photons by a total reflection at the interface is often consisted with a low-refractive-index Al-containing material

which can maximize the index contrast against the active region. Higher index contrast can be achieved by incorporating more aluminum content into the alloy, but higher aluminum composition can lead to a larger lattice mismatch and a strain-induced layer degradation which have negative effects on the performance of the device. Therefore, the most commonly used cladding layer material is AlGaN with aluminum composition of around 30%. Also, recent studies suggest that InAlN with x_{In} ~18% that is lattice-matching to GaN is a promising candidate for the cladding layer material to replace AlGaN because of its high aluminum composition over 80%, lower refractive-index, and smaller or negligible layer strain. Table 1-1 summarizes various physical properties of the III-nitride materials.

Table 1-1. Physical properties of the III-nitride semiconductors [14,15].

Property	GaN	AlN	InN
Lattice constant, *a* [A]	3.189	3.112	3.548
Lattice constant, *c* [A]	5.185	4.982	5.76
Bandgap [eV]	3.47	6.23	0.78
Refractive index, *n*	2.35	1.80	2.90
Thermal conductivity, κ [W/cm K]	1.3	2.0	0.8
Dielectric constant, ε_0	9.5	8.5	15.0
c_{11} [GPa]	390	396	223
c_{12} [GPa]	145	137	115
c_{13} [GPa]	108	106	92
c_{33} [GPa]	398	373	224
Poisson's Ratio ν	0.508	0.579	0.821

1.3 Growth of the III-Nitride Semiconductors by Metalorganic Chemical Vapor Deposition

Since the initial development by Manasevit and his colleagues [16] in the late 1960's, metalorganic chemical vapor deposition (MOCVD) has been a major growth technique for high-quality compound semiconductors for electronic- and optoelectronic-devices over conventional growth techniques such as liquid-phase epitaxy (LPE) and vapor-phase epitaxy (VPE). Although molecular-beam epitaxy (MBE) technique is also capable of producing high-quality materials with abrupt interfaces, MOCVD is more suitable for a large-scale production with various material systems. Therefore, MOCVD is widely accepted in both academic research and industrial applications. Since its development, there have been many terms developed to name this growth technique, including metalorganic vapor phase epitaxy (MOVPE), organometallic CVD (OMCVD), and organometallic VPE (OMVPE). However, Manasevit first used the term MOCVD and it has been widely accepted.

In a conventional CVD process, two or more materials are introduced into a chamber (usually in a gaseous phase) to chemically react each other and form a new material near the substrate surface. MOCVD adds an extra step of reaction between the precursors on this process. A metalorganic (or alkyl) precursor is usually supplied as a condensed phase (liquid or solid) and a carrier gas "bubbles" it to transport it into the chamber. Trimethylgallium (TMGa), triethylgallium (TEGa), trimethylaluminum (TMAl), and trimethylindium (TMIn) are the commonly used the Group III precursors in the III-nitride semiconductor epitaxy. When NH_3 is used as a Group V precursor, the reaction to form a III-nitride compound can be described by the following equation:

$$R_3M + NH_3 \leftrightarrow MN + 3 \cdot RH \ , \qquad (1\text{-}3)$$

where R is an alkyl group such as methyl (CH_3) or ethyl (C_2H_5), M is the Group III metal such as gallium (Ga), indium (In), or aluminum (Al). Nitrogen is rarely used as a Group V source due to its extremely low dissociation rate [17]. Instead, NH_3 is widely used as it has a decomposition rate of around 4% up to 950 ^oC [18]. In the MOCVD growth process, precursors and gases introduced into a chamber form a new material on the wafer surface via several steps, *i.e.*, gas input, pyrolysis, diffusion, and surface reaction. The by-products formed during these steps are pumped away with carrier gases. Figure 1-5 shows a schematic illustration of the MOCVD process in a vertical-flow system.

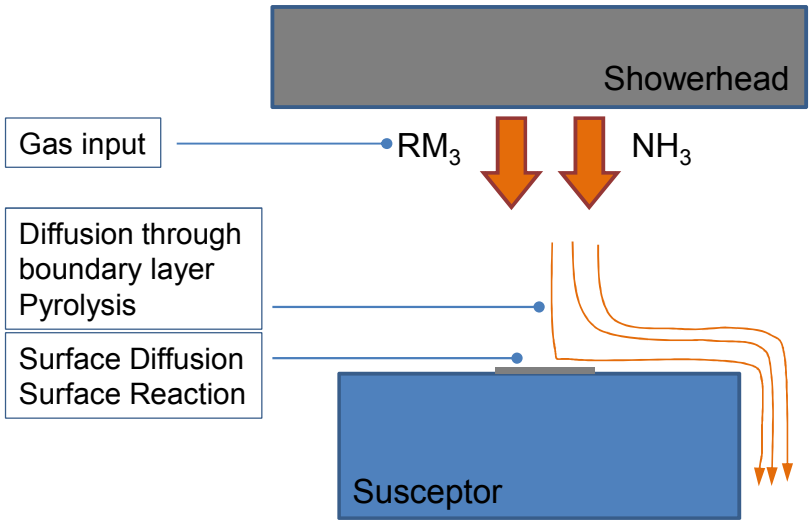

Figure 1-5. Schematic illustration of the MOCVD process in a vertical-flow system.

When metalorganic sources are transported into the chamber by a bubbling process, their molar flow rates depend on the flow rates of carrier gases, the pressure of the metalorganic source container (bubbler), and the equilibrium vapor pressure of the precursor. When the vapor phase and the condensed phase co-exist in an equilibrium status, the equilibrium vapor pressure can be described by the following equation [19]:

$$\log p_{eq}(T) = B - \frac{A}{T} + C\log T\ , \qquad (1\text{-}4)$$

where $p_{eq}(T)$ is an equilibrium vapor pressure of the condensed phase, T is temperature in degrees Kelvin, and A, B, and C are material-specific constants. The constant C is often neglected in the practical use, making the relationship simpler. Equation 1-4 shows that the equilibrium vapor pressure of a metalorganic source is a strong function of the temperature. Therefore, bubblers are usually kept in an isothermal bath to maintain a constant temperature. Table 1-2 summarizes the thermodynamic properties of the various metalorganic precursors.

Table 1-2. Thermodynamic properties for the selected metalorganic precursors used in the MOCVD growth of the III-nitride semiconductors.

Chemical Name	Formula	Formula Weight	$\log p$ (mmHg) = $B - A / T$	
			A	B
Trimethylgallium (TMGa)	$(CH_3)_3Ga$	114.83	1703	8.07
Triethylgallium (TEGa)	$(C_2H_5)_3Ga$	156.91	2162	8.083
Trimethylaluminum (TMAl)	$(CH_3)_3Al$	72.09	2134.83	8.224
Trimethylindium (TMIn)	$(CH_3)_3In$	159.93	3014	10.52
Bis(cyclopentadienyl) magnesium (Cp_2Mg)	$(C_5H_5)_2Mg$	154.49	$\log p$ (mmHg) = $B - A / T$ + 2.18 log$T$	
			4198	25.14

The constant total pressure inside a bubbler is also a critical factor for the constant bubbling efficiency. This is achieved by using an electronic pressure controller (EPC) controlled by a computer. Molar flow rate of a metalorganic source is then obtained by the following equation:

$$Q = \frac{p_{eq}(T)}{P - p_{eq}(T)} \frac{F_{CarrierGas}}{C_{STP}} \quad , \tag{1-5}$$

where P is the bubbler pressure, $p_{eq}(T)$ is the equilibrium vapor pressure of the metalorganic source, $F_{CarrierGas}$ is the flow rate of a carrier gas in standard cubic centimeter per minute (sccm), and C_{STP} is 22,406 cc/mole that is the molar volume of an ideal gas at standard temperature (298.15K) and pressure (760 Torr).

Material growth in this study was performed by using Thomas Swan Scientific Equipment 6x2" close-coupled showerhead (CCS) reactor. The CCS technology can provide a growth uniformity for a vertical rotating-disk system with a mass transport with completely and uniformly intermixed gas phases while minimizing the impact of growth parameters such as disk spinning rate, source flow rate, growth pressure and temperature on the growth results.

1.4 Scope of This Work

The III-nitride semiconductor-based optoelectronic devices have been very successful in the past decade because of their compact size, high energy efficiency, and long lifetime. Especially, LEDs are expected to replace conventional light sources in many applications including display devices and general lighting in near future. In spite of their significant improvements in the luminous performance, however, the initial costs of the LEDs are still not low enough for them to be competitive with incandescent bulbs and fluorescent lamps. To compensate the high initial costs of the LEDs within a reasonable period, their light emission efficiency should be further improved. The efficiency droop problem is considered as the most critical challenge preventing LEDs from achieving a higher emission efficiency, as it causes a substantial reduction of the emission efficiency in a high injection-current density condition. This work will focus on the growth of the III-nitride semiconductor based

LEDs by using MOCVD and the reduction of the efficiency droop of visible LEDs with a novel device structure. Chapter 2 covers the principles of the essential material characterization tools which are used in this study. Chapter 3 investigates the effect of various factors including the physical properties of the substrates and growth environments on the actual growing-surface temperature during the MOCVD growth process by using the *in-situ* temperature monitoring tools and the finite element method (FEM) calculation. The results obtained in this chapter are utilized in the subsequent epitaxial layer growth for the better crystalline quality. Chapter 4 discusses the development and adoption of an InAlN electron-blocking layer into the visible LED structures to prevent carrier spill-over which is considered as a major origin of the efficiency droop. Finally, Chapter 5 summarizes results and describes future works to further suppress efficiency droop of the visible LEDs.

CHAPTER 2 MATERIAL CHARACTERIZATION

2.1 Introduction

The study of the semiconductor materials requires various analysis and characterization techniques for the growth of the high quality materials. This chapter discusses the basic principles of *in-situ* and *ex-situ* characterization methods to monitor the growth process and analyze various properties of the semiconductor materials.

2.2 *In-situ* Temperature Monitoring and Reflectance Measurement

The temperature of the substrate is a very important parameter for the growth of the semiconductor materials using the MOCVD technique. The temperature of the substrate creates significant influences on almost every physical aspects of the grown epitaxial layer, including the growth rate, the alloy composition, the surface roughness, and the crystalline quality. Therefore, *in-situ* monitoring of the substrate temperature and its precise control is indispensable for the growth of the high-quality epitaxial layers [20].

Conventionally, the growth temperature of the layer has been determined by using a thermocouple sensor that is located under the susceptor where a substrate is placed during growth. In this configuration, the amount of heat transferred from the heater to the substrate is inconsistent with the heat conveyed to the thermocouple, and the temperature detected at the thermocouple is often significantly different from the actual temperature of the substrate. The wafer temperature can be deduced by several tests runs and a linear interpolation of the results. However, these predictions often suffer from a poor accuracy, as various growth parameters such as the material of the susceptor, the epitaxial layer being grown, the chamber pressure, and the flow rates of the carrier gases are also related with the substrate temperature. Therefore, a pyrometer that directly measures the surface

temperature of the substrate through an optical method is the most appropriate tool for *in-situ* monitoring of the growth temperature.

A pyrometer detects the temperature based on the principle that an object emits electromagnetic radiation proportional to its temperature. The temperature and the radiation intensity of a black body at a certain wavelength can be described by Plank's Law as follows:

$$dP_s = \frac{2}{h^4 c^3} \frac{(\hbar\omega)^5}{e^{\hbar\omega/k_b T - 1}} d\lambda \ , \qquad (2\text{-}1)$$

where P_s is the radiation intensity of the black body. The thermal-radiation intensities of a black body along with the wavelength (or photon energy) at different temperatures are shown in Figure 2-1. The thermal radiation is observed mainly in the region with a wavelength longer than 950 nm, and the power of the emitted radiation that can be obtained from the area below the curve increases with the increase of the temperature. Therefore, the temperature of a black body can be inferred from the radiation power.

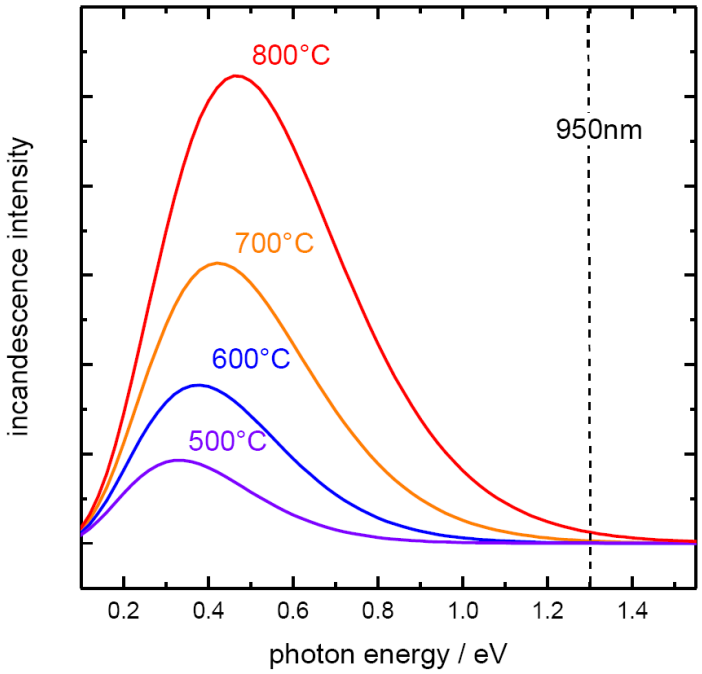

Figure 2-1. Thermal radiation of a black body according to Planck's Law [21].

The estimation of the temperature of an actual substrate by using Plank's Law, however, can lead to a significant measurement error because of the non-ideal absorption/emission characteristics of a real body. Plank's Law assumes that a body will emit all incoming thermal energy as a form of a radiation regardless of its electromagnetic wavelength. This assumption is true for an ideal black body, but the radiation of a real body is often much less than that of a black body, as the radiation in a real body is attenuated by the optical properties (which are also a function of the emission wavelength) and the surface roughness of the real body. The ratio between the radiation intensities of a black body and a real body can be described by an emissivity, as follows:

$$\varepsilon(\lambda, T) = \frac{P}{P_S} \ , \qquad (2\text{-}2)$$

where ε is an emissivity of the real body. For an accurate temperature measurement, the emissivity of the body should be exactly determined. However, the emissivity (and also the absorption coefficient) has no fixed value but changes continuously over the growth process, because it is a function of the alloy composition and the temperature of the material (because of the temperature dependent nature of the bandgap energy). Also, the thermal radiation usually experiences multiple reflections and interferences at the interfaces between the epitaxial layers or between a layer and a substrate before it escapes from the wafer. These constructive or destructive interferences cause a significant modulation on the detected radiation intensity and a false signal or a non-existing temperature change. The fluctuation of the detected temperature without the proper correction process is shown in Figure 2-2 as a blue line.

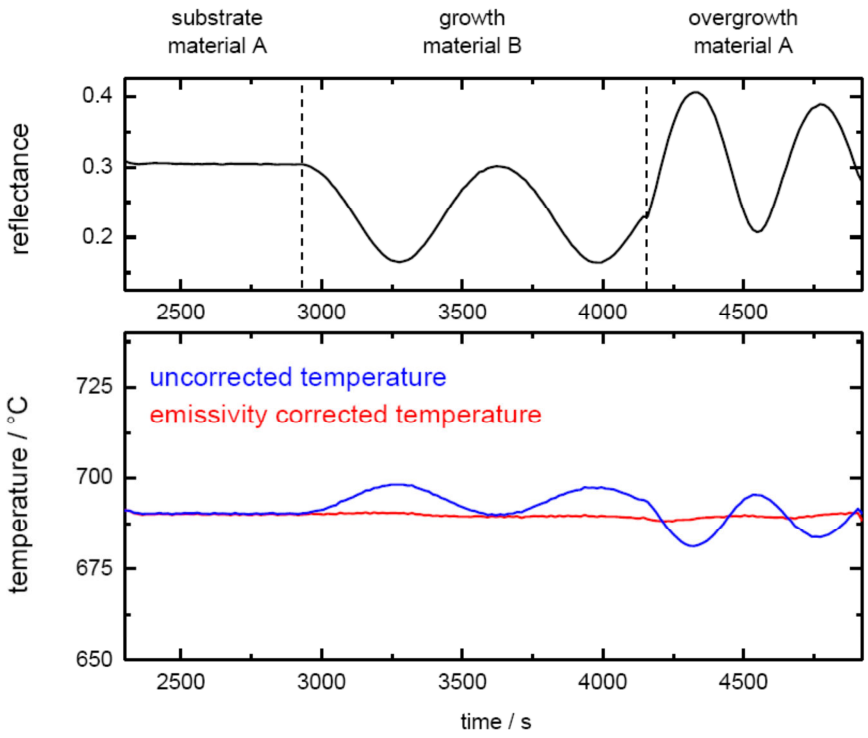

Figure 2-2. Results of the true temperature measurement during the heteroepitaxy growth [21].

To measure an actual emissivity and correct these artifacts, the reflectance of the wafer should be measured in real-time at the same wavelength that the thermal-radiation intensity of the wafer is detected. During the reflectance measurement, the wafer is illuminated with a dedicated light source, and the intensity of the reflected beam is measured. According to the principle of energy conservation, the sum of the absorbed, reflected, and transmitted radiation should be equal to the incident light. If the wafer is opaque at the incident wavelength, the transmitted radiation can be safely ignored, and the absorption is easily obtained from the following relationship:

$$\alpha = 1 - R \ , \tag{2-3}$$

where α is the absorption coefficient and R is the reflectance. According to Kirchhoff's Law, the absorption is equal to the emissivity of the body, as shown in the following equation:

$$\alpha(\lambda, T) = \varepsilon(\lambda, T) \ . \tag{2-4}$$

Therefore, the emissivity of a wafer can be derived directly from the measured reflectance. The substrate temperature after the emissivity-correction is shown in Figure 2-2 as a red line. If the wafer is transparent to a significant fraction of the black-body radiation (for example, growth of a GaN layer on a double-polished sapphire substrate or a SiC substrate), then the transmitted radiation T in Equation 2-3 is not negligible. A pyrometer will detect the radiation not only from the wafer but also from the underlying susceptor on which the wafer is located. Also, the Group III-nitride semiconductors are usually transparent to the near-infrared (NIR) spectrum around 950 nm, resulting in the "reading" of the emissivity of the susceptor (with possible alteration by the substrate condition) instead of the emissivity of the substrates and the epitaxial materials [22]. These situations cause a certain amount of the deviation on the temperature reading. To correct the deviation, the absolute

temperature of the susceptor ($T_{suscpetor}$) is determined first by a melting-point measurement, eutectics, or a pyrometry at two different wavelengths. Then, the temperature of the wafer is determined from its optical properties. These two measurements can provide a temperature difference (ΔT) between the susceptor and the wafer, and this information can be used to compensate the temperature detected by the pyrometer to provide a correct temperature of the wafer during the growth process. There are also other approaches, such as the calibration of the temperature based on *in-situ* measured bandgap shift of the SiC in conjunction with a real-time emissivity-corrected pyrometry [23], the use of a near-ultraviolet (NUV) spectrum (λ~405 nm) that is opaque to GaN materials at high temperatures [24], and the use of a mid-IR (MIR) wavelength range (7~8 μm) where sapphire substrates are opaque and the reactant gases are transparent [25].

On the other hand, *in-situ* reflectance measurement is also able to provide very useful information on the epitaxial growth such as thickness, growth rate, and surface morphology of the growing layer. When the layer is transparent, a part of the incident beam is reflected at the growing-surface, while the remaining part of the beam goes through the layer and reflected at the interface between the layer and the substrate. These two beams will experience constructive or destructive interferences to cause an oscillation of the intensity signal at the detector side. This phenomenon is called as Fabry-Perot oscillation, and its period is closely related with the thickness of the layer. The different paths of the beams reflected at the surfaces of the epitaxial layer and at the substrate are shown in Figure 2-3.

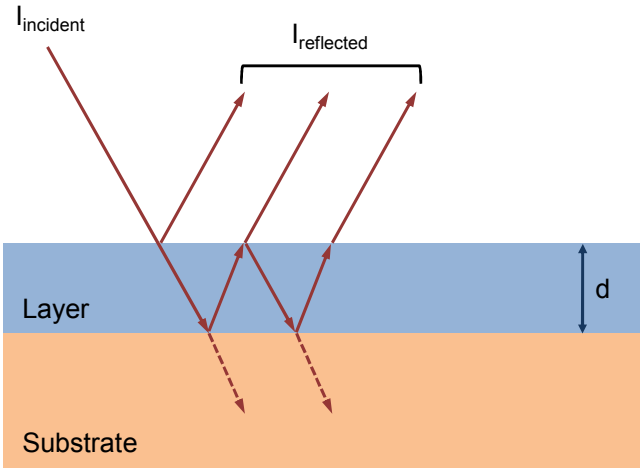

Figure 2-3. Reflections of the incident beam at the surfaces of an epitaxial layer and at a substrate.

For constructive or destructive interferences, the path difference (which is the thickness of the layer) should satisfy the following relations:

$$2nd = m\lambda \,, \quad \text{and} \tag{2-5}$$

$$2nd = (m + \tfrac{1}{2})\lambda \,, \tag{2-6}$$

where n is the refractive index of the epitaxial layer, d is the thickness of the epitaxial layer, m is an even integer, and λ is the wavelength of the incident beam. From these equations, the increase of the layer thickness during a single period of the oscillation of the reflectance can be derived as

$$\Delta d = d_1 - d_2 = \frac{\lambda}{2n} \,. \tag{2-7}$$

Therefore, the layer thickness and the growth rate can be calculated from the refractive index of the layer and the oscillation period of the reflectance signal. A reflectance curve measured during the

growth of a GaN layer on a GaN/sapphire substrate is shown in Figure 2-4. The period of the reflectance oscillation is 182 sec, and this corresponds to the layer thickness increase of 633 nm / (2×2.4) = 135 nm. The growth rate of the GaN layer is calculated to be 135 nm / 182 sec = 0.742 nm/sec, and the total layer thickness will be ~1500 nm if the layer is grown for 2000 sec.

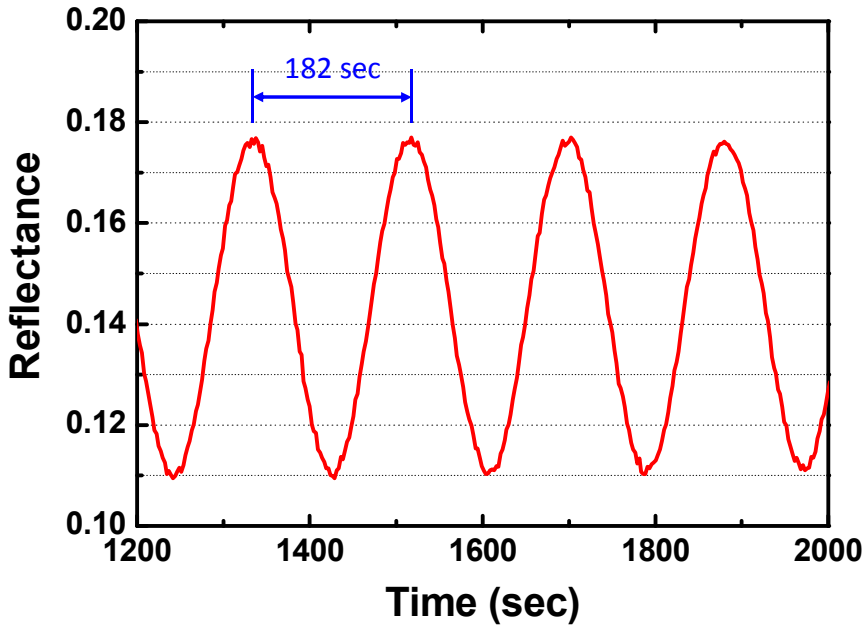

Figure 2-4. A reflectance measurement result during the growth of a GaN layer on a GaN/sapphire substrate.

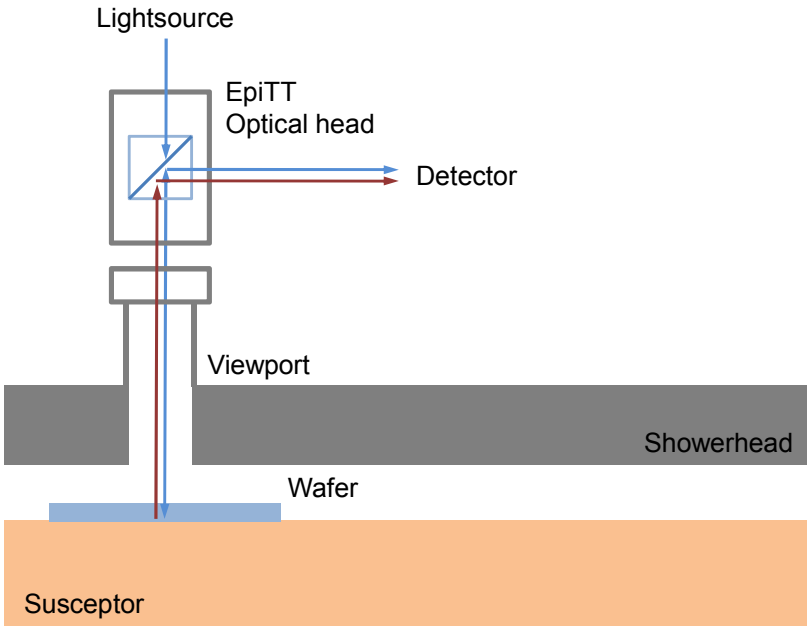

Figure 2-5. Schematic configuration of the EpiTT installation on the showerhead type MOCVD chamber.

We used LayTec's EpiTT® system for *in-situ* temperature monitoring and reflectance measurement. The growth temperature, the growth rate, and the thickness of the layer specified in this work are determined from the EpiTT® measurement results and confirmed by other post-growth characterization techniques including transmission electron microscopy and high-resolution X-ray diffraction. A schematic configuration of the EpiTT® installation on our MOCVD system is shown in Figure 2-5.

2.3 X-Ray Diffraction

High-resolution X-ray diffraction (HR-XRD) is a very powerful tool for the characterization of the crystalline materials. In the HR-XRD technique, an incident X-ray beam collides with a specimen, and the number of the scattered electrons is recorded with the angular information to obtain a "rocking curve". HR-XRD technique can determine the crystalline quality, thickness, alloy

composition, strain status, and the degree of relaxation of the epitaxial layer via a non-destructive process. For the precise analysis of the materials, an X-ray beam with a small beam divergence is inevitable. There are several techniques and designs to obtain a narrow X-ray beam, including a multilayer mirror, capillary optics, or a pinhole collimator. The schematic structure of an XRD system with a pinhole collimator consisting of two pinholes with apertures of the same diameter *d* separated by a distance of *h* is shown in Figure 2-6. *F* is the source size of the X-ray beam. An anti-scattering pinhole is used to block the scattering of the X-ray beam at the second pinhole.

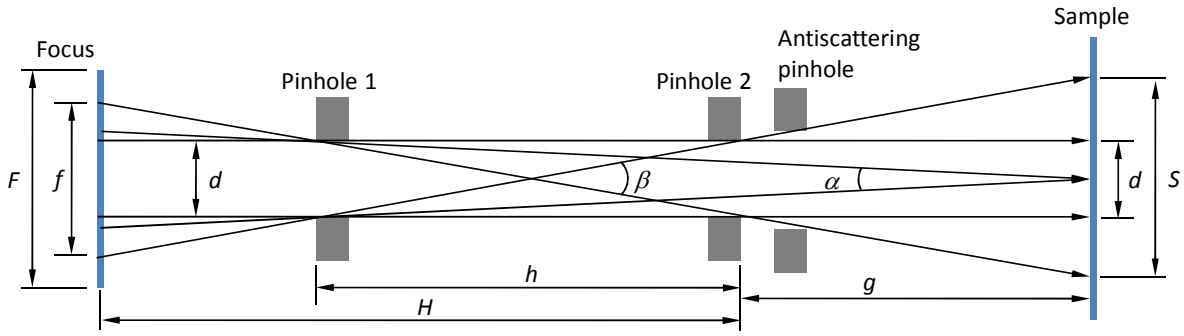

Figure 2-6. Schematic diagram of an XRD with a pinhole collimator.

The divergence of the X-ray beam in this configuration is given by the following equation:

$$\beta = \frac{2d}{h}\delta\theta = \frac{h+s}{a} \quad . \tag{2-8}$$

In the typical case when *d* is 0.2 mm and *h* is 150 mm, the divergence of the beam is around 550 arcsec. This divergence value is too large for a fine characterization of the materials, especially for the semiconductor materials whose peak separation between the epitaxial layer and the substrate is often only several hundred arcsec. Reducing the diameter of the pinhole will make the beam divergence smaller, but the manufacturing of a very small pinhole with the beam divergence below several arcsec.

is very difficult. Other beam collimation configurations that rely on mechanical techniques also hold similar problems. Therefore, most HR-XRD systems utilize a single-crystal beam conditioner in front of the X-ray source to obtain a collimated and monochromated beam. For widely used Cu $K_{\alpha 1}$ source (λ=1.540562 A), multiple Ge (220) crystals are commonly used as a monochromator. Most HR-XRD systems equipped with a crystal beam conditioner can provide a beam with an angular resolution below 1 arcsec. The monochromated beam is incident into the specimen and collected by the detector. A typical configuration of a HR-XRD system with a crystal beam conditioner is shown in Figure 2-7.

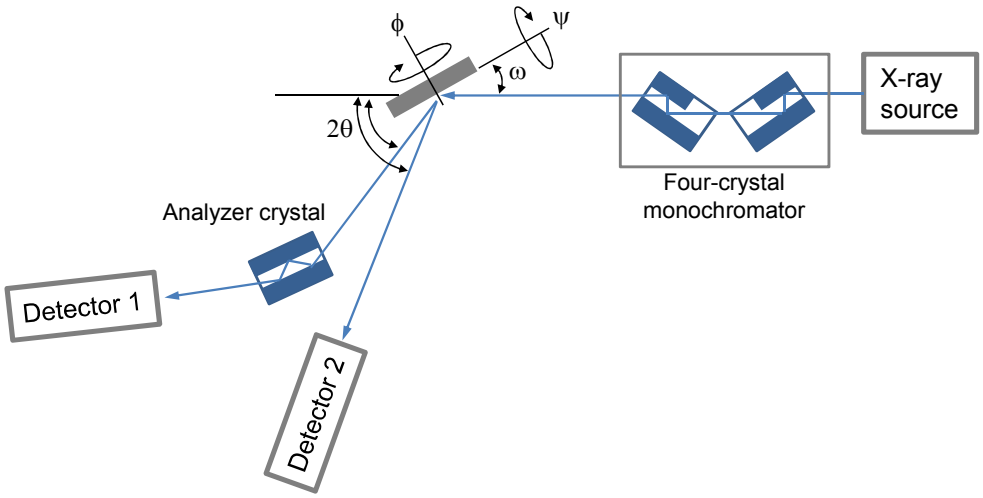

Figure 2-7. A typical configuration of a HR-XRD system.

As shown in Figure 2-7, a HR-XRD system has several axes which can be driven independently or coupled with other axis, such as ω-axis (sample rocking), ϕ-axis (sample rotation), ψ-axis (sample tilt), and θ-axis (detector rocking). The basic principle of HR-XRD can be best explained by assuming that the material is consisted with parallel adjacent planes of atoms with a spacing of d, as shown in Figure 2-8.

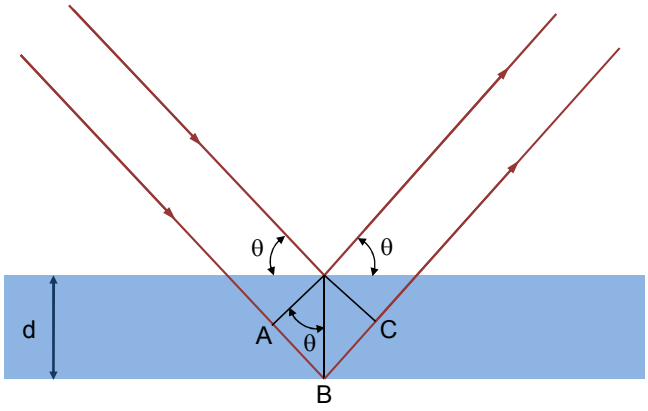

Figure 2-8. Two different traveling paths of X-ray beams in a crystal.

When X-ray beams with an incident angle of θ are scattered by a crystal, the difference of the traveling paths between the beams reflected at the surface of the sample and reflected at the crystal interface (the path "A-B-C" in Figure 2-8) can be expressed as *2dsin(θ)*. When this path difference becomes a multiple of the wavelength of the source X-ray beam, a constructive interference occurs, and a large signal will be detected at the detector. This condition is described by Bragg's Law as

$$n\lambda = 2d\sin(\theta) \ . \tag{2-9}$$

The wavelength of the X-ray beam λ is fixed, so we can obtain the inter-planar spacing d by measuring the detector angle θ when a constructive interference occurs. If the lattice constant of the material is known, the spacing of the planes having Miller indices of *(h k l)* in a cubic lattice is expressed as

$$\frac{1}{d_{hkl}^2} = \frac{h^2+k^2+l^2}{a^2} \ . \tag{2-10}$$

In case of a hexagonal lattice, the inter-planar spacing is represented as

$$\frac{1}{d_{hkl}^2} = \frac{4}{3}\left(\frac{h^2+hk+l^2}{a^2}\right) + \frac{l^2}{c^2} \quad . \tag{2-11}$$

Therefore, once the inter-planar spacing of the layer is known by measuring the Bragg Angle, the lattice constant of the sample can be obtained by using above equations. In an actual measurement, an X-ray beam from the fixed source is directed toward the surface of a specimen that is rotating in the ω-axis. The beam scattered at the specimen is collected by the detector that is rotating in the θ-axis twice as fast (twice more angular speed) as the specimen. The angular positions of the specimen and the detector are recorded with the beam intensity. The Bragg Angle is determined from the detector angle where the peak intensity appears. This method, called as ω-2θ scan, is the basic scan method for a double-crystal diffraction (DCD) measurement.

If an epitaxial layer is grown by a heteroepitaxy, the lattice constant of the epitaxial layer is different from that of the underlying substrate. Under the assumptions that the substrate is thick enough, the lattice constant of the epitaxial layer is larger than that of the substrate, and the epitaxial layer is fully strained to the substrate, the lattices of the epitaxial layer will experience a tetragonal distortion as shown in Figure 2-9.

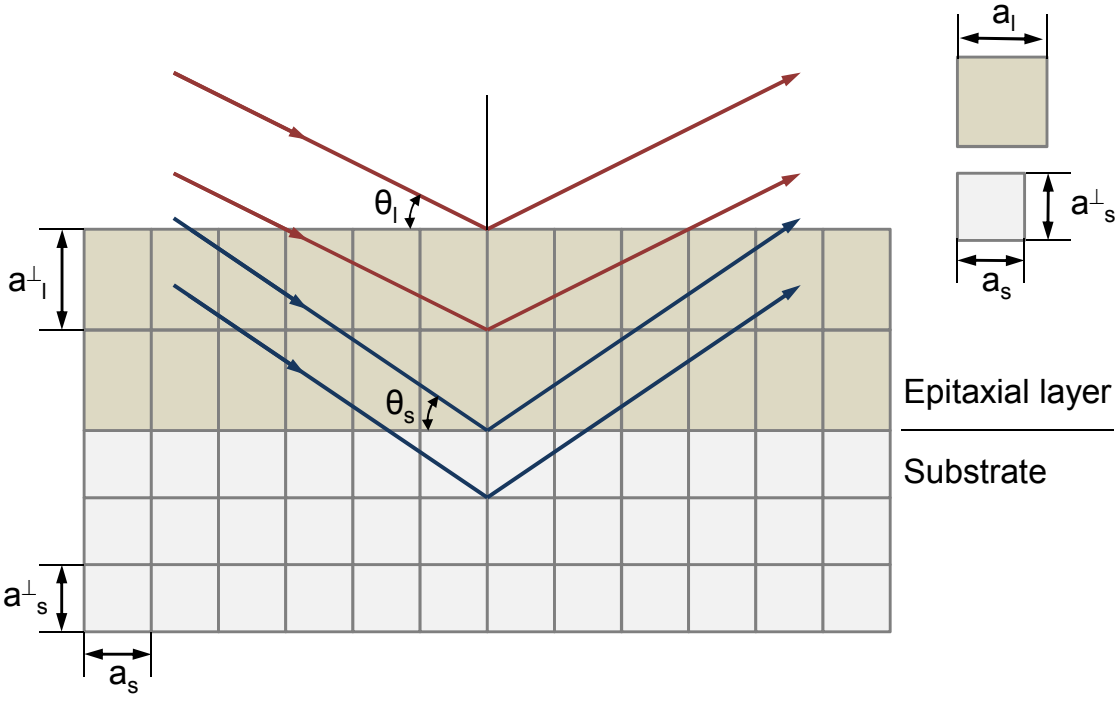

Figure 2-9. The paths of the X-ray beams inside an epitaxial layer and a substrate under a symmetric diffraction condition.

The lattice distortion (or strain) of the epitaxial layer in a vertical direction is linearly converted into the relaxed lattice strain (the lattice strain before the tetragonal distortion) by using Poisson's Ratio, as shown in the following equation:

$$\varepsilon_r = \frac{a_l - a_s}{a_s} = \left(\frac{1-\nu}{1+\nu}\right)\varepsilon^{\perp} = \left(\frac{1-\nu}{1+\nu}\right)\left(\frac{a_l^{\perp} - a_s^{\perp}}{a_s^{\perp}}\right), \qquad (2\text{-}12)$$

where ν is Poisson's Ratio. a_l and a_s are the in-plane lattice constants of the layer and the substrate when they are relaxed, while $a^{\perp}_l$ and $a^{\perp}_s$ are the vertical-direction lattice constants of the layer and the substrate under the tetragonal distortion, respectively. Similarly, ε_r represents the lattice strain between the layer and the substrate when the epitaxial layer is fully relaxed, while $\varepsilon^{\perp}$ represents the lattice strain in a vertical direction under the tetragonal distortion. According to Equation 2-12, it is

clear that the measurement of the vertical-direction lattice strain will reveal the relaxed lattice strain and the relaxed in-plane lattice constant of the epitaxial layer. When an X-ray beam is incident with a symmetric diffraction condition, *e.g.* an incident on the plane of (0 0 *L*), the substrate and the epitaxial layer have different Bragg conditions, because their inter-planar spacings are not identical. Their Bragg Angles are represented by the following equations:

$$\lambda = 2d_s \sin(\theta_s), \quad \text{and} \tag{2-13}$$

$$\lambda = 2d_l \sin(\theta_l), \tag{2-14}$$

where d_s and d_l are the spacings of the (0 0 *L*) planes in the substrate and the epitaxial layer, respectively. Therefore, the intensity peaks from the substrate and the epitaxial layer will appear at the different detector angles of $2\theta_s$ and $2\theta_l$ during the ω-2θ-scan. When the lattice constant of the substrate is known, the separation angle between the peaks provides the spacing of the diffraction planes of the epitaxial layer through the following equations:

$$\Delta d = \frac{\lambda}{2}\left(\frac{1}{\sin(\theta_l)} - \frac{1}{\sin(\theta_s)}\right), \quad \text{and} \tag{2-15}$$

$$\varepsilon^{\perp} = \left(\frac{d_l - d_s}{d_s}\right) = \frac{\sin(\theta_s)}{\sin(\theta_s + \Delta\theta)} - 1, \tag{2-16}$$

where Δd is the difference between the inter-planar spacings of the epitaxial layer and the substrate, and $\Delta\theta$ is the angular separation of the peaks. In the symmetric scan on the (0 0 *L*) plane, the inter-planar spacing d_l and the vertical-direction lattice constant $a^{\perp}_l$ is related by the following equation:

$$a_l^{\perp} = d_l L . \tag{2-17}$$

Therefore, once the peak-separation angle is measured, the vertical-direction lattice strain $\varepsilon^{\perp}$ and the relaxed lattice strain ε_r can be obtained by using Equation 2-12, 2-16, and 2-17. The relaxed in-plane lattice constant of the epitaxial layer is calculated from the lattice constant of the substrate and Equation 2-12. The layer composition is calculated by applying Vegard's Law on the relaxed in-plane lattice constant of the epitaxial layer.

In case of an asymmetric diffraction condition where the X-ray beam is incident on the planes such as (1 0 2) or (1 0 5), the Bragg Angle and the inter-planar spacing have somehow different relationship against the symmetric condition. The lattices and diffraction planes of an epitaxial layer and a substrate in an asymmetric scan are shown in Figure 2-10.

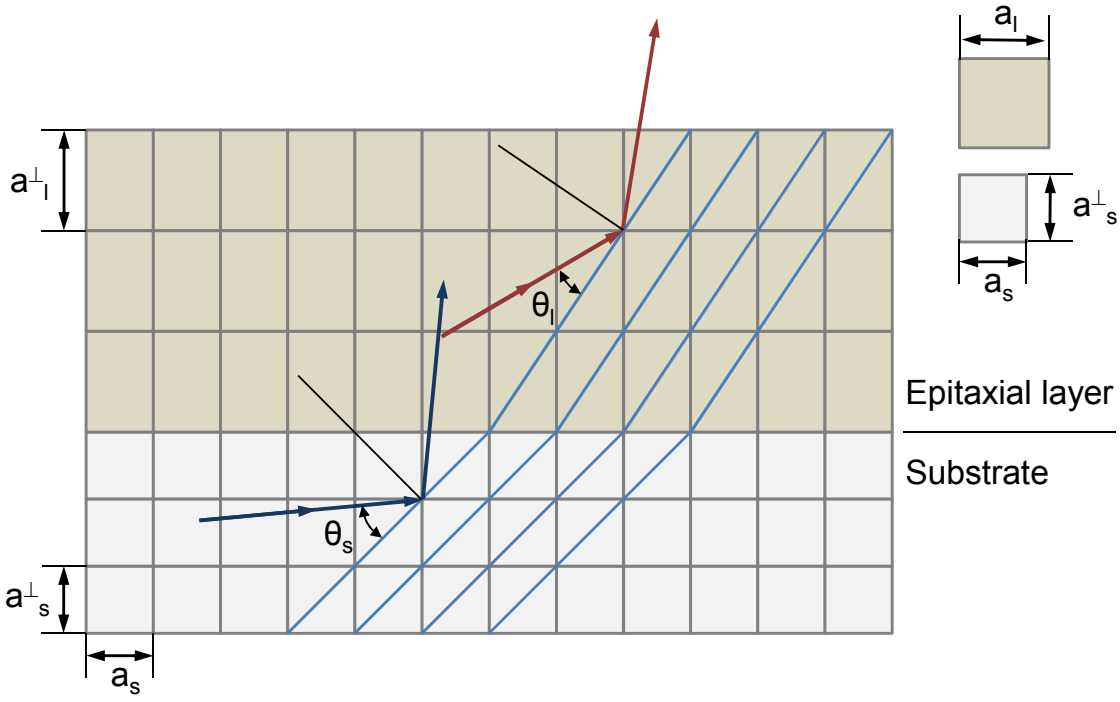

Figure 2-10. The paths of the X-ray beams inside an epitaxial layer and a substrate under an asymmetric diffraction condition.

In the asymmetric ω-2θ-scan, the separation of peaks from an epitaxial layer and a substrate includes the tilt angle between the reflection planes of an epitaxial layer and a substrate. Therefore, an asymmetric scan is more useful than the symmetric scab in analyzing the sample with a small lattice-constant difference between the epitaxial layer and the substrate. Also, the asymmetric scan provides more detailed information about the density of the threading dislocations and defects in the epitaxial layer.

Previously described procedures for measuring the lattice constant and the composition of the layer are based on the assumption that the epitaxial layer is fully strained to the substrate. In many cases, however, the epitaxial layer is partially or fully relaxed as the layer thickness is above the critical thickness. To analyze the partially relaxed layer, the "degree of relaxation" of the layer should be taken into account. The lattice distortions of the epitaxial layers under the fully strained and partially relaxed status are shown in Figure 2-11.

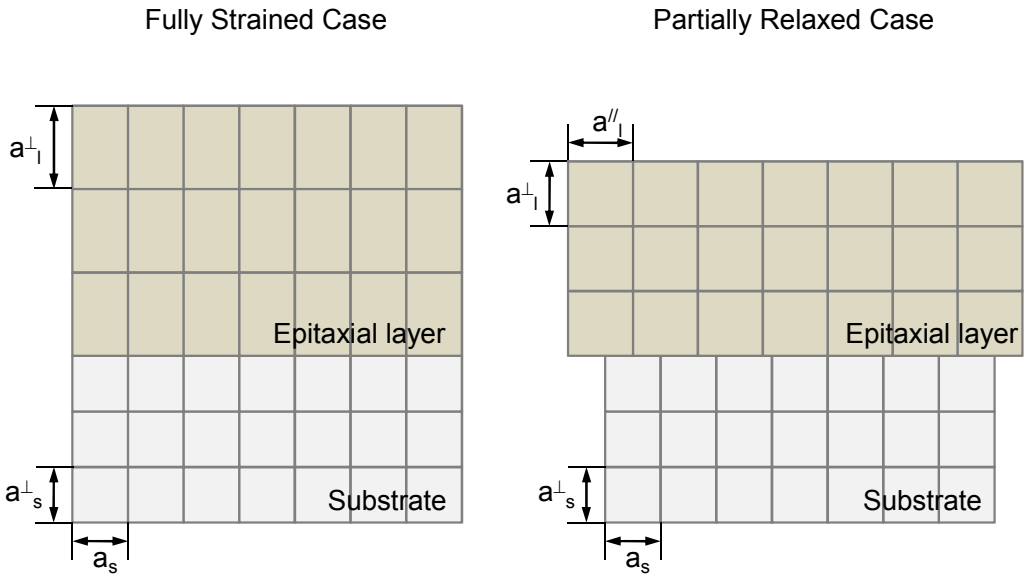

Figure 2-11. Lattice distortions of the epitaxial layers under fully strained (left) and partially relaxed (right) status to the substrates.

When a layer is partially relaxed, the relaxed lattice strain ε_r and the vertical-direction lattice strain $\varepsilon^{\perp}$ do not comply with Equation 2-12, and the in-plane lattice strain under the tetragonal distortion should be additionally considered, as in the following equations:

$$\varepsilon_r = \left(\frac{1-\nu}{1+\nu}\right)(\varepsilon^{\perp} - \varepsilon_{\parallel}) + \varepsilon_{\parallel} \text{ , and} \tag{2-18}$$

$$\varepsilon_{\parallel} = \frac{a_l^{\parallel} - a_s^{\parallel}}{a_s^{\parallel}} \text{ ,} \tag{2-19}$$

where $\varepsilon_{//}$ is the in-plane lattice strain, and $a^{//}_l$ and $a^{//}_s$ represent the in-plane lattice constants of the layer and the substrate under the tetragonal distortion, respectively. Unlike the analysis of the fully strained layer, the in-plane lattice constant of the partially relaxed epitaxial layer $a^{//}_l$ should be separately measured as it is not identical to that of the substrate. The in-plane lattice constant of the epitaxial layer can be obtained by performing two consequent asymmetric scans with different incident angles. The incident angles of the scans are determined from the tilt angle of the diffraction plane of the epitaxial layer against the substrate. On the other hand, a two-dimensional scan on the reciprocal space can provide more detailed information on the in-plane and vertical-direction lattice-constant distortion, degree of the layer relaxation, and the composition of the layer. This technique is called reciprocal space mapping (RSM).

For a better understanding of the principle of RSM, the specimen, the incident beam, and the scattered beam are shown on the reciprocal space in Figure 2-12. The Q_x- and Q_y-axis represent the directions parallel and perpendicular to the sample surface, respectively. The lattice points of the layer and the substrate are also shown as gray ellipses in Figure 2-12.

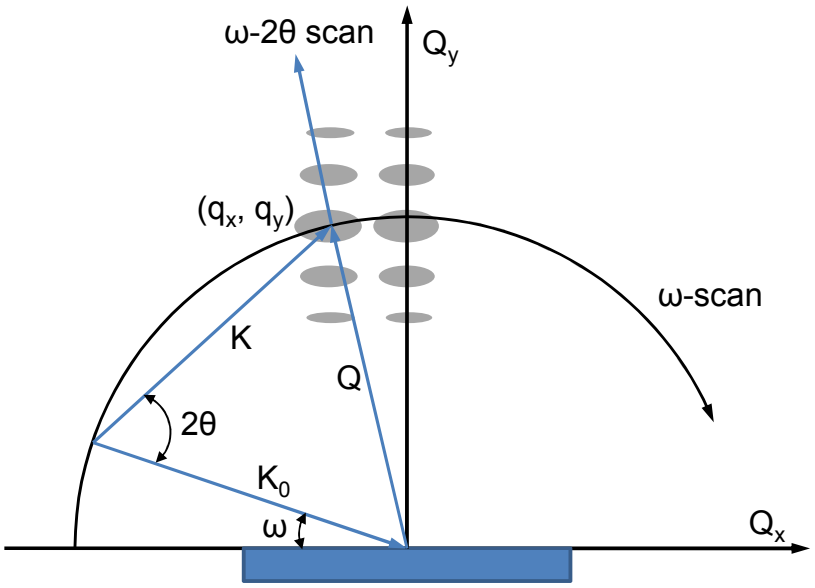

Figure 2-12. Reciprocal space representation of the ω-scan and ω-2θ-scan along with Ewald's Sphere.

In Figure 2-12, K_0 vector represents an incident X-ray beam, and K is a vector of the scattered beam. The angle between the vector K_0 and the surface of the specimen is labeled as ω, and the angle between the detector and the specimen is shown as 2θ. The scattered vector Q at a certain reciprocal lattice point (q_x, q_y) is related with these vectors as follows:

$$Q = K - K_0 \,. \tag{2-20}$$

Therefore, these three vectors form a triangle. This triangle defines a sphere which is centered at the origin of the Q vector and intersects two other vertexes of the triangle. This sphere is known as Ewald's Sphere, and it represents the trace of the HR-XRD scan in the reciprocal space. The coordinates of the reciprocal point (q_x, q_y) can be represented by using ω and 2θ through a simple geometric calculation as follows:

$$q_x = \frac{2}{\lambda}\sin\theta\cos(\omega - \theta), \text{ and} \tag{2-21}$$

$$q_y = \frac{2}{\lambda}\sin\theta\sin(\omega - \theta). \tag{2-22}$$

Therefore, an ω-scan that changes only the ω angle by rotating the specimen makes the triangle consisted with the K and K_0 vector rotate around the origin of the Q vector, as shown in Figure 2-13. On the other hand, an ω-2θ-scan changes the angles of the specimen (ω) and the detector (2θ) at the same time, and the triangle shows a vertical transformation, as shown in Figure 2-14.

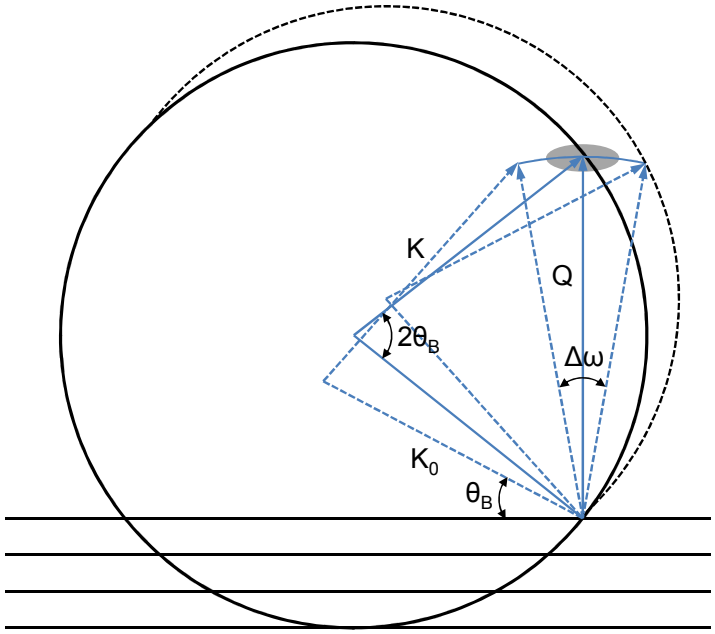

Figure 2-13. Illustration of an ω-scan in the reciprocal space along with Ewald's Sphere.

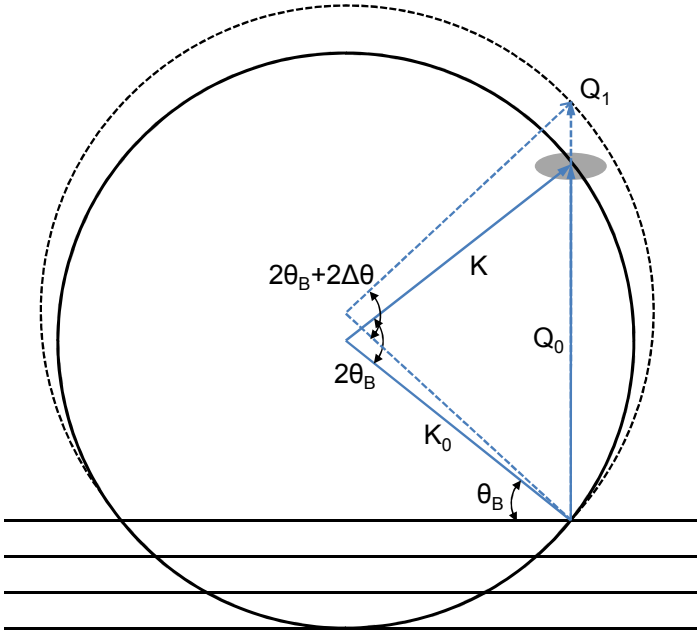

Figure 2-14. Illustration of an ω-2θ–scan in the reciprocal space along with Ewald's Sphere.

Therefore, one can obtain a two-dimensional map of a certain area in reciprocal space by repeating ω-2θ-scans at different ω values. In case of a DCD configuration, the detector is wide open, and it has a very low resolution along the ω-axis; the detector integrates and records the intensity of the scattered beam for a wide angular range without separating closely located lattice points. For a precise analysis of the reciprocal lattice points, an analyzer crystal is attached in front of the detector so that the detector can receive the scattered beam from a very narrow angular range. This configuration is called as triple-crystal diffraction (TCD) or triple-axis diffraction (TAD), because the analyzer crystal enhances the angular resolution along with the ω-axis, effectively providing an additional axis. The result of RSM is recorded in angular units, and it should be converted into reciprocal lattice units (RLUs) through Equation 2-21 and 2-22 for a numerical analysis. A result of RSM on an AlGaN layer grown on an AlN/sapphire substrate and its reciprocal space representation are shown in Figure 2-15.

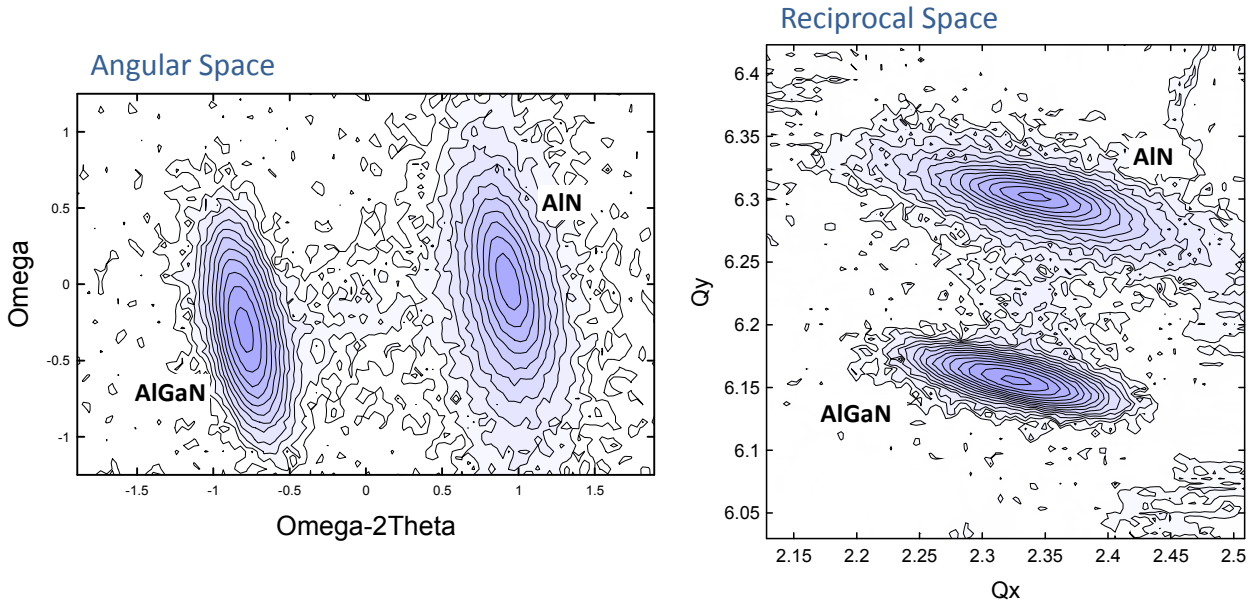

Figure 2-15. Angular space and reciprocal space representation of the RSM of an AlGaN layer grown on an AlN/sapphire substrate.

In the reciprocal space representation of RSM, the peak separation along with the each axis provides distinct information; the peak separation in the Q_y axis represents the difference of the lattice constants in a vertical direction, while the separation in the Q_x axis indicates the difference of the in-plane lattice constants. Therefore, unlike an ω-2θ-scan that provides information on the vertical-direction lattice constant only, RSM can determine the strain status and the composition of the layer independently and simultaneously. In Figure 2-15, the AlGaN layer is partially relaxed to the underlying AlN layer, because the peaks from the layer and the substrate are not aligned along with the Q_y axis. Also, the alloy composition of the AlGaN layer is determined from the position of the peaks in the reciprocal space. According to the calculation, the layer is approximately 65% relaxed, and it contains around 47% of aluminum.

All XRD measurement results in this work are taken using a Philips X'Pert MRD (Material Research Diffractometer) HR-XRD with a Cu $K_{\alpha 1}$ source and four Ge (220) crystals as a beam conditioner. The X'Pert system has two separated detector optics; detector path 2 has a typical DCD

configuration for a rocking curve measurement, and detector path 1 is equipped with a Ge (110) channel-cut crystal that is aligned to the (220) reflection as an analyzer crystal for a TCD scan.

2.4 Photoluminescence

Photoluminescence (PL) is a measurement technique that is widely used in the analysis of the optoelectronic device structures. This technique provides a non-destructive method to obtain information on the internal optical processes and the optical quality of the material [26]. When a material in an equilibrium state is excited by photons whose energy is larger than the bandgap of the material, electron-hole pairs are generated inside the material. They return to the equilibrium state via a radiative or non-radiative recombination process, and the number and the wavelength of the photon emitted during the radiative recombination process are recorded to complete a spectral plot. The spectral plot delivers information on the bandgap of the material, various mid-states and defect levels, and the optical quality of the layer. The peak wavelength λ in the PL spectra is directly related with the bandgap energy of the layer E_g through the following equation:

$$E_g = \frac{hc}{\lambda}, \tag{2-23}$$

where h is Planck constant. We used an RPM2000 system from Accent Optical Technologies for PL measurements in this study. A 266-nm Q-switched Nd:YAG laser is used for the material excitation. The incident laser light is attenuated up to 7.5× by the attenuators, delivering various laser powers from 0.4 mW (5 W/cm^2) to 3.1 mW (38 W/cm^2). The detection range of the charge-coupled device (CCD) detector is from 300 nm to 1300 nm (up to 4.698 eV). In a typical PL measurement for the visible-light LED structure, the excitation laser power of 1.4 mW (17 W/cm^2), a grating of 600 groves/mm, and a slit with 0.1 mm width were used.

2.5 Electroluminescence

Electroluminescence (EL) is another widely used characterization method to analyze the optical properties of the device structure. While the PL technique uses a laser to excite carriers, EL utilizes the electric current to inject carriers and to cause radiative recombination inside the material structure. Therefore, the sample needs to have a complete device structure with the contact layers that make the injection of the current through the metal probes possible. An external current source or a semiconductor parameter analyzer is commonly used to inject a constant amount of the current.

In the electroluminescence process, excess carriers are injected from the metal contacts and radiatively recombine in the active region to generate photons, and the detection and data-acquiring process is very similar to that of the PL technique. However, EL technique can provide the emission characteristics and the emission intensity of an actual device in operation in addition to the emission spectra. We used Keithley Model 2400 Series Source Meter as a current source. The photon-emission spectra were captured by using Ocean Optics HR2000-CG-UV-NIR spectrometer (detection range of 200 – 1100 nm) with a composite grating and a 2048-pixel CCD Linear Image Sensor controlled by a LabVIEW® software.

2.6 Atomic-Force Microscopy

Atomic-force microscopy (AFM) is a very useful tool to observe the surface of the specimen in three-dimension and in sub-nanometer scale [27,28]. A sharp silicon tip traveling on the sample surface is used to physically collect information of the surface morphology of the sample. The tip is attached to a flexible cantilever extending from a rigid substrate, and a piezoelectric driver and the feedback loop produce a raster-type scan motion while maintaining a certain distance between the tip and the sample surface in response to the surface morphology. The cantilever converts the

morphology of the sample surface into a vertical motion, and it is then translated into the height information by using an optical method, most commonly, the reflection of the laser beam. The laser beam is incident into the backside of the cantilever and reflected toward the detector. The bending of the cantilever occurred by a contour on the sample surface causes a shift of the beam spot on the detector. The controller converts this shift into the height information and completes a three-dimensional height map by repeating this process for a certain scan area. A schematic diagram of the AFM system is shown in Figure 2-16. A scan area is consisted with multiple fast axis scans and a slow axis scan. The piezoelectric driver has two drive directions, and one of them becomes a fast axis, while another becomes a slow axis to cover a two-dimensional scan area. The slow axis and the fast axis of the piezoelectric driver are shown in Figure 2-17.

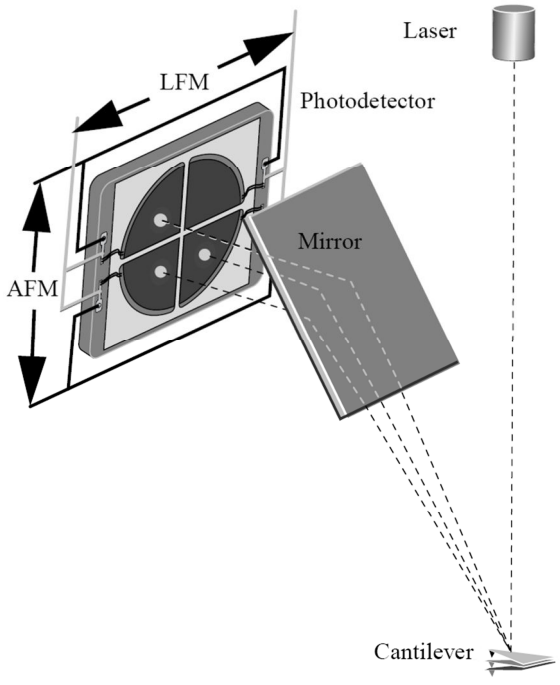

Figure 2-16. Schematic illustration of an AFM system [28].

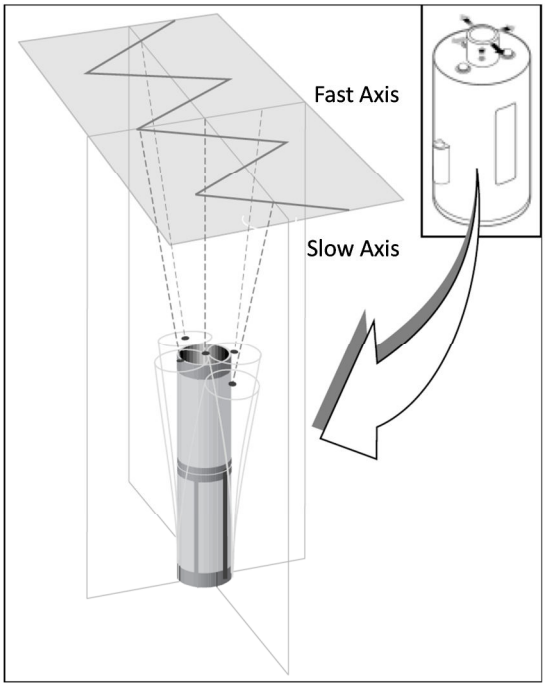

Figure 2-17. The fast axis and the slow axis of the piezoelectric driver [28].

AFM has two measurement strategies: contact mode and non-contact mode. In the contact mode, the probe tip and the sample are in physical contact to trace the surface morphology. In the non-contact mode, in the contrary, the probe tip floats several hundred angstroms above the sample surface, and the height profiling is done by a Van der Waals interaction. Because the interaction force is very small (around 10^{-12} N), direct detection of the bending of the cantilever is very difficult. Instead, the cantilever is oscillated near its resonant frequency (typically from 100 to 500 kHz) and the phase- or the frequency-shift of the oscillation caused by the interaction between the tip and the sample is detected. The non-contact mode scan is useful in measuring a soft specimen or a biological sample that contains water, because the damage on the specimen can be minimized. The distance and the interaction force between the probe and the sample with the corresponding AFM measurement modes are shown in Figure 2-18.

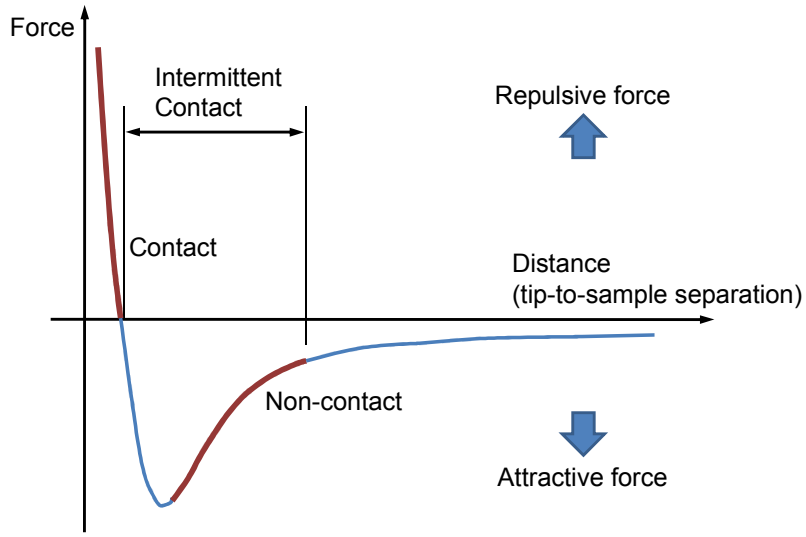

Figure 2-18. The tip-to-sample distance and the corresponding interaction forces.

The tapping mode is a recent advancement over the conventional AFM measurement modes. It overcomes the problems of both contact mode and non-contact mode AFM by alternately placing the probe tip in contact with the surface to provide a high resolution while avoiding the dragging of the tip across the surface and minimizing the damage on the sample surface. The cantilever oscillates near its resonant frequency as in the non-contact mode, but the amplitude is much larger (50 – 200 nm), and the surface morphology is measured by "tapping" the tip on the sample surface. In this study, all AFM observations were performed by using Veeco Dimension 3100 AFM system operating in the tapping mode with NSC Series 16 probes. The NSC Series 16 probe has a cantilever length of 230 μm with a typical resonant frequency of 325 kHz and the force constant of 40 N/m.

2.7 Transmission-Line Measurement

Transmission-line measurement (TLM) method is a measurement technique developed to analyze the resistances of the semiconductor layer and the metal-semiconductor contact. Unlike conventional techniques such as two-terminal measurements, contact-front resistance test or contact-

end resistance test, TLM can provide both the sheet resistance and the contact resistivity simultaneously with a good accuracy through a relatively simple process. The TLM employs a test pattern produced by a mesa etching and a deposition of multiple metal contact pads. A typical TLM pattern is shown in Figure 2-19. In Figure 2-19, the spacing between the metal contact pads has multiple values from d_1 to d_6. Also, the mesa etching around the pattern ensures the confinement of the current flow into the area between the metal pads.

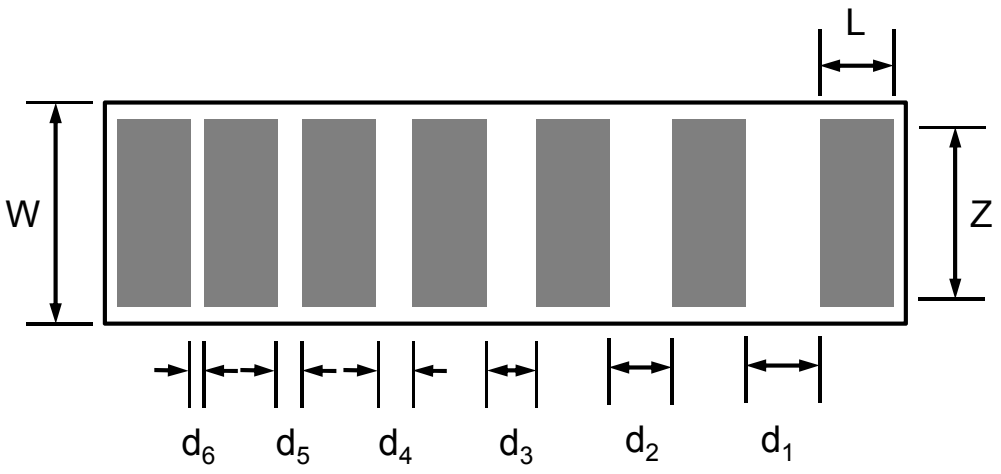

Figure 2-19. A typical TLM pattern showing the semiconductor mesa with metal contact pads.

The specific contact resistance ρ_c and the sheet resistance R_s can be obtained by plotting the resistances between the two contact pads as a function of the contact-pad spacing. An example of the plot of the measured resistances versus the contact spacings is shown in Figure 2-20.

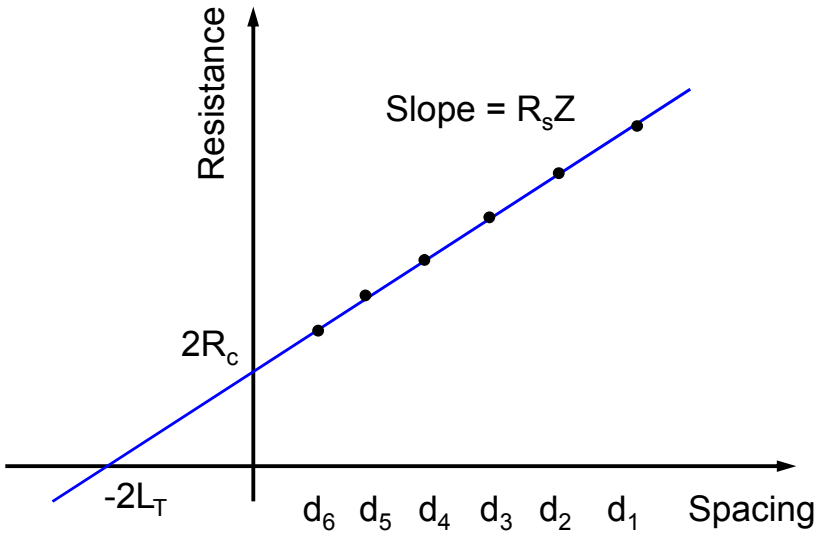

Figure 2-20. Plot of the measured resistances along with the contact-pad spacings.

In the plot shown in Figure 2-20, the sheet resistance of the semiconductor layer is calculated through the following equation:

$$R_s = slope \cdot Z, \tag{2-24}$$

where Z is the height of the metal pads as shown in Figure 2-19. On the other hand, the y-intercept of the linear plot in Figure 2-20 corresponds to twice the contact resistance, $2R_c$. Also, the x-intercept of the plot is twice the transfer length, $2L_T$. The transfer length is defined as the distance from the edge of the metal pad to the point that the contact voltage is $1/e$ of its maximum value. With these parameters, the specific contact resistance ρ_c can be calculated from the following equations:

$$R_c = R_s \cdot L_T \text{ , and} \tag{2-25}$$

$$\rho_c = L_T \cdot Z \cdot L_T \text{ .} \tag{2-26}$$

2.8 DC Current-Voltage Measurement

DC current-voltage measurement technique analyzes the electrical properties of the device structures or the fabricated devices by applying a voltage bias and measuring the current. Two-port devices such as LEDs will produce a single current-voltage curve, while three-port devices such as HFETs and HBTs will have a "family" of the curves that is a set of the multiple current-voltage relations between two electrodes measured at different bias levels of the third electrode. The current-voltage measurement results provide a wide range of the device information including the series resistance, forward voltage, leakage current, capacitance, inductance, gain, and the transconductance. We used an Agilent Model 4156C semiconductor parameter analyzer connected to a personal computer via a General Purpose Interface Bus (GPIB) to conduct the DC current-voltage measurement. Interactive Characterization Software's Metrics software is used to control the 4156C and to automate the measurement process.

2.9 Sentaurus

Sentaurus is a technology computer-aided design (TCAD) package which provides a wide range of functionalities to simulate electrical, thermal, and optical behaviors of the semiconductor devices. It can describe two-dimensional or three-dimensional device structures and includes numerous physical models to find solutions on various problems including the carrier density, conduction and valence band energy, piezoelectric and spontaneous polarization field, AC and DC current-voltage curve, heat transfer, and optical emission. Also, the command script based on the Scheme scripting language provides a high flexibility in the automation of the problem solving, result compilation, and data visualization. In this work, Sentaurus is used to clarify the concept of the new device structures by predicting their electrical properties prior to the actual growth and fabrication.

The basic workflow of the Sentaurus and the corresponding software tools to be used are shown in Figure 2-21.

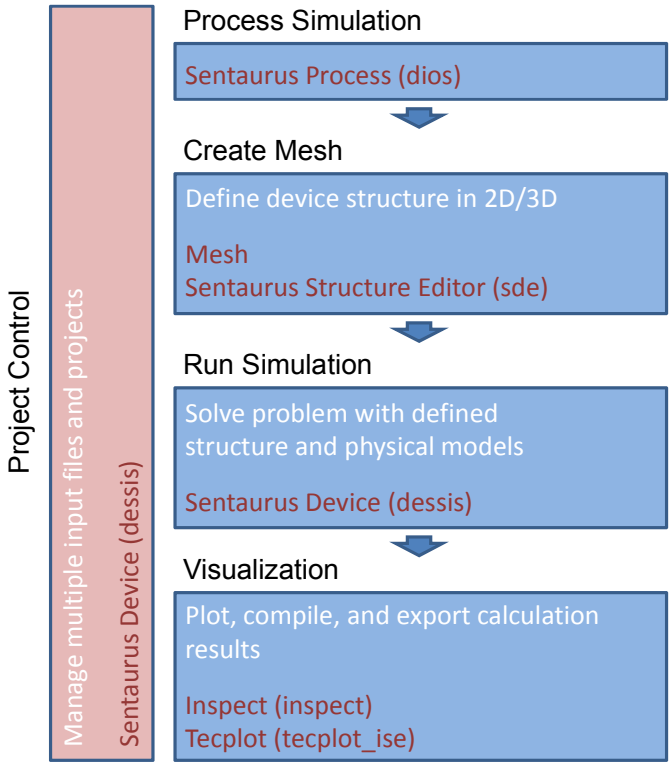

Figure 2-21. The overall workflow and the corresponding software tools of the Sentaurus.

CHAPTER 3 MOCVD SURFACE TEMPERATURE SIMULATION

3.1 Introduction

Foreign substrates whose lattice constants and thermal expansion coefficients are mismatched to those of the Group III-nitride materials have generally been employed in the growth of epitaxial structures of the III-nitride materials, since the bulk growth of GaN (or AlN) crystals from a melt for the preparation of native substrates is extremely difficult due to a very high vapor pressure of nitrogen at the melting temperature of GaN. Among many candidates of foreign substrates having the same crystalline symmetry of the growth surface as that of the Group III-nitride materials, sapphire (α-Al_2O_3), and 4H- and 6H-silicon carbide (SiC) substrates have been popular choices due to not only the wide availability of high-quality materials but also their chemical and thermal stability at elevated temperatures for the epitaxial growth of the III-nitride semiconductors. Sapphire substrates have been widely used because of their reasonable cost, despite its large lattice mismatch of 14%. SiC substrates are considered a viable alternative substrate choice with a much smaller lattice constant mismatch (~1%) and a reduced thermal expansion coefficient mismatch [29]. SiC substrates also have an advantage in vertical-conducting devices and high-power devices with lower device cooling requirements because of their high electrical and thermal conductivities. Silicon (Si) substrates are also a promising candidate for the low cost of the substrate and the integration of the III-nitride semiconductors with Si technology. Recently, GaN and AlN "bulk" substrates have been developed to be available for the growth of a homoepitaxial structure with a low defect density and lattice- and thermal-matching. However, the use of various foreign and native substrates in the growth process introduces several technical challenges that are generally not observed in other Group III-V semiconductors such as InP- and GaAs-based materials whose lattice constant, thermal-expansion coefficient, and thermal conductivity are similar each other. Significantly different lattice constants and thermal-expansion coefficients of the substrates for the Group III-nitride materials often leads to

inconsistent growth results. Furthermore, the differences in the thermal conductivity and thickness of different substrates result in the difference in the temperature at the growing-surface of the Group III-nitride semiconductors that is one of the important process parameters in the epitaxial growth - the quality, the composition, and the growth rate of the materials are very sensitive to the growth temperature [30,31]. Especially, the growth of high-aluminum (Al)-containing or high-indium (In)-containing materials requires a very precise control on the temperature of the actual growing-surface because of low adatom mobility of aluminum [32] and high equilibrium vapor pressure of indium [33]. In many cases of the growth of epitaxial structures on different substrates as part of a substrate comparison study, the growth is carried out at the same set-point of the growth temperature (often in the same batch of wafers in a growth run) in an attempt to ensure the same nominal growth conditions. However, this attempt may lead to a significantly different actual temperature of the growing-surface because of the different properties of substrates. In addition, the surface temperature for the epitaxial growth depends not only on the thermal conductivity of the substrate, but also on the surface heat loss by the forced convection that is a function of the chamber design and the flow rate of a carrier gas combined with precursors in the typical MOCVD. Therefore, it is important to investigate these factors to estimate the actual surface temperature for the growth of high-quality and well-controlled Group III-nitride materials grown on different substrates with different growth conditions in various reactor systems. In this chapter, we have investigated the actual surface temperature of various substrates and its influence on the characteristics of the resulting epitaxial films via a theoretical calculation and an experimental layer growth. The effects of substrates with different thermal properties and thicknesses, and of the growth conditions are investigated. In addition, the effects of the hydrodynamics on the surface temperatures of different substrates are also investigated. The results of AlGaN epitaxial layers grown on native and sapphire substrates are also discussed as an experimental demonstration of the calculation results. The temperature gradient in the vertical

direction from the backside to the surface of the each substrate was analyzed during the FEM calculations.

3.2 The Heat Transfer Calculation Model

The actual surface temperature of the most common substrates employed for the Group III-nitride semiconductor growth is studied by employing the one-dimensional (1D) finite element method (FEM). The schematic model used to describe the heat transfer between the susceptor and the substrate is shown in Figure 3-1. The model is consisted with a susceptor that has a certain fixed temperature, a substrate with a certain thickness that transfers heat from the underlying susceptor to its surface, and a carrier gas passing the top of the substrate and the susceptor.

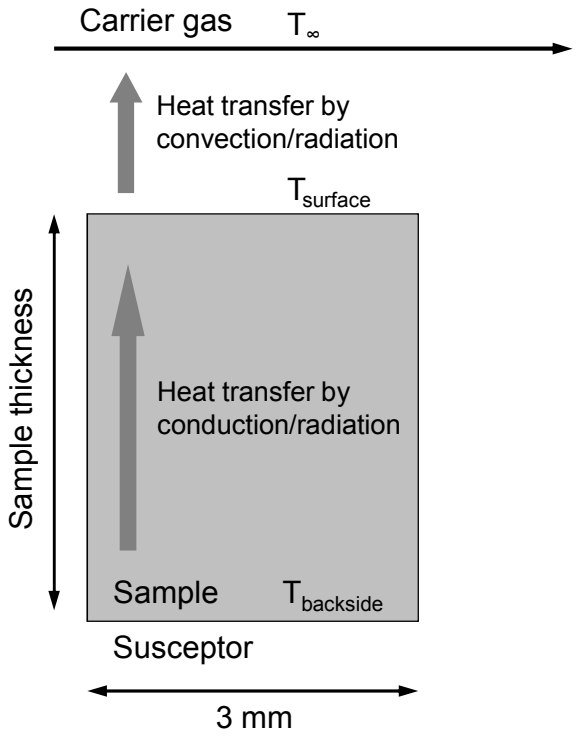

Figure 3-1. Schematic illustration of the model used in the heat transfer calculation.

In the calculation, sapphire, SiC, Si, GaN, and AlN substrates having the same thickness were considered. The temperature for the backside of each substrate (or the surface of the susceptor) was set to 1150 °C and 780 °C that are representative growth temperatures of AlGaN and InGaN materials, respectively. Thermal conduction and radiation were considered as the major method of the heat transfer from the susceptor to the substrates. The increase of a vertical thickness caused by the thermal expansion was ignored, since the thickness change caused by the thermal expansion is negligibly small (e.g., 6.1×10^{-8} mm for a 2 mm-thick AlN substrate at 1150 °C). The initial temperature of the carrier gas entering the chamber was set to room temperature, as we assumed that the reactor does not have a pre-heater for the sources. Also, as in many reactors whose volume of the chamber is small, the velocity of carrier gas passing the susceptor is relatively high, leaving short time to raise the temperature significantly from its initial temperature. Therefore, we also assume T_∞, the reference temperature of carrier gas passing top of the chamber, to be room temperature. The calculation was performed on a cylindrical area with a diameter of 3 mm located at the center of the substrates. Heat loss from the sidewall of the area was not considered, as the target area is small compared to the diameter of the substrates and adjacent area that has the same temperature acts as a thermal insulator. Therefore, heat loss will occur only at the surface of each substrate by forced convection of the carrier gas. Various thermal properties of the substrates and carrier gases we used in the calculations, including the thermal conductivities, specific heat capacity, and the viscosity, are summarized in Table 3-1 and Table 3-2.

Table 3-1. Thermal properties of hydrogen and nitrogen at 300 K, 1 bar which is used for the theoretical calculations [34].

Materials	Thermal conductivity, k (W/m·K)	Specific heat capacity, c_p (kJ/kg·K)	Viscosity, μ (Pa·s)	Fluid density, ρ (kg/m^3)

(Table 3-1 continued)

Hydrogen	0.1877	14.31	8.9×10^{-6}	0.08
Nitrogen	0.0261	1.041	17.9×10^{-6}	1.125

Table 3-2. Thermal properties of the substrates used for the theoretical calculations. The thermal conductivities of the substrates are measured at 1100 °C and the transmittance value was estimated with a substrate thickness of 430 μm.

Materials	Thermal conductivity, *k* (W/m·K)	Thickness	Transmittance	Emissivity
Sapphire	10.5[34]	430 μm	0.82[35]	0.02[35]
AlN	40.0[36]	430 μm	0.76[37]	0.51[38]
GaN	50.0[39]	430 μm	0.71[40]	0.50[41]
SiC	47.0[42]	430 μm	0.44[43]	0.78[44]
Si	26.0[45]	430 μm	0.54[46]	0.70[47]

The transmittance and emissivity of the substrates are values in the wavelength of ~2 μm, because at 1150 °C maximum radiation energy is transferred from the susceptor to the substrates through this wavelength region. Other parameters required for describing the flow geometry inside the chamber such as the Reynolds number, Prandtl number, and convective heat transfer coefficients can be found in Ref. 48.

In the FEM calculation, the heat loss at the surface of the substrates is expressed by a force matrix, while heat transfer is described by a stiffness matrix. The convection heat transfer at the surface is the main component of the force matrix, and the conduction heat transfer inside the substrate and the heat loss by the convection at the end node consist the stiffness matrix. For the heat transfer

by radiation, the difference between the radiative heat transferred from the susceptor and lost at the surface of the substrate was added to the force matrix as a heat flux. The convective heat transfer coefficient, h, can be determined by the Reynolds number and the Prandtl number that reflect the carrier gas composition, the gas flow rate, and the design of the chamber. The Reynolds number and Prandtl number can be calculated by using following equations:

$$Re_x = \frac{\rho u_\infty x}{\mu}, \text{ and} \tag{3-1}$$

$$Pr = \frac{\mu c_p}{k}, \tag{3-2}$$

where Re_x is the Reynolds number, Pr is the Prandtl number, ρ is the density of the carrier gas, u_∞ is a uniform velocity, x is the length of the flowing ground, μ is the viscosity, c_p is the specific heat capacity, and k is the thermal conductivity. These numbers are related to the convective heat transfer coefficient by the Nusselt number:

$$Nu = 0.664 Re_x^{1/2} Pr^{1/3} = \frac{hD}{k}, \tag{3-3}$$

where D is the characteristic length. Similar values of h will cause similar amount of heat loss from the surface, and the environmental difference between the growth chambers can be summarized into a single parameter. The heat transferred by radiation was calculated by using Stefan-Boltzmann Law and Planck's distribution with the emissivity and transmittance of each substrate.

3.3 The Heat Transfer Calculation Results

The calculated transient of the surface temperature of various substrates with the change in the convective heat transfer coefficient, *h*, is shown in Figure 3-2. The substrates were assumed to have a thickness of 430 μm.

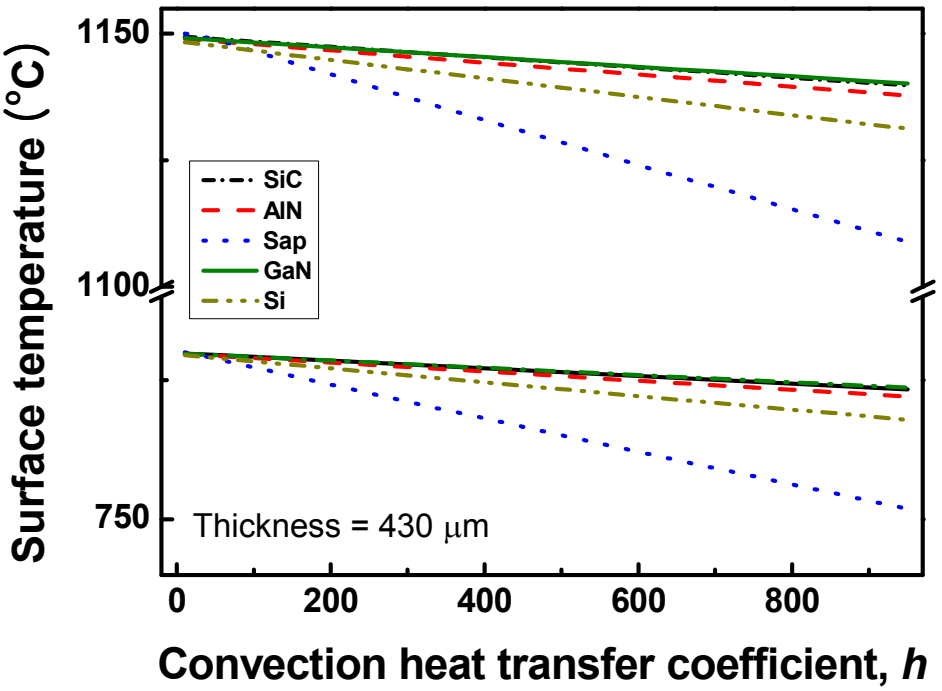

Figure 3-2. The dependence of the calculated growing-surface temperature of the substrates upon the change of the convection heat transfer coefficient *h* at the AlGaN growth temperature (upper) and the InGaN growth temperature (lower).

If the value of *h* is small (*h*<100), the surface temperature difference in the various substrates will be small regardless of their thermal conductivity. However, the temperature dependence upon the substrate materials becomes significant with an increase in *h*. The surface temperatures of the GaN or SiC substrates are higher than that of a sapphire substrate by ~30 °C for 1150 °C (of backside temperature of the substrate) and by ~20 °C for 780 °C with an *h* of 900. It is clear that a substrate with a higher thermal conductivity will transfer more heat from the backside to the surface, resulting in a higher substrate surface temperature. At the same time, the heat loss from the surface is

proportional to the temperature difference between the surface and the carrier gas (assumed to be at room temperature), and high-thermal-conductivity substrates will lose more heat at the surface. However, because of the relatively small substrate thickness, the difference in the conduction heat transfer will override the difference in the heat loss at the surface and will lead to higher surface temperatures in substrates of which the thermal conductivity is high. Therefore, in most MOCVD reactors having *h* values from 150 to 700, the surface temperature of sapphire substrates is predicted to be lower than those of SiC, AlN, or GaN substrates by more than 10 °C at both the AlGaN and InGaN nominal growth temperatures. This surface temperature difference is large enough to affect the layer quality and the alloy composition.

However, the assumption we made about the thickness of substrates is not always true. In many cases, the bulk substrates have various thicknesses because of their unique wafering process. For example, the thickness of the AlN substrate used in this experimental study is ~2 mm. Thicker substrates will have a reduced heat transfer from the backside, and it will show lower surface temperature. The change of the surface temperature with the different thickness of substrates from 100 μm to 2.5 mm at selected *h* values is shown in Figure 3-3.

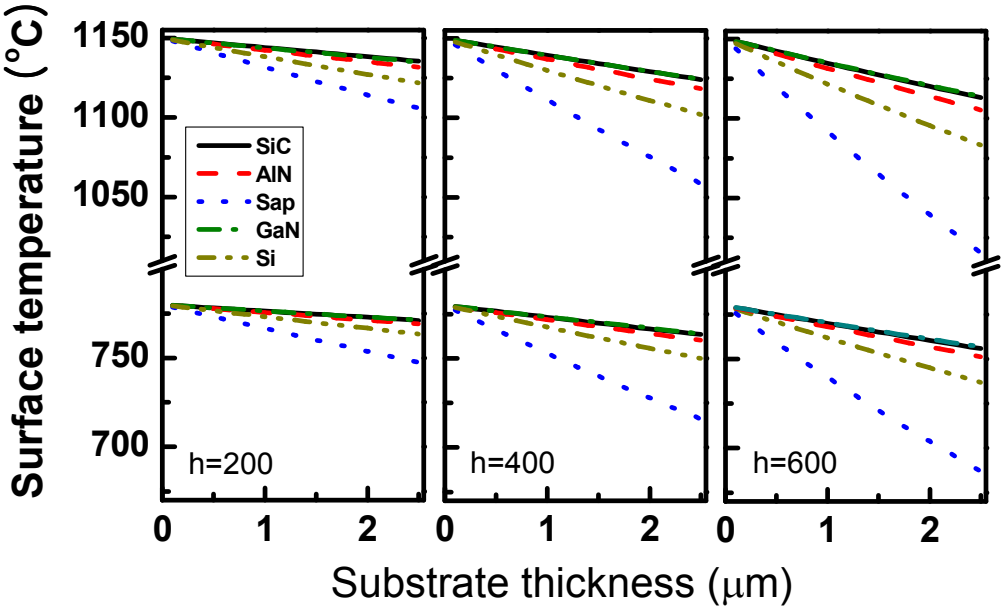

Figure 3-3. The dependence of the calculated growing-surface temperature of the substrates upon the thickness of the substrates for the selected *h* values at the AlGaN growth temperature (upper) and the InGaN growth temperature (lower).

In Figure 3-3, the surface temperature tends to decrease with the thickness of the substrates under all *h* values. Furthermore, this tendency becomes significant as the value of *h* increases. This means that a 2 mm-thick bulk AlN substrate has similar surface temperature with that of a commonly used 430 μm-thick sapphire substrate under small *h* values ($h<200$), and the surface temperature of the thick bulk AlN substrate will be at least 10 °C lower than the that of a sapphire substrate if the *h* value is high ($h>400$). This temperature discrepancy will be expanded to more than 10 °C if thicker AlN substrates are used in AlGaN growth.

In addition, the surface temperatures are affected by the carrier gases. In the case of InGaN growth, nitrogen (N_2) is used as a carrier gas instead of hydrogen (H_2) in order to avoid the etching effect of H_2 [49]. Their different physical- and thermal-properties can change the amount of heat loss at the surface and the surface temperature. Although N_2 has higher fluid density and dynamic viscosity, its thermal conductivity and specific heat capacity is much lower than those of H_2, and they

contribute to the smaller convection heat transfer coefficient of the reactor. As a result, a reactor that has h=600 with H_2 carrier gas will have h=225 when it has N_2 as a carrier gas, and the surface temperature difference between the sapphire and the bulk GaN substrate with the same thickness will be 5 °C at the InGaN growth temperature of 780 °C. Therefore, N_2 carrier gas will cause a smaller temperature difference than H_2 carrier gas. Also, the temperature difference will become larger if a thicker bulk GaN substrate is used. The calculated surface temperature of each substrate in typical growth conditions of AlGaN and InGaN with h of 600 (H_2 carrier gas) and 225 (N_2 carrier gas) are summarized in Table 3-3.

Table 3-3. Summary of the surface temperatures of substrates at selected growth temperatures with convection heat transfer coefficient h of 600 (H_2 carrier) and 225 (N_2 carrier).

	Thickness (μm)	Substrates				
		Sapphire	AlN	GaN	SiC	Si
AlGaN growth temperature with H_2 carrier gas (1150 °C, h=600)	430	1124.1	1141.9	1143.6	1143.3	1137.5
	2500	1015.6	1105.4	1114.6	1113.1	1083.3
InGaN growth temperature with H_2 carrier gas (780 °C, h=600)	430	762.1	774.9	775.8	775.7	772.1
InGaN growth temperature with N_2 carrier gas (780 °C, h=225)	430	773.4	777.9	778.3	778.3	776.8

3.4 The Experimental Results on the Surface Temperature

The effect of the surface temperature on the layer growth results was experimentally confirmed by growing AlN/AlGaN superlattice (SL) structures simultaneously on a bulk AlN substrate and an AlN/sapphire template/substrate. The AlN and AlGaN epitaxial layers were grown in a Thomas Swan Scientific Equipment CCS 6×2" MOCVD reactor system. The AlN/sapphire templates were prepared on a (0001) sapphire substrate using a conventional two-step growth employing a low-temperature AlN buffer layer. The bulk AlN substrates were grown using the sublimation-recondensation of high-purity AlN powder and then sliced into wafers [50]. The epitaxial layers were grown at a temperature (T_g) of 1150 °C. Note that this temperature was measured at the surface of the SiC-coated graphite susceptor using a LayTec EpiTT®, and it is not necessarily the actual temperature of the growing-surface. The crystalline quality and the alloy composition were investigated by HR-XRD, and the strain status of the epitaxial layer was measured by RSM. The thickness of the AlN native substrate was 2.1 mm, while that of the sapphire substrate was 430 μm. This can serve as a good example that can demonstrate the effects of both thermal conductivity and thickness of different substrates on the surface temperature. The separation between the showerhead and the susceptor in our growth chamber is ~1 cm, and the flow rate of the H_2 carrier gas used during the conventional AlGaN growth is ~20 l/min. Under these conditions, h is calculated to be ~600. According to the previous calculation with this substrate thickness difference (also with the effect of the different thermal conductivity), a bulk AlN substrate is predicted to have a lower surface temperature than the sapphire substrate by ~10 °C. The AlN/AlGaN SL structure was grown by the following procedure. First, an AlN high-temperature "buffer layer" was grown on the substrate and the template. Then, an AlN/$Al_{\sim 0.8}Ga_{\sim 0.2}N$ SL and an $Al_{\sim 0.8}Ga_{\sim 0.2}N$/$Al_{\sim 0.65}Ga_{\sim 0.35}N$ SL were deposited. Finally, ~0.5-μm-thick $Al_{\sim 0.5}Ga_{\sim 0.5}N$ layers were grown on top of the SL layers. HR-XRD ω-2θ-scan results with (002) diffraction on the AlN/AlGaN SL layers grown on the bulk AlN substrate and the AlN/sapphire template are shown in Figure 3-4.

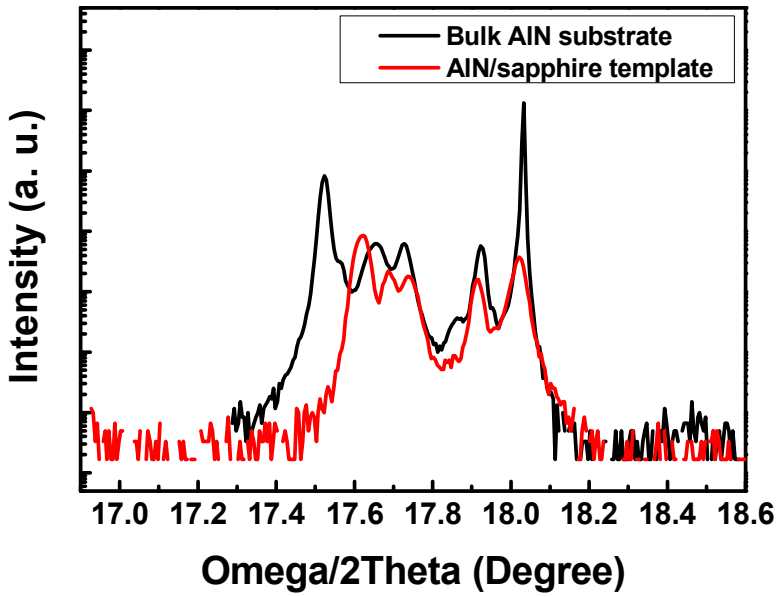

Figure 3-4. HR-XRD ω-2θ-scan results for the AlN/AlGaN SL samples simultaneously grown on a bulk AlN substrate and an AlN/sapphire template/substrate at 1150 °C.

The peaks from the AlN substrate and the AlN/sapphire template were located at the rightmost side, and four peaks from the upper layers appear subsequently on the left side. Unlike other HR-XRD peaks representing SL layers, the leftmost peaks from the 50% targeted AlGaN layers show a large position discrepancy between samples grown on different substrates. This peak position difference can originate from either a strain status difference, an actual composition difference, or both of them. By assuming that AlGaN layers on both substrates are fully relaxed, the aluminum composition of the 50% targeted AlGaN layer on the bulk AlN substrate is measured to be 15% lower than that of the comparable layer grown on the AlN/sapphire template. To confirm the strain status of the AlGaN layers, HR-XRD RSM around the asymmetric (105) reflection was measured and shown in Figure 3-5.

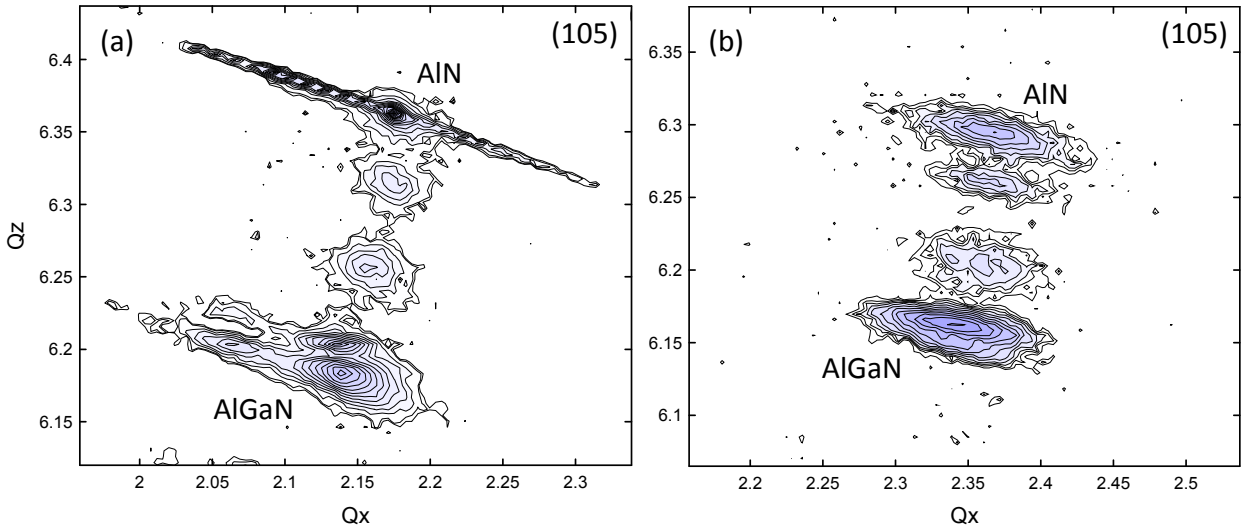

Figure 3-5. HR-XRD RSM observations of AlGaN SLs on (a) a bulk AlN substrate (b) an AlN/sapphire substrate in the (105) diffraction.

The degree of relaxation determined from the separation of the lattice vectors perpendicular and parallel to the surface for $Al_{0.35}Ga_{0.65}N$ and $Al_{0.5}Ga_{0.5}N$ layers on the bulk AlN substrate and the AlN/sapphire template is more than 90% for both samples. Therefore, the strain status difference is not the main reason of the peak position discrepancy in the HR-XRD rocking curve, and the surface temperature difference predicted in the previous calculation is believed to have caused the actual aluminum composition difference. As the temperature of the surface increases, the incorporation of gallium will be limited, resulting in higher aluminum composition on a "thin" sapphire substrate with a higher surface temperature than on a "thick" AlN substrate with a lower surface temperature. However, the 15% of the composition difference is somehow larger than that expected from the predicted 10 ^{o}C of the growth surface temperature difference. This implies that the actual surface temperature difference could be larger than the prediction, due to various factors such as chamber design-specific flow dynamics or a discrepancy from the theoretical calculation model which cannot be fully described by parameters used in the calculation.

CHAPTER 4 DEVELOPMENT OF THE LIGHT-EMITTING DIODES WITH AN InAlN ELECTRON-BLOCKING LAYER

4.1 Introduction

Driven by their significant improvements in the internal and external quantum efficiencies, the Group III-nitride-based LEDs are expected to be employed in displays and general lighting applications replacing conventional incandescent and fluorescent light sources in the near future. However, technical and economic challenges remain to be solved for the LEDs to be competitive in terms of their performance characteristics and the manufacturing costs. As mentioned above, one of the critical technical challenges to be addressed for high-brightness and high-power operations of the LEDs is a phenomenon commonly referred to as an efficiency droop that is observed as a reduction in the emission efficiency with the increasing injection current under the high current-density conditions. The consensus on this efficiency droop problem is that this problem is not a thermal issue (*i.e.*, Joule heating), but a fundamental problem associated with InAlGaN materials and their heterostructures.

However, this well-recognized problem is not completely understood. The origin of the efficiency droop was previously suspected to be related to the high defect-densities in combination with the carrier delocalization from the localized states in the active region of the light emitters [51, 52]. Recently published works have suggested several (possibly related and all partially contributing) causes of the efficiency droop, including Auger recombination processes [53,54,55], carrier spill-over [56,57], and limited hole-transport [58,59]. The Auger recombination processes describe the reduction of the photon-generation rate through the transfer of the electron-hole recombination energy toward a third carrier under a high carrier-density condition. The limited hole-transport theory suggests that the deficiency of the holes in the active region causes the significant decrease of the electron-hole pairs and the reduction of the radiative recombination. Each theory is supported by several observations. However, the carrier spill-over theory is widely accepted by the

industries as well as the academic fields as the most convincing origin of the efficiency droop problem, and most commercial devices incorporate a measure to reduce the carrier spill-over.

The carrier spill-over describes the traverse transport of the injected carriers over the active region followed by their recombination outside the active region at the high carrier-density conditions. In most cases, electrons with mobility much higher than holes have a greater chance to be spilled over into the *p*-type layer. The insertion of a wide-bandgap AlGaN material between the active region and the *p*-type hole-injection layer as an electron-blocking layer (EBL) has been suggested to suppress the escape of the electrons out of the active region [51]. However, recent studies suggest that the electron-confinement by a typical AlGaN EBL (with x_{Al}~0.2) is not sufficiently effective to solve the efficiency droop problem, especially because of the added polarization effects caused by the AlGaN [57]. In typical LED structures, an AlGaN EBL is located on top of a GaN barrier of the quantum-well (QW) active region, and the lattice mismatch between AlGaN and GaN generates a piezoelectric-polarization field in addition to the differential spontaneous-polarization fields. These polarization fields pull the conduction band downward at the AlGaN/GaN interface. As a result, the effective barrier height of the EBL is reduced, and the leakage of the carriers is not effectively suppressed [56]. The effective barrier height of the AlGaN EBLs can be augmented with a higher aluminum composition, and consequently, a wider bandgap and a larger conduction-band offset relative to GaN. However, incorporation of a high aluminum mole fraction into the AlGaN layer usually degrades the layer crystalline quality with the generation of strain-induced defects and leads to an even larger piezoelectric-polarization field. Also, an AlGaN EBL may not be compatible with all visible LEDs. The high optimum growth temperature of the AlGaN EBL can produce a significant thermal damage on the active region of the green and longer wavelength LEDs with an indium compositions of 0.2 or higher, degrading its luminescence characteristics [60].

InAlN with x_{In}~0.18, grown lattice-matched to GaN by MOCVD, has been used as the low-index material component of the distributed Bragg reflectors in the vertical-cavity surface-emitting

lasers [61], as a barrier layer in the heterostructure field-effect transistors [62,63], and as a cladding layer in the edge-emitting diode lasers [64]. $In_{0.18}Al_{0.82}N$ also has many attractive characteristics as an EBL material, including the ability to lattice-match to GaN and $In_xGa_{1-x}N$, a wide energy bandgap, a large conduction-band offset relative to GaN, and a relatively low growth temperature. In this chapter, the growth of the InAlN layers by using MOCVD and their use as a lattice-matching EBL with a higher electron-blocking efficiency will be studied.

4.1 Growth of the InAlN Layer by Using MOCVD

The optimum growth temperatures and pressures for InN and AlN are very different. InN is usually grown at a low temperature (~600 ^{o}C) and at a high pressure, while AlN is grown at a high temperature (~1300 ^{o}C) and at a low pressure condition. Because of these growth condition differences, there are many technical issues in the growth of the InAlN layers, such as a spinodal phase separation and a large immiscibility gap between InN and AlN that can cause a compositional fluctuation of the InAlN layer [65]. Therefore, the most critical factors on the growth of InAlN are believed to be the growth temperature and the growth pressure. To examine the influence of the growth conditions, InAlN test structures were grown under the various combinations of the growth temperatures and pressures. The InAlN test structures were constructed with 100 nm-thick InAlN layers grown on GaN/sapphire substrates. The layer thickness was measured by *in-situ* reflectance, and the indium composition was measured and confirmed by HR-XRD and RSM. The indium compositions of the InAlN test layers under various growth conditions are shown in Figure 4-1.

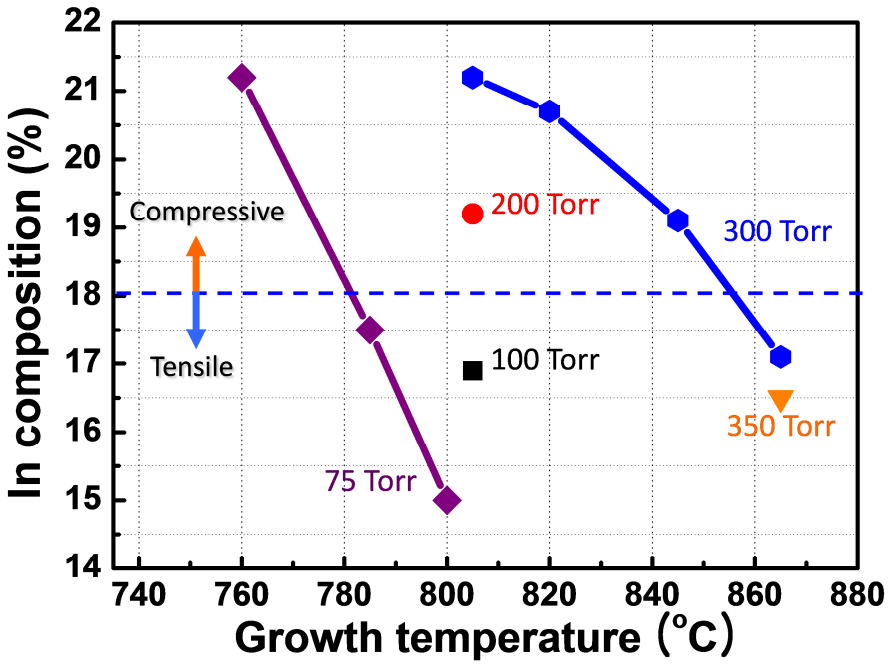

Figure 4-1. The dependence of the indium compositions in the InAlN test layers on the growth temperatures and the growth pressures.

As shown in Figure 4-1, the indium composition decreases with the increase of the growth temperature. This behavior is often observed in the growth of the InGaN layers and consistent with other reports about the growth of the InAlN layer [65]. The desorption of InN at the layer surface is enhanced and the indium alloy composition is reduced under the high growth temperature because of the much weaker chemical bonding of InN than that of AlN [66]. Also, the indium composition increases with the increase of the growth pressure under a fixed growth temperature. This can be accounted by a reduced incorporation of aluminum because of a reduction of the mobility of the aluminum adatom under a higher growth pressure. On the other hand, the adatom mobility is closely related to the surface morphology of the layer. The transition of the surface morphology of the InAlN layers along with the growth conditions observed by AFM is shown in Figure 4-2. The growth conditions are selected to maintain the similar indium composition in the grown InAlN layers.

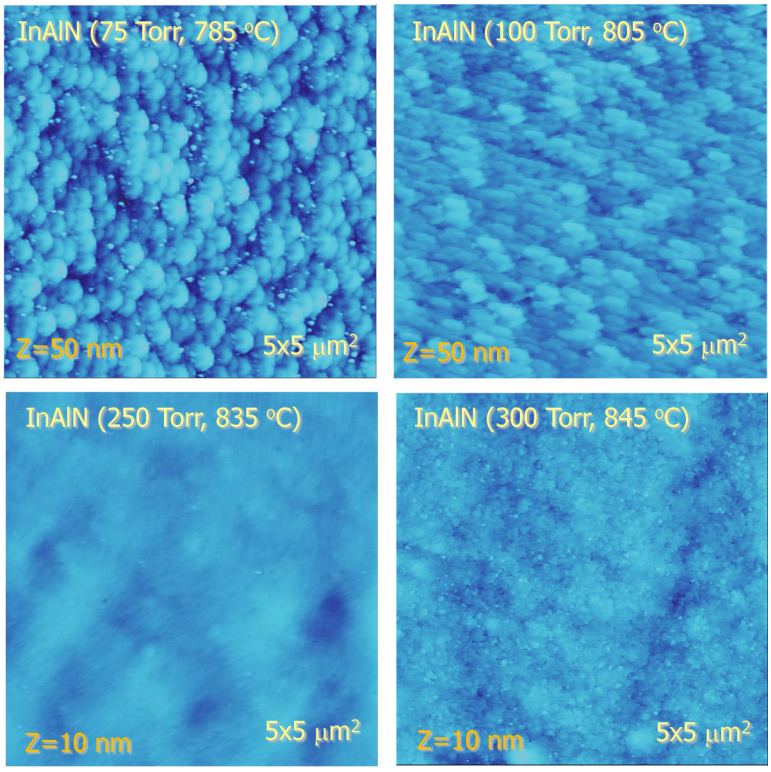

Figure 4-2. The surface morphologies of the InAlN layers with different growth pressures and growth temperatures observed by AFM.

In Figure 4-2, the improvement of the surface morphology with the decrease of the growth pressure and the increase of the growth temperature is clearly observed. The root-mean-square (RMS) surface roughness obtained from the AFM observation along with the layer growth conditions are shown in Figure 4-3.

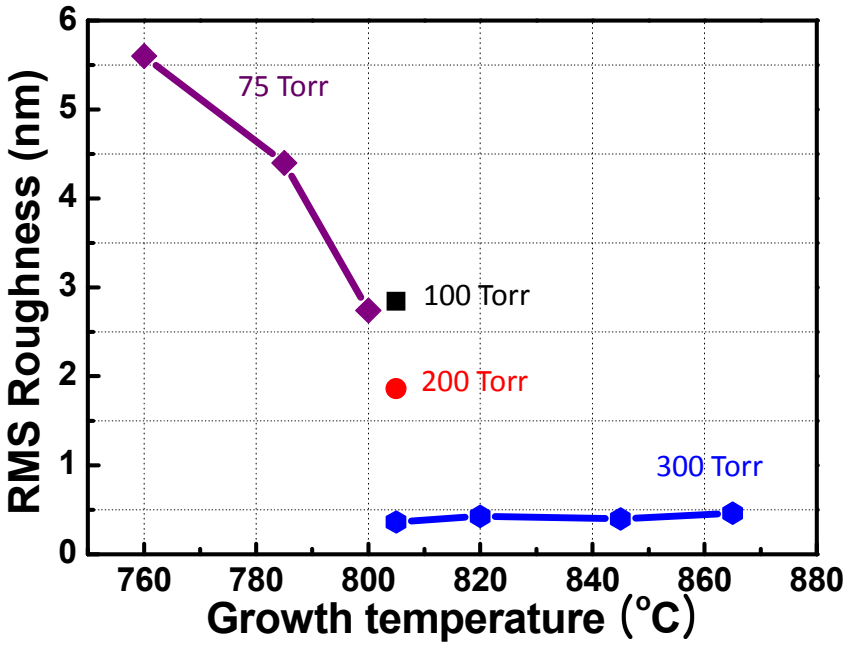

Figure 4-3. The dependence of the RMS roughness of the surface of the InAlN layers on the growth temperature and the growth pressure.

As shown by the results in Figure 4-3, the InAlN layers grown under a low pressure of 75 Torr show rather rough surfaces with the RMS roughness over 3 nm. The surface roughness dramatically decreases with the increase of the growth pressure, and the layers show very flat surfaces with the RMS roughness under 1 nm at 300 Torr. Based on these results, we could obtain an InAlN layer with a flat surface morphology containing 19% of indium that is nearly lattice-matching to GaN. The layer structure of the InAlN test structure and its HR-XRD ω-2θ-scan result in (004) diffraction are shown in Figure 4-4.

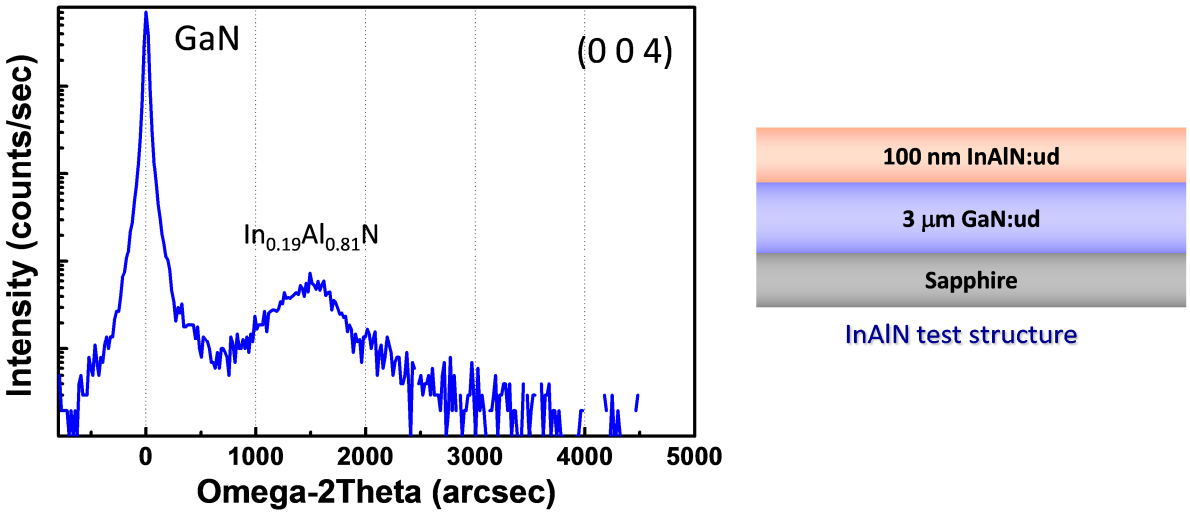

Figure 4-4. The structure of the InAlN test sample and its HR-XRD ω-2θ-scan result in (004) diffraction.

Under the assumption that the layer is fully strained, the indium composition of the layer calculated from the separation between the peak from the GaN layer and the InAlN layer is 19%. To confirm the strain status of the layer, we performed HR-XRD RSM in (105) diffraction, and the result is shown in Figure 4-5.

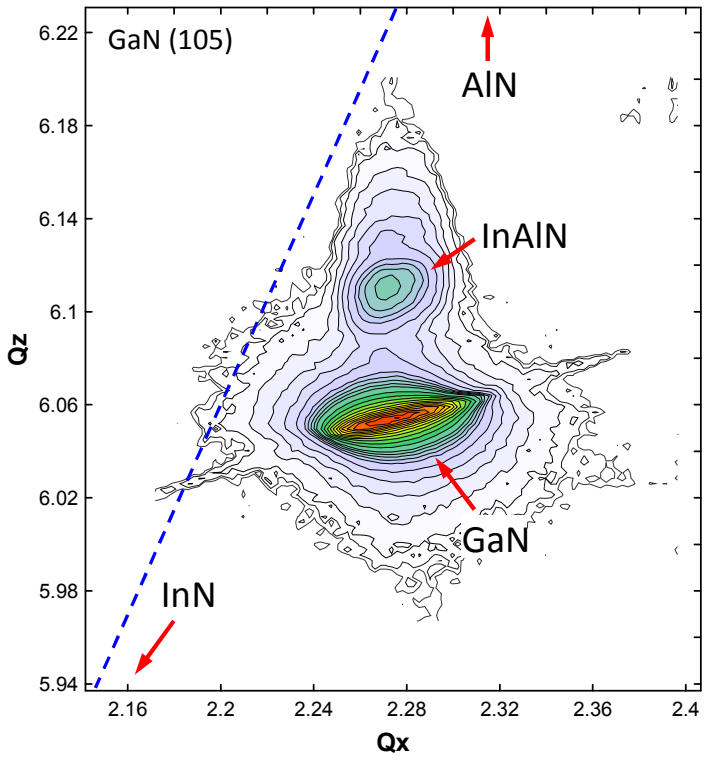

Figure 4-5. HR-XRD RSM observation result of the InAlN test sample in (105) diffraction.

In the reciprocal space plot shown in Figure 4-5, reciprocal points from the GaN layer and the InAlN layer have very close q_x coordinates. This means that those layers have very similar in-plane lattice constants and they are confirmed to be in the lattice-matched status. Therefore, the composition obtained from the HR-XRD ω-2θ-scan under the assumption that the layer is not relaxed is confirmed to be correct. The surface morphology of the $In_{0.19}Al_{0.81}N$ layer observed by AFM is shown in Figure 4-6. The sample has a flat surface with a well-developed step-flow morphology.

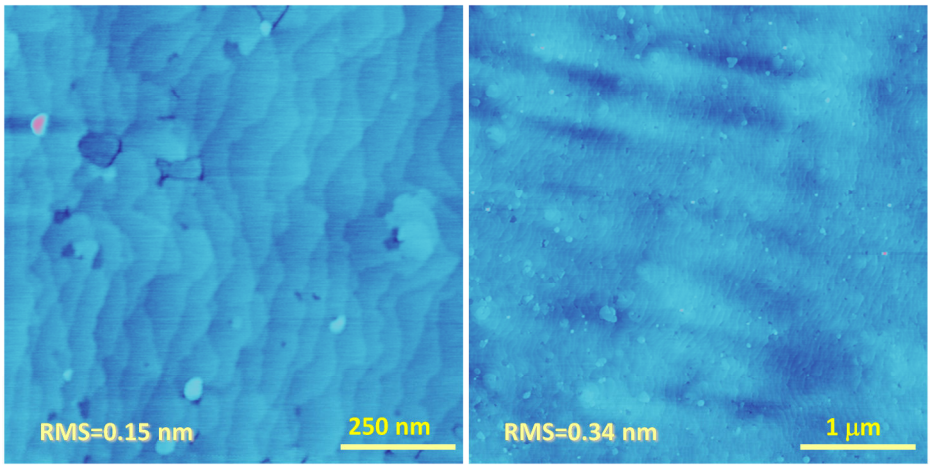

Figure 4-6. The surface morphology of the $In_{0.19}Al_{0.81}N$ test sample observed by AFM.

4.2 Band-Structure Calculation of the LEDs with an EBL

Before the growth of the actual LED structures, we performed band-structure calculations of the LEDs with different EBLs by using Sentaurus software for a theoretical comparison. The calculated band diagrams of the blue LED structures with $In_{0.19}Al_{0.81}N$ and $Al_{0.30}Ga_{0.70}N$ EBLs are shown in Figure 4-7. It is worthy of noting that the $Al_{0.30}Ga_{0.70}N$ EBL has more aluminum mole fraction than a *typical* EBL in the LED epitaxial structures, hence a better electron-confinement, while being accompanied by more material-related issues such as a higher T_g and a higher tensile strain than a typical AlGaN EBL.

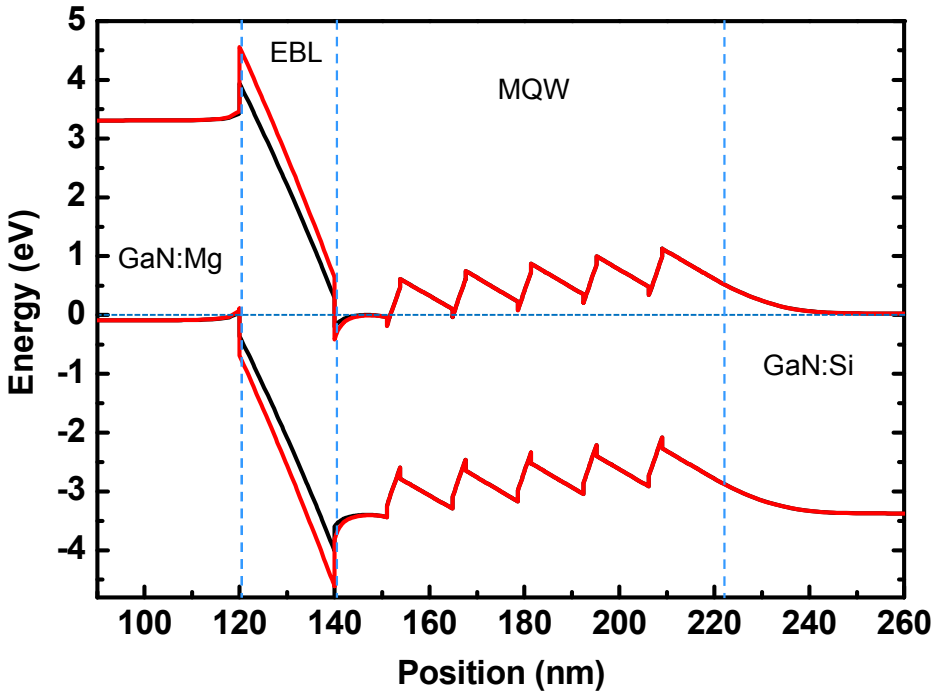

Figure 4-7. Calculated band structures of the blue LEDs with an $In_{0.19}Al_{0.81}N$ and an $Al_{0.30}Ga_{0.70}N$ EBLs.

The piezoelectric field within the $In_{0.19}Al_{0.81}N$ EBL layer is very small, because it is nearly lattice-matched to GaN and the layer strain is small. However, the difference in the spontaneous-polarization field induces a relatively high built-in potential field parallel to the [0001] direction. As a result, in combination with a large conduction-band offset, the insertion of an $In_{0.19}Al_{0.81}N$ EBL layer provides an excellent electron confinement in the conduction band of the active region, as shown in Figure 4-7. The conduction-band offset of the nearly lattice-matched $In_{0.19}Al_{0.81}N$ to GaN (1.14 eV), calculated from the interpolation between the values of AlN (1.75 eV) [67] and InN (1.68 eV) [68], is much higher than that of $Al_{0.3}Ga_{0.7}N$ (0.53 eV). In the conventional AlGaN EBLs, an increase of the aluminum mole fraction is the only way to enhance the confinement effect on electrons. However, it will also introduce a higher strain and a larger polarization field, and it is very difficult to incorporate an aluminum mole fraction higher than 30%. Therefore, the InAlN EBL is expected to provide a more effective electron confinement without detrimental effects due to a lattice mismatch and a high growth

temperature. In the band-structure diagram, the existence of a parasitic electron accumulation in the last QW barrier near the EBL and the potential barrier for the hole-transport at the *p*-GaN/*p*-InAlN EBL must also be noted. The parasitic electron accumulation, similar to that which forms the electron channel in the AlGaN/GaN heterostructure field-effect transistors, may potentially result in a decreased quantum-efficiency (more specifically, a reduced injection efficiency) and an increased threshold current in the LDs. The potential-barrier height, and the profile of the EBL and the last QW barrier also affect the distribution of holes in the MQW active region [69] that can result in the efficiency droop [70]. The parasitic electron accumulation and a non-uniform hole distribution among QWs can be mitigated by a tapered potential-barrier profile employing a compositional grading from the QW to the EBL [69] and/or a further improved magnesium doping of the EBL. Various techniques to improve the hole injection efficiency in the LED structures with InAlN EBLs and their results will be discussed in Chapter 5.

4.3 Growth and Fabrication of the LED Structures

By using previously developed growth conditions, the $In_{0.19}Al_{0.81}N$ layers were inserted into the standard blue LED structures as an EBL. The blue LED which does not include an EBL and the LED with an $Al_{0.2}Ga_{0.8}N$ EBL were also grown for the comparison purpose. All LEDs share a very similar epitaxial structure. They consist of a 3-μm-thick Si-doped *n*-type GaN layer with an electron concentration of $n\sim5\times10^{18}$ cm^{-3} (*n*-GaN:Si, 3 μm, $n\sim5\times10^{18}$ cm^{-3}), a five-period $In_{0.16}Ga_{0.84}N$/GaN (2.5/11 nm) multiple QW (MQW) active region, an $In_{0.19}Al_{0.81}N$:Mg or $Al_{0.2}Ga_{0.8}N$:Mg EBL (20 nm), a *p*-GaN:Mg (100 nm, $p\sim8\times10^{17}$ cm^{-3}) and a GaN:Mg^{++} (20 nm, [Mg]~1×10^{20} cm^{-3}). The schematic layer structure of the blue LED with an EBL is shown in Figure 4-8.

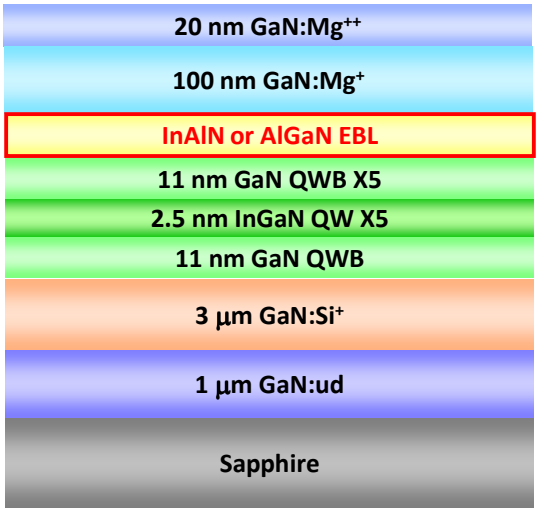

Figure 4-8. Schematic layer structure of the LED with an $In_{0.19}Al_{0.81}N$ or an $Al_{0.2}Ga_{0.8}N$ EBLs

The growth temperature of the QWs was set to 750 °C for the emission in blue region around 475 nm. The $In_{0.19}Al_{0.81}N$ EBL was grown at 845 °C and at a growth rate of 0.012 nm/sec for the optimized crystalline quality [71], while the $Al_{0.2}Ga_{0.8}N$ EBL was grown at 930 °C and at 0.065 nm/sec. The growth conditions of the active regions of all LEDs were maintained to be same. This ensures the same Auger recombination and hole-transport effects on the peak efficiency and efficiency droop except for minor influences of the different EBLs. The layer structures are also examined with HR-XRD. The HR-XRD ω-2θ-scan result on the LED with an $In_{0.19}Al_{0.81}N$ EBL in the symmetric (002) diffraction is shown in Figure 4-9.

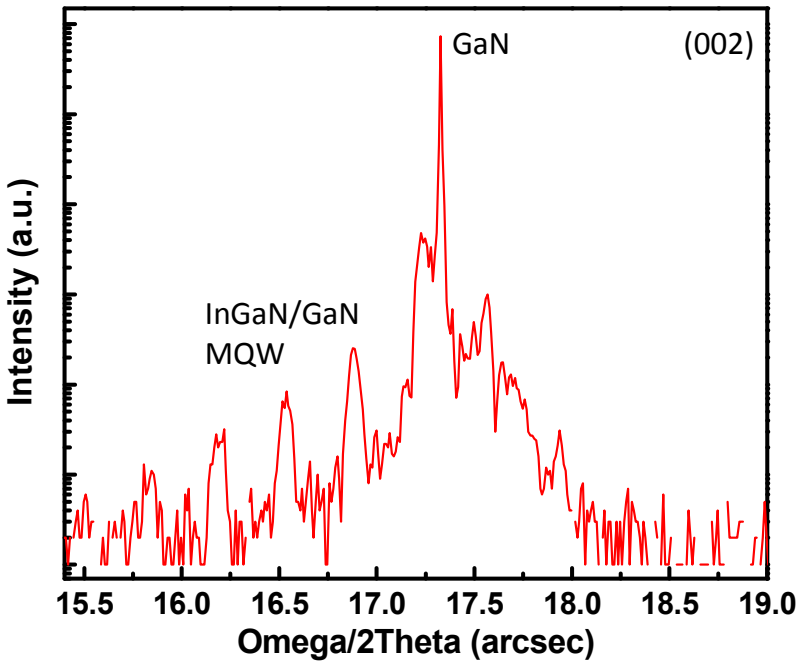

Figure 4-9. HR-XRD ω-2θ-scan result on the LED with an $In_{0.19}Al_{0.81}N$ EBL in the symmetric (002) diffraction.

The rocking curve shown in Figure 4-9 clearly shows the periodic satellite peaks which contain information on the composition and the thickness of the InGaN/GaN QWs and QBs. According to a HR-XRD simulation using Philips Epitaxy software, the thickness of the QWs and QBs are estimated to be 2.6 nm and 11 nm, respectively. Also, the peak from an $In_{0.19}Al_{0.81}N$ EBL is expected to appear at the right side of the GaN layer peak. But the peak from the $In_{0.19}Al_{0.81}N$ EBL is not clearly shown, because it is overlapped with satellite peaks from the InGaN/GaN MQW and the thickness of the EBL is thin.

The surface morphologies of as-grown LEDs with and without EBLs are shown in Figure 4-10. All samples show a flat surface morphology with the RMS roughness smaller than 0.4 nm, indicating that the insertion of an $In_{0.19}Al_{0.81}N$ or $Al_{0.2}Ga_{0.8}N$ layer did not cause a significant surface roughening or a *p*-layer crystalline-quality degradation. To observe the crystalline qualities more closely, high-resolution transmission electron microscopy (HR-TEM) was used for the LED structures. A bright-

field, cross-section HR-TEM image of the LED structure without an EBL on [11-20] zone axis is shown in Figure 4-11. The image shows that the QWs and QBs in the MQW region have uniform thicknesses with abrupt interfaces. The total thickness of the active region consisted with 5 pairs of QW/QB (five QWs and four QBs) is estimated as 56 nm. This thickness is consistent with the target thicknesses of QW (2.5 nm) and QB (11 nm).

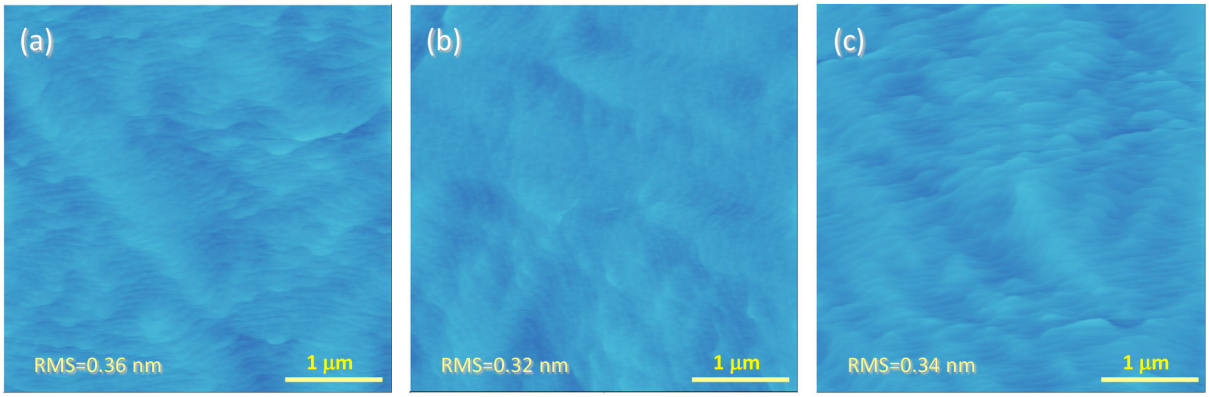

Figure 4-10. The surface morphologies of the LEDs (a) without an EBL, (b) with an $In_{0.19}Al_{0.81}N$ EBL, and (c) with an $Al_{0.2}Ga_{0.8}N$ EBL observed by AFM.

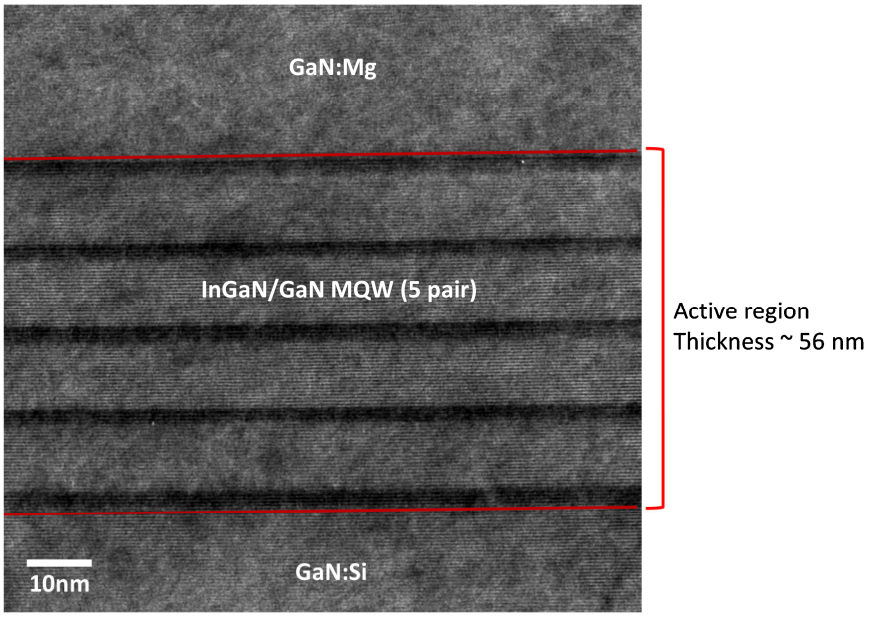

Figure 4-11. The bright-field, cross-section HR-TEM image of the blue LED without an EBL on [11-20] zone axis.

The bright-field, cross section HR-TEM images of the LED with an $In_{0.19}Al_{0.81}N$ EBL and the LED with an $Al_{0.2}Ga_{0.8}N$ EBL on [11-20] zone axis are shown in Figure 4-12. The $In_{0.19}Al_{0.81}N$ EBL shown in Figure 4.12 (a) looks brighter than other layers because of its higher aluminum composition. The interfaces between the $In_{0.19}Al_{0.81}N$ EBL and the GaN layers show a sharp transition and flat morphology. The thickness of the $In_{0.19}Al_{0.81}N$ EBL measured from the HR-TEM image is around 16-18 nm. The $Al_{0.2}Ga_{0.8}N$ EBL shown in Figure 4-12 (b) also looks brighter than the active region and the GaN layer, but its lower aluminum composition (target = 20% Al) makes it less bright than the $In_{0.19}Al_{0.81}N$ EBL. The thickness of the $Al_{0.2}Ga_{0.8}N$ EBL is estimated to be around 23 nm. Both $In_{0.19}Al_{0.81}N$ EBL and $Al_{0.2}Ga_{0.8}N$ EBL shows sharp interfaces between underlying and upper GaN layers with a flat interface morphology. Also, the thickness of the QW/QB of the active regions in the LEDs with the EBLs is very similar to that of the LED structures without an EBL.

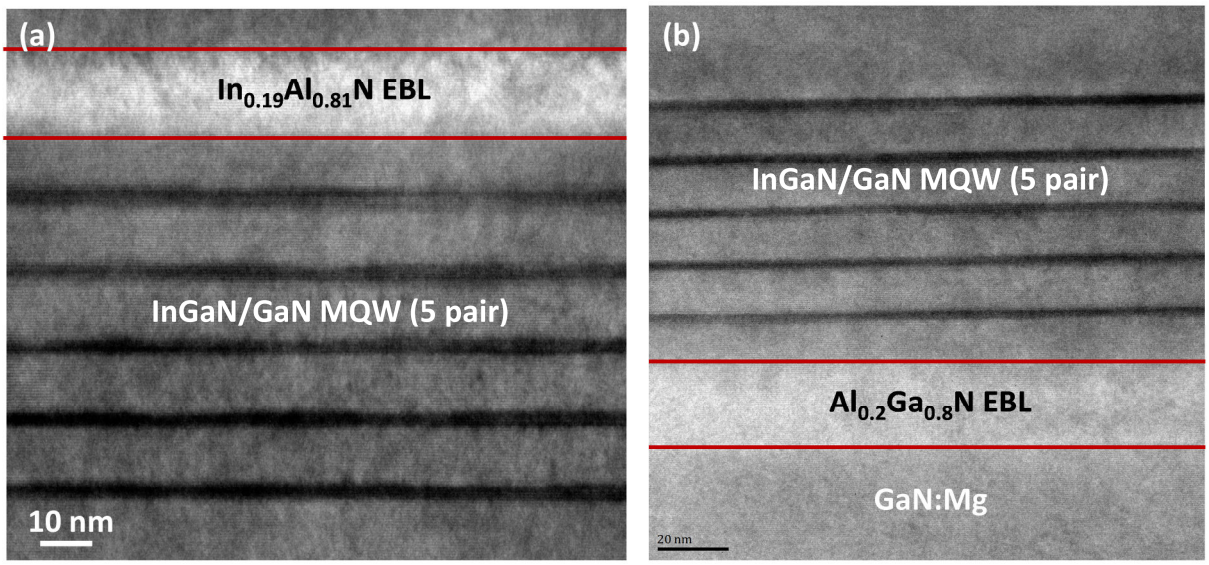

Figure 4-12. The bright-field, cross-section HR-TEM images of (a) the blue LED with an $In_{0.19}Al_{0.81}N$ EBL, and (b) the blue LED with an $Al_{0.2}Ga_{0.8}N$ EBL on the [11-20] zone axis.

These LED structures were fabricated into devices using a standard top-emitting chip process. The fabrication process consists with a mesa definition produced by an inductively-coupled plasma reactive ion etching, a Ti/Al/Ti/Au *n*-Ohmic contact metallization, and a transparent Ni_xO_{1-x}/Au *p*-Ohmic contact metallization by an electron-beam evaporation followed by a thermal annealing. An optical microscope image of a fabricated LED with the 350×350 μm^2 device area is shown in Figure 4-13.

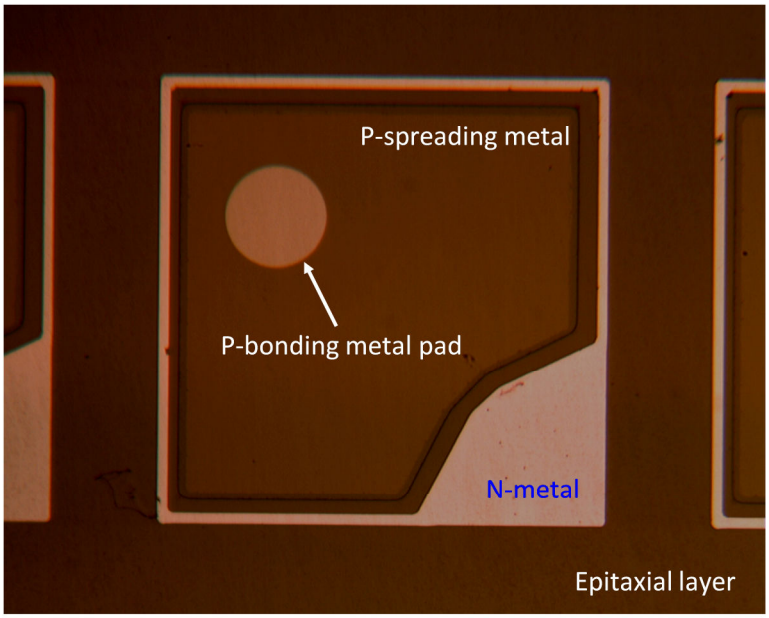

Figure 4-13. An optical microscope image of the fabricated blue LED with the device area of 350×350 μm^2.

4.4 Electrical Characterization of the Blue LEDs

The electrical characteristics of the fabricated blue LEDs with and without the EBLs were analyzed before the emission performances of the LEDs were measured. The electrical characteristics of the LED are deeply related with its overall performance. The quantum efficiency which can be enhanced by reducing the efficiency droop is determined only by the ratio between the injected current (or the number of the injected carriers) and the number of the photons generated by the radiative recombination processes, and the device operation voltage is not considered. However, the overall performance of the LED is evaluated by the light output generated by the unit amount of the electrical energy supplied, and the power consumption of the LED should be taken into account. One of the more important factors determining the voltage and the power consumption is the series resistance of the LED. The series resistance is defined as an additional resistance component which appears in series with the ideal-diode component in the equivalent circuit of an actual LED. The series resistance

can be represented as a sum of the resistances of the each layer, such as the *n*-type and the *p*-type regions and the MQW region. The insertion of an EBL into the LED structure may increase the series resistance and the device operation voltage, because (1) the thickness of the EBL adds an extra traveling distance for holes, and (2) lower magnesium-doping efficiency of the EBL with a high aluminum composition makes the EBL more resistive than the *p*-type GaN:Mg layer. Worse electrical properties of a LED including a higher operation voltage and a larger series resistance can degrade the overall performance of the LED. If a LED with an EBL achieved improved quantum efficiency at a cost of the increased device voltage, then the total power consumption of the LED is increased and most of the performance benefits brought by the enhanced quantum efficiency will be screened out. Therefore, the impact of the insertion of the EBLs on the electrical characteristics of the LED structures should be examined to evaluate the actual performance improvements of the LEDs. Because the blue LEDs with and without the EBLs share the same layer structure, the influences of the EBLs on the electrical properties can be easily isolated by comparing the measurement results.

The electrical properties of the *p*-type and *n*-type layers of the LEDs were measured by using TLM method to ensure the uniformity between the samples. The size of the metal contact pads is 200 μm by 50 μm, and the gaps between the metal pads are 10/20/40/70/110 μm for the *n*-type layers and 8/14/20/30/50 μm for the *p*-type layers. An Agilent Model 4156C semiconductor parameter analyzer connected to a PC controlled by Interactive Characterization Software's Metrics software was used to apply the voltage and measure the current flow between the two metal pads with different gaps. The current larger than 100 mA was not measured because of the current compliance of the 4156C. The current-voltage measurement results on the TLM patterns are shown in Figure 4-14.

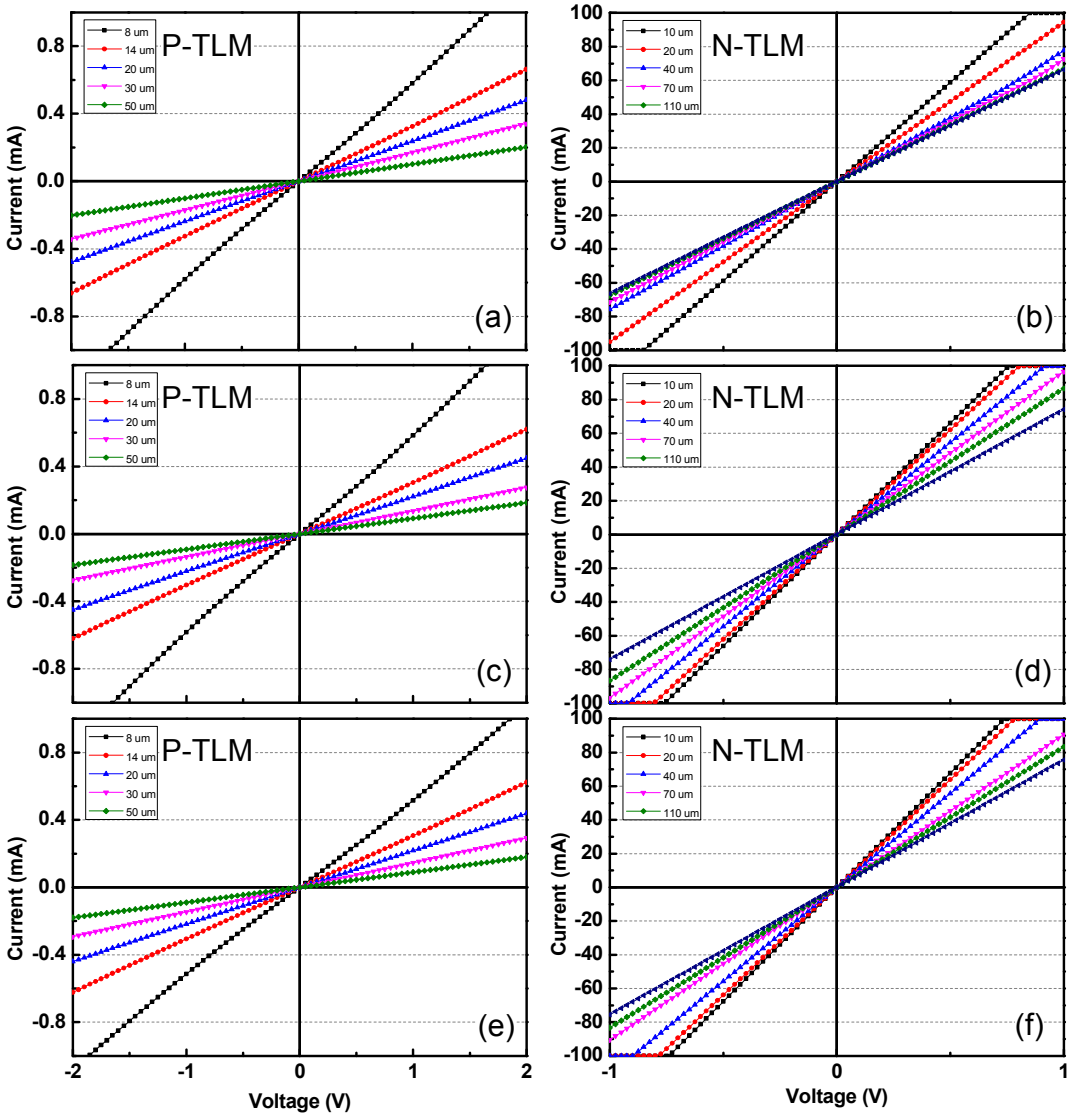

Figure 4-14. The TLM results on the *p*- and *n*-type layers of the blue LEDs. (a) and (b) the LEDs without an EBL, (c) and (d) the LEDs with an $In_{0.19}Al_{0.81}N$ EBL, and (e) and (f) the LEDs with an $Al_{0.2}Ga_{0.8}N$ EBL.

In the TLM results on the *n*-type layers, the measured current-voltage curves show a very good linear behavior, indicating that the contacts between the metal pads and the semiconductor layers have good Ohmic characteristics. The measurement results on the *p*-type layers also show a good linearity without a noticeable Schottky semiconductor-metal contact behavior. The total resistances of each gap calculated from the current-voltage curves were plotted along with the gaps and linear fitted to

obtain the specific contact resistances (r_c) and the sheet resistances (R_{sh}). The specific contact resistances and the sheet resistances calculated from the slopes and the intercepts of the linear fittings are listed in Table 4-1. The *R*-square values of the linear fittings are also listed with the results.

Table 4-1. The sheet resistances and the specific contact resistances of the LEDs without and with EBLs obtained from the TLM results.

Layer	Blue LED without an EBL			Blue LED with an $In_{0.19}Al_{0.81}N$ EBL			Blue LED with an $Al_{0.2}Ga_{0.8}N$ EBL		
	R_{sh} (Ω)	r_c (Ω-cm2)	R^2	R_{sh} (Ω)	r_c (Ω-cm2)	R^2	R_{sh} (Ω)	r_c (Ω-cm2)	R^2
n-layer	10.0	3.0E-4	0.999	9.2	5.5E-4	0.999	12.3	3.6E-4	0.999
p-layer	84.5K	2.0E-4	0.999	95.6K	9.3E-5	0.991	95.1K	1.1E-4	0.999

According to Table 4-1, the *n*-type layers of all LEDs have similar electrical properties. The sheet resistances of the *n*-type layers were around 10 Ω regardless of the insertion of the EBLs. Specific contact resistances between the metal contacts and the semiconductor layers were also uniform between the samples. The sheet resistances and the specific contact resistances of the *p*-type layers also shows very similar values with small differences between the samples, indicating that the *p*-doped region (excluding the EBL) of each LEDs have similar electrical properties. Therefore, any differences in the electrical properties which may be observed between the LED samples should be considered as the effect of the EBLs.

The current-voltage curves on the fabricated LEDs with a device area of 350 μm × 350 μm^2 were measured with an on-wafer probing system and shown in Figure 4-15 (a), (c), and (e). The voltage was supplied by the Agilent Model 4156C power supply and the current was measured up to 100 mA.

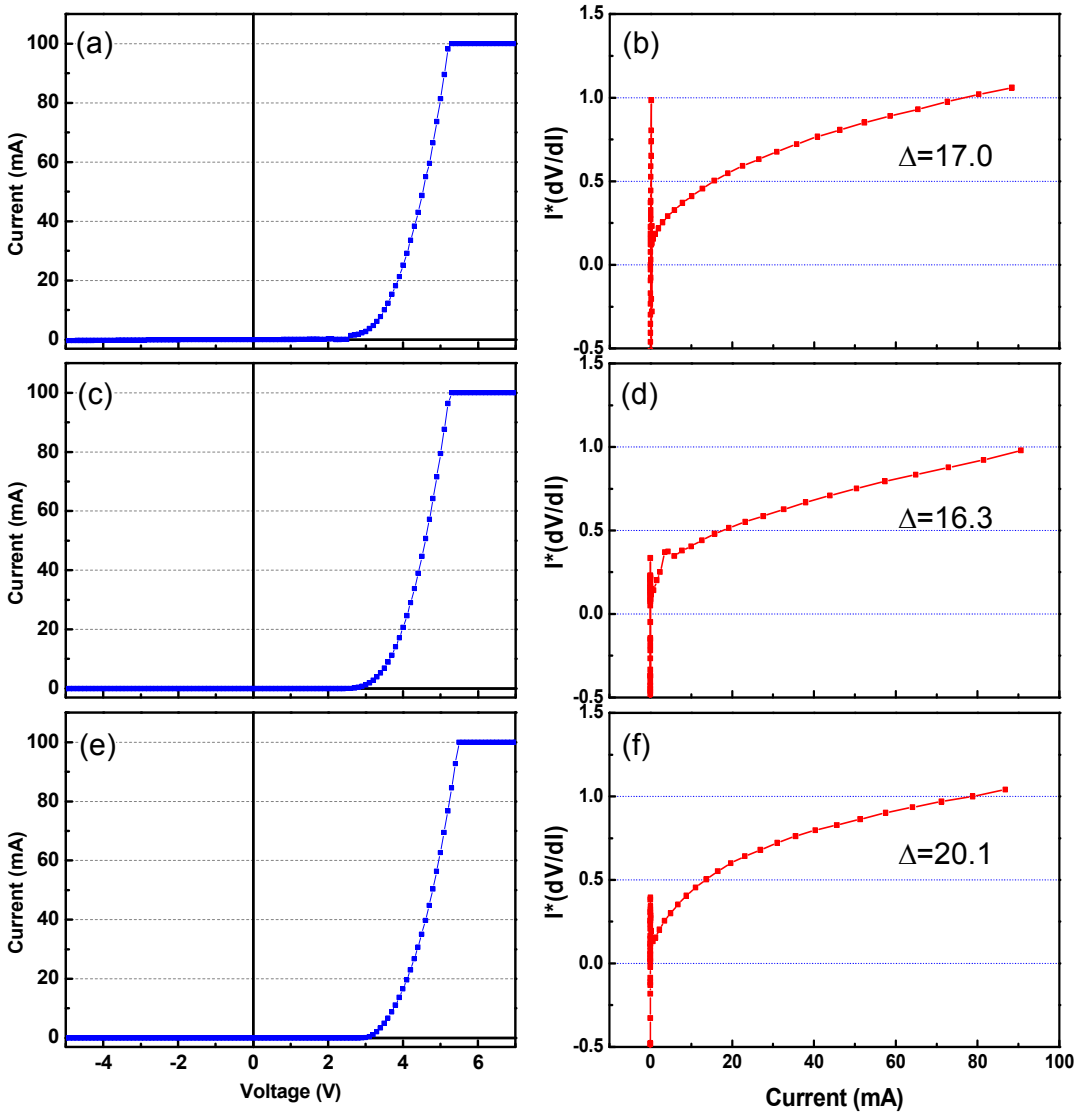

Figure 4-15. The current-voltage measurement results and series resistance plots on the blue LEDs. (a) and (b) the LEDs without an EBL, (c) and (d) the LEDs with an $In_{0.19}Al_{0.81}N$ EBL, and (e) and (f) the LEDs with an $Al_{0.2}Ga_{0.8}N$ EBL.

In Figure 4-15, all LEDs show similar current-voltage behaviors with small voltage or current differences. The voltages when the current reaches 20 mA were measured to be 3.9 V for the LED without an EBL and the LED with an $In_{0.19}Al_{0.81}N$ EBL, and 4.1 V for the LED with an $Al_{0.2}Ga_{0.8}N$ EBL. Also, the amount of the current flow at the applied voltage of 5V was observed to be 76 mA for the LED without an EBL, 80 mA for the LED with an $In_{0.19}Al_{0.81}N$ EBL, and 70 mA for the LED with

an $Al_{0.2}Ga_{0.8}N$ EBL. These results indicate that the insertion of the EBLs did not cause a significant extra voltage on the operation voltage of the LEDs. The observed voltage changes are limited to 5% of the forward voltage of the LED without an EBL. To obtain the extra resistance components caused by the EBLs, the series resistances of the LEDs were calculated from the current-voltage measurement results. The current and the voltage of a diode with a series resistance R_s are described by the following equation:

$$I = I_s\left(exp\left(\frac{q(V_s - IR_s)}{nkT}\right) - 1\right), \quad (4\text{-}1)$$

where I_s is the saturation current of the diode, I is the diode current, V_s is the diode voltage, n is the ideality factor, k is Boltzmann constant, and T is the temperature. Equation 4-1 shows the increase of the effective diode voltage by the extra voltage caused by the series resistance. Under the condition that V_s is much larger than kT/q, Equation 4-1 is transformed to a linear equation between I and $I*dV/dI$ through some of the arithmetic processes as follows:

$$I\frac{dV}{dI} = IR_s + C, \quad (4\text{-}2)$$

where C is a constant. The values of $I*dV/dI$ obtained from the current-voltage measurement results of the LEDs are plotted in Figure 4-15 (b), (d), and (f) along with the current I. The series resistances calculated from the slope of the each plot are also displayed. In these results shown in Figure 4-15, the series resistance of the LED with an $Al_{0.2}Ga_{0.8}N$ EBL is slightly higher than those of the LED without an EBL or the LED with an $In_{0.19}Al_{0.81}N$ EBL. The increased resistance may originate from the additional thickness of the EBL, the lower magnesium-doping efficiency of the $Al_{0.2}Ga_{0.8}N$ EBL which contains high aluminum composition, or the non-uniformity in the device-fabrication process.

However, relatively small thickness of the EBL (20 nm) compared to the total thickness of the *p*-doped region (140 nm) limits the additional resistance to less than 18% of the total series resistance. Therefore, the electrical properties of the LED without an EBL and the LEDs with the EBLs can be safely considered as comparable. However, during the measurements and comparisons of the electroluminescence and quantum efficiency of the LEDs, the differences in the voltage and the series resistance will be considered and compensated for more accurate analysis.

4.5 Device Electroluminescence Measurement Results

The electroluminescence spectra of the LEDs measured with an on-wafer probing on the 350×350 μm^2 devices under an injection current, I, ranging from 60 mA (corresponding to a current density of J~49 A/cm^2) to 420 mA (J~343 A/cm^2) are plotted in Figure 4-16. For the measurement, a Keithley Model 2430 current source was used to supply pulse-mode current with a duty cycle of 10% and a pulse length of 10 msec. at room temperature. The peak emission wavelengths of LEDs without an EBL, with an $Al_{0.2}Ga_{0.8}N$ EBL, and with an $In_{0.19}Al_{0.81}N$ EBL at I=60 mA were 475 nm, 476 nm, and 473 nm, respectively. Therefore, the peak emission wavelength did not change very much with the different EBL schemes. Also, the LED emission peak intensity of the spectra at a given injection current increases in the order of: the LEDs (1) without an EBL, (2) with an $Al_{0.2}Ga_{0.8}N$ EBL, and (3) with an $In_{0.19}Al_{0.91}N$ EBL. The light-emission characteristics of the LEDs were estimated by comparing the integrated intensity change with the increasing current, as shown in Figure 4-17.

The LED without an EBL shows an almost linear increase in the light output that is slightly higher than the LEDs with the EBLs in the low injection-current region of I<40 mA. However, at higher injection currents, the *L-I* curve of the LED without an EBL shows a distinct sub-linear behavior and a tendency to saturate at I~75 mA. At even higher currents of I>360 mA, an increase in the injection current hardly contributes to the increase of the light output, and only a small portion of

the injected carriers result in the radiative recombination. The LED with an $Al_{0.2}Ga_{0.8}N$ EBL shows lower light outputs than the LED without an EBL for low and medium injection currents (I<120 mA). However, with an increase of the injection current, the light output rapidly increases and surpasses the LED without an EBL at I~140 mA. Moreover, higher slope of the curve is maintained at higher currents with a significantly reduced efficiency droop, showing ~25% higher light output at I=360 mA and ~40% higher at I=440 mA than the LED without an EBL. The light output of the LED with an $In_{0.19}Al_{0.81}N$ EBL is slightly higher than that of the LED without an EBL at I=50 mA, but it ramps up significantly with the increasing injection current. As a result, it is ~110% brighter than the LED without an EBL and 40% brighter than the LED with an $Al_{0.2}Ga_{0.8}N$ EBL at I=440 mA. The light output is significantly enhanced when either an $Al_{0.2}Ga_{0.8}N$ or $In_{0.19}Al_{0.81}N$ layer is inserted as an EBL, possibly because of their improved electron-blocking effect in the high injection-current regime. Also, higher light output of the LED with an $In_{0.19}Al_{0.81}N$ EBL indicates a superior electron confinement with respect to the $Al_{0.2}Ga_{0.8}N$ EBL case.

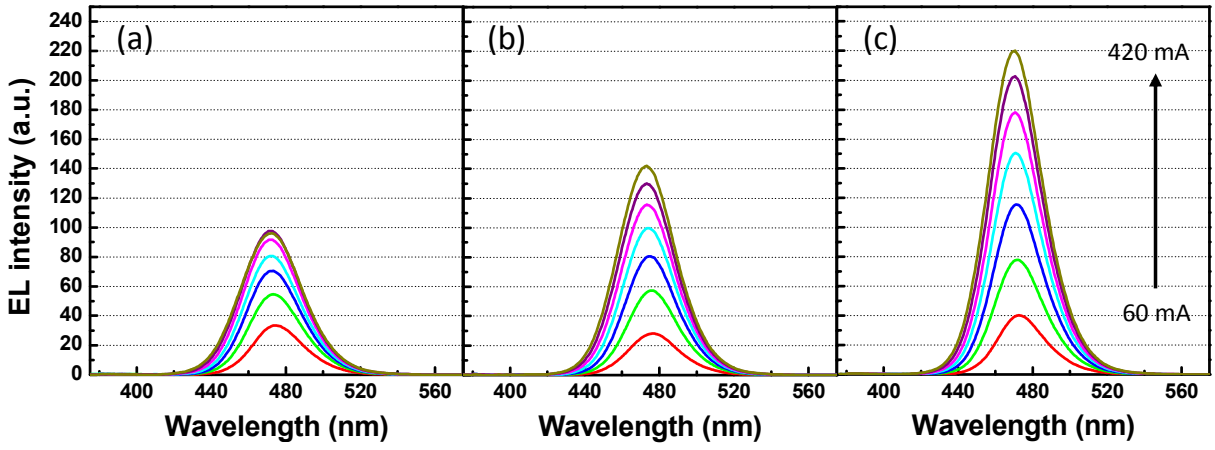

Figure 4-16. Electroluminescence spectra of the LEDs (a) without an EBL, (b) with an $Al_{0.2}Ga_{0.8}N$ EBL, and (c) with an $In_{0.19}Al_{0.81}N$ EBL, with the pulse-mode injection current up to 420 mA.

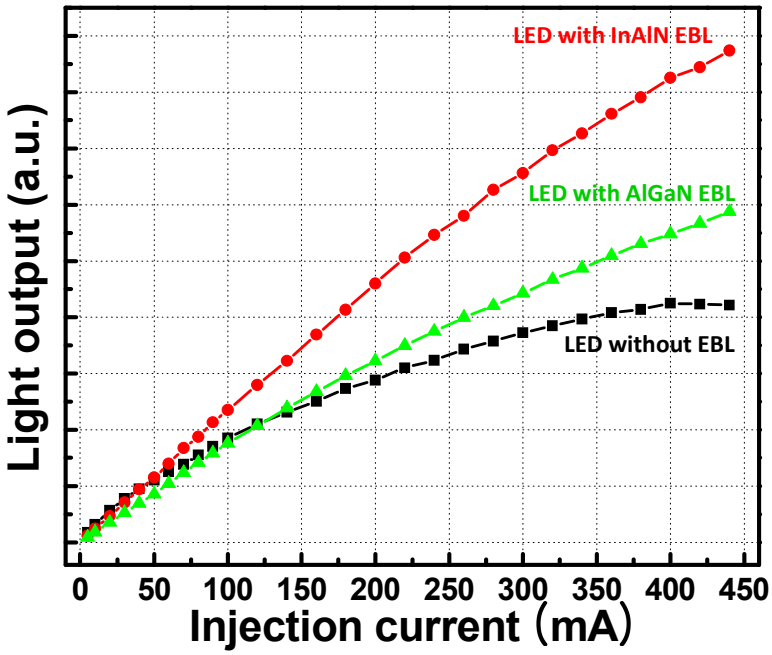

Figure 4-17. Light output versus current (*L-I*) characteristics of the LEDs without an EBL, with an $Al_{0.2}Ga_{0.8}N$ EBL, and with an $In_{0.19}Al_{0.81}N$ EBL.

To clarify the effect of the various EBLs on the efficiency droop, the quantum efficiency of the LEDs is calculated and plotted versus the current density in Figure 4-18. The quantum efficiency is obtained by dividing the integrated EL intensity by the injection current. After a rapid increase at very low injection-current densities, all the LEDs show a monotonic efficiency drop with the increasing current. The efficiency droop can be defined by the ratio of drop of the efficiency from the peak value.

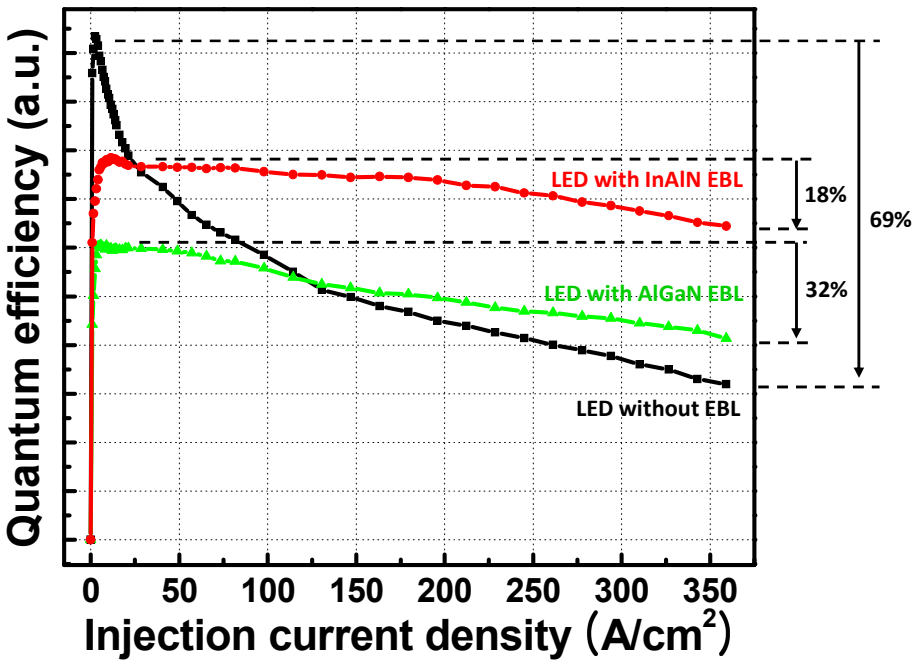

Figure 4-18. Quantum efficiency versus injection-current density for the LEDs without an EBL, with an $Al_{0.2}Ga_{0.8}N$ EBL, and with an $In_{0.19}Al_{0.81}N$ EBL.

In Figure 4-18, the LED without an EBL shows a sharp peak efficiency at J=3 A/cm^2, while the LEDs with an $Al_{0.2}Ga_{0.8}N$ EBL and an $In_{0.19}Al_{0.81}N$ EBL show peak efficiencies at J=6 A/cm^2 and 11.5 A/cm^2, respectively. Note that the peak efficiency of the LED without an EBL is higher than other LEDs with EBLs and also occurs at a lower current density. The insertion of an EBL creates barriers not only in the conduction band, but also in the valence band that may act as a hole-blocking barrier. At low current densities, this barrier may limit the hole-transport into the active region and may result in a non-uniform hole distribution [69] leading to lower quantum efficiencies for the LEDs with an EBL than for the LED without an EBL. Beyond the peak efficiency, the LED without an EBL shows a rapid efficiency drop with increasing injection-current density suggesting a severe carrier loss by carrier spill-over. The quantum efficiency of the LED without an EBL at J=360 A/cm^2 is only one-third of its peak-efficiency value showing an efficiency droop of ~69%. On the other hand, the LED with an $Al_{0.2}Ga_{0.8}N$ EBL shows the lowest peak efficiency at low current densities, but the droop of

the efficiency with an increase of the current density is much smaller than that of the LED without an EBL. As a result, its quantum efficiency exceeds that of the LED without an EBL at the current density higher than J=130 A/cm^2, and shows a ~30% higher value at J=360 A/cm^2. The efficiency droop is also improved with only a ~32% efficiency drop at J=360 A/cm^2 with respect to the peak value. The peak efficiency of the LED with an $In_{0.19}Al_{0.81}N$ EBL is located between those of the LED with an $Al_{0.2}Ga_{0.8}N$ EBL and the LED without an EBL, and because of its smallest efficiency-drop rate, it shows the highest absolute efficiency and the lowest efficiency droop at high current densities. The efficiency droop at J=360 A/cm^2 is estimated to be ~18% compared to its peak value. Thus, the $In_{0.19}Al_{0.81}N$ EBL has demonstrated to provide a better electron-blocking effect than the $Al_{0.2}Ga_{0.8}N$ EBL, and the LED with an $In_{0.19}Al_{0.81}N$ EBL shows significantly improved emission intensities and substantially mitigated efficiency droop in the visible wavelength region than the LED with a conventional $Al_{0.2}Ga_{0.8}N$ EBL. However, although the efficiency droop is significantly improved by the insertion of the $In_{0.19}Al_{0.81}N$ EBL through minimizing the carrier spill-over, the droop is not completely suppressed. This may suggest that other mechanisms such as Auger recombination or limited hole-transport may also have some influence in the efficiency droop.

CHAPTER 5 THE HOLE-BLOCKING EFFECT OF THE InAlN ELECTRON-BLOCKING LAYER IN THE LIGHT-EMITTING DIODES

5.1 Introduction

As shown in Chapter 4, an $In_{0.19}Al_{0.81}N$ EBL is confirmed to provide higher efficiency droop performance, because it is more effective in confining electrons and minimizing the carrier spill-over than the conventional $Al_{0.2}Ga_{0.8}N$ EBL. However, the efficiency droop of the LED is not completely suppressed by employing an $In_{0.19}Al_{0.81}N$ EBL. In Figure 4-15, the quantum efficiency of the LED with an $In_{0.19}Al_{0.81}N$ EBL still shows the decrease of the emission efficiency with the increasing injection current. As pointed out in Chapter 4.5, this may suggest the existence of other efficiency-droop mechanisms that can be suppressed by additional structural improvements.

The main strategy in the employment of the EBL is the suppression of the electron spill-over by creating a high electron-confinement barrier through the insertion of the wide-bandgap materials. Therefore, an $In_{0.19}Al_{0.81}N$ EBL with wider bandgap energy has an advantage over an $Al_{0.2}Ga_{0.8}N$ EBL in terms of the electron-confinement effect. However, it is clear that a wider-bandgap material also contributes to a higher hole-blocking barrier that may prevent the efficient injection of holes into the active region. The valence-band offset of the $In_{0.19}Al_{0.81}N$ layer on a GaN layer is calculated to be 0.40 eV under at equilibrium. This value is much larger than that of the conventional $Al_{0.2}Ga_{0.8}N$ EBL (0.11 eV), and the large valence-band offset creates a large hole-blocking barrier with a formation of a sharp potential spike. Although the performance enhancement from the electron-confinement effect of the EBL seems to override the impact of the hole-blocking effect on the light output, an improved hole-injection efficiency will lead to an additional increase of the LED performance. Moreover, the limited hole injection is claimed as one of the major origins of the efficiency droop by many reports [58,59]. Therefore, identifying the hole-blocking effect caused by the $In_{0.19}Al_{0.81}N$ EBL is very important in suppressing the efficiency droop of the LED.

5.2 Hole-Blocking Effect of the InAlN EBL

The hole-blocking effect of the $In_{0.19}Al_{0.81}N$ EBL is predicted by tracing the change of the electronic band structure of the LED. The band structure diagram of the blue LED structures with $In_{0.19}Al_{0.81}N$ EBLs nearly lattice-matched to GaN is calculated under the equilibrium condition by Sentaurus and shown in Figure 5-1. The thickness of the *p*-type GaN:Mg layers were set to around 200 nm, and the exact thickness of the *p*-type layer varies with the thicknesses of the EBLs to make the total *p*-type layer thickness (the thickness of the EBL and the GaN:Mg layer) to be 220 nm. The total thickness of the *p*-type layers is determined to maximize the light-extraction efficiency from the top surface of the LED device at the blue emission wavelength region. The detail of the *p*-layer design will be discussed later.

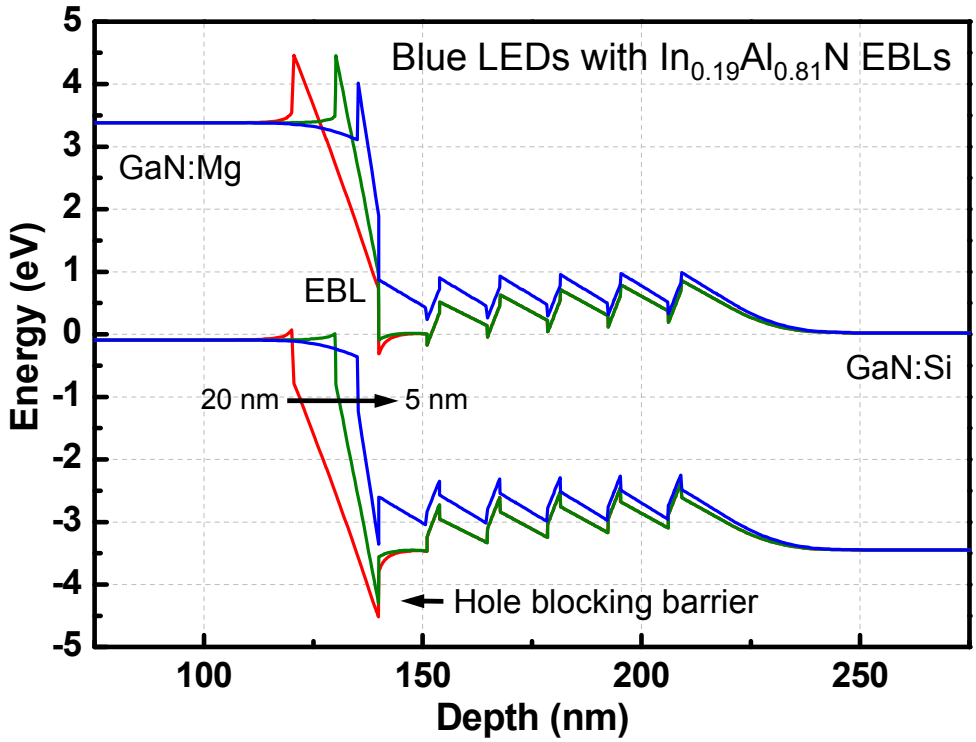

Figure 5-1. Electronic band diagram of the blue LED epitaxial structures with $In_{0.19}Al_{0.81}N$ EBLs with thicknesses of 5, 10, and 20 nm.

In Figure 5-1, a high barrier for hole transport is observed in the valence band at the interface between the $In_{0.19}Al_{0.81}N$ EBL and the active region. This hole barrier will cause a reduced hole-injection efficiency into the active region, and the hole deficiency leads to a lower emission performance of the LED. However, the impact of the hole blocking caused by the EBL on the performance of the LED cannot be separated and identified easily. An EBL with a high hole-blocking effect may also have a high electron-confinement effect that enhances the light output of the LED, and the overall performance of the LED is determined by both the hole-blocking effect and the electron-confinement effect. Therefore, for a quantitative evaluation of the impact of the hole blocking, a series of the LED structures with different amount of the hole-blocking and electron-confinement effect is needed to be analyzed with a proper model.

One parameter that controls the amount of the hole-blocking effect of the $In_{0.19}Al_{0.81}N$ EBL is the thickness of the EBL. In Figure 5-1, the height of the potential barrier induced by the $In_{0.19}Al_{0.81}N$ EBL in the valence band decreases with the reduction of the EBL thickness from 20 nm to 5 nm. In addition, the control of the hole-blocking effect by adjusting the EBL thickness has several advantages. The alloy composition of the $In_{0.19}Al_{0.81}N$ EBL is fixed, and the strain status of the EBL is maintained to be same without inducing any extra polarization field and band bending. Also, the magnesium doping efficiency that depends highly on the aluminum composition of the layer will remain unchanged, ensuring the electrical properties of the EBL region and the series resistance of the LEDs to be similar each other. Therefore, the strategy of changing the EBL thickness to control the hole-blocking effect can eliminate extra factors that may introduce artifacts in the analysis process.

For a quantitative analysis on the hole-blocking and electron-confinement effect of the EBL, we proposed and applied a quantum-efficiency model on the measurement results of the LEDs with different EBL thickness. Our model uses major recombination rate equations to describe the quantum efficiency of a LED analytically without depending on a computational method. The advantage of the analytical model over a computational method is that the model helps understanding the underlying mechanism between the carrier densities and the emission performance of the LED more clearly and directly than the computational method. The details on the analysis method will be discussed in Chapter 5.5.

5.3 Growth and Fabrication of the LED Structures with Different EBL Thickness

To evaluate the effect of the hole blocking and the electron confinement on the performance of the LED, blue LED structures that contain the EBLs with different thickness were grown. The structure of the LEDs is maintained to be very similar, consisting of a 3-μm-thick Si-doped *n*-type GaN layer (*n*-GaN:Si, 3 μm, n~5×10^{18} cm^{-3}), a five-period $In_{0.15}Ga_{0.85}N$/GaN (2.5/11 nm) multiple quantum-well (MQW) active region, a *p*-$In_{0.18}Al_{0.82}N$:Mg EBL, a *p*-GaN:Mg (p~8×10^{17} cm^{-3}), and a *p*-

GaN:Mg^{++} (20 nm, [Mg]~1×10^{20} cm^{-3}) contact layer. The thickness of the $In_{0.19}Al_{0.81}N$ EBL was changed from 5 to 20 nm, and a LED structure without an EBL was also grown for a comparison. The total layer thickness above the active region was maintained to be 240 nm by changing the thickness of the *p*-GaN:Mg layer to ensure the same light-extraction efficiency for different LED structures[72]. The schematic layer structure of the blue LED with different EBL thickness is shown in Figure 5-2.

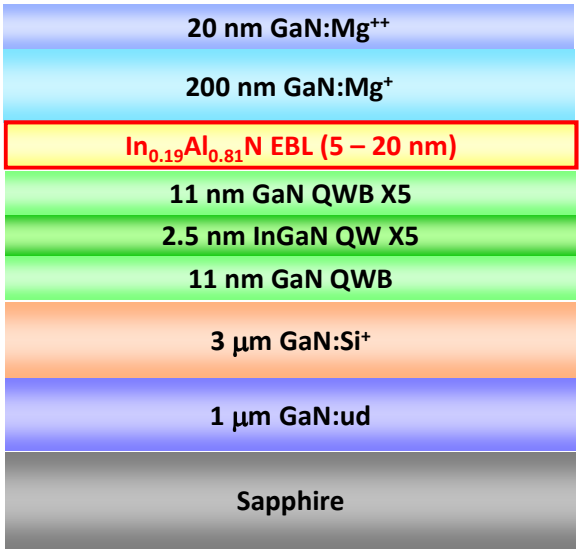

Figure 5-2. Schematic structure of a blue LED with an $In_{0.19}Al_{0.81}N$ EBL with different thickness.

The surface morphologies of as-grown LEDs with different EBL thickness are observed by AFM and shown in Figure 5-3. All samples show a good surface morphology with small RMS roughness below 0.5 nm. The insertion of the EBL did not cause any significant roughening on the sample surface regardless of the thickness change. The lattice-matching capability of the $In_{0.19}Al_{0.81}N$ EBL contributed to the flat surface morphology of the structure.

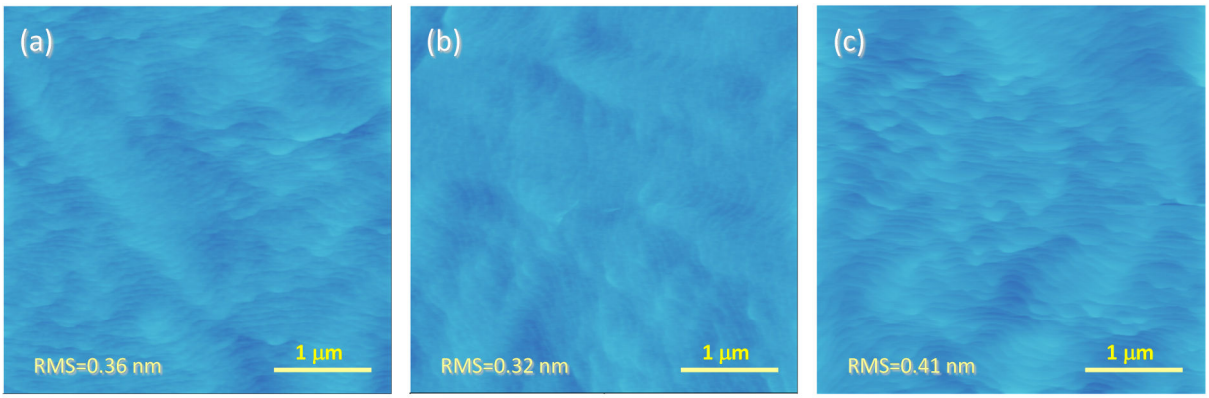

Figure 5-3. The surface morphology of the blue LEDs (a) without an EBL, (b) with a 20 nm $In_{0.19}Al_{0.81}N$ EBL, and (c) with a 10 nm $In_{0.19}Al_{0.81}N$ EBL.

These LED structures were fabricated into 350×350 μm^2 devices using a similar top-emitting chip process described in Chapter 4.3.

5.4 Device Characterization

The electrical characterization was performed on the fabricated LEDs to examine a possible discrepancy in the electrical properties caused by the insertion of different EBLs. The sheet resistance and the specific contact resistance of the *p*-type and *n*-type layers of the LEDs were measured by TLM. The standard TLM pattern is consisted with metal pads of 200 µm by 50 µm with gaps of 10/20/40/70/110 µm for the *n*-type layers and 8/14/20/30/50 µm for the *p*-type layers. An Agilent Model 4156C semiconductor parameter analyzer was used to apply the voltage and measure the current flow between the two metal pads with different gaps. The specific contact resistances and the sheet resistances of the *p*-type and *n*-type layers of the LED structures are calculated from the current-voltage relationship in the TLM measurements and listed in Table 5-1 with the R-square values of the linear fitting.

Table 5-1. The sheet resistances and the specific contact resistances of the *p*-type and *n*-type layers of the LEDs without an EBL and with $In_{0.19}Al_{0.81}N$ EBLs with different thicknesses obtained from the TLM results.

EBL thickness	None		20 nm		15 nm	
	R_{sh} (Ω/sq)	r_c (Ω-cm^2)	R_{sh} (Ω/sq)	r_c (Ω-cm^2)	R_{sh} (Ω/sq)	r_c (Ω-cm^2)
n-layer	5.5	1.0E-3	5.6	9.9E-4	5.9	8.6E-4
p-layer	38.4K	2.0E-4	41.2K	2.3E-4	43.7K	1.1E-4

EBL thickness	10 nm		5 nm	
	R_{sh} (Ω/sq)	r_c (Ω-cm^2)	R_{sh} (Ω/sq)	r_c (Ω-cm2)
n-layer	5.4	1.4E-3	5.1	1.4E-3
p-layer	38.9K	7.9E-4	43.8K	9.3E-5

According to Table 5-1, the *n*-type layer and the *p*-dope regions of all LEDs, including the LED structure without an EBL, have similar electrical properties. The insertion and the different thickness of the $In_{0.19}Al_{0.81}N$ EBLs may increase the sheet resistance of the *p*-doped region. The magnesium doping efficiency of the InAlN is lower than for GaN:Mg, and therefore it may have higher sheet resistance. Also, the doping profile may be changed with the "slow doping" effect of magnesium and different thickness of the EBLs (thus different growth time before the start of the growth of the GaN:Mg layers). However, the measurement results indicate that the insertion of the $In_{0.19}Al_{0.81}N$ EBLs with different thickness did not cause any significant change in the properties of the *p*-doped region. The current-voltage curves of the fabricated LEDs with a device area of 350 μm × 350 μm^2 were measured by an on-wafer probing and shown in Figure 5-4.

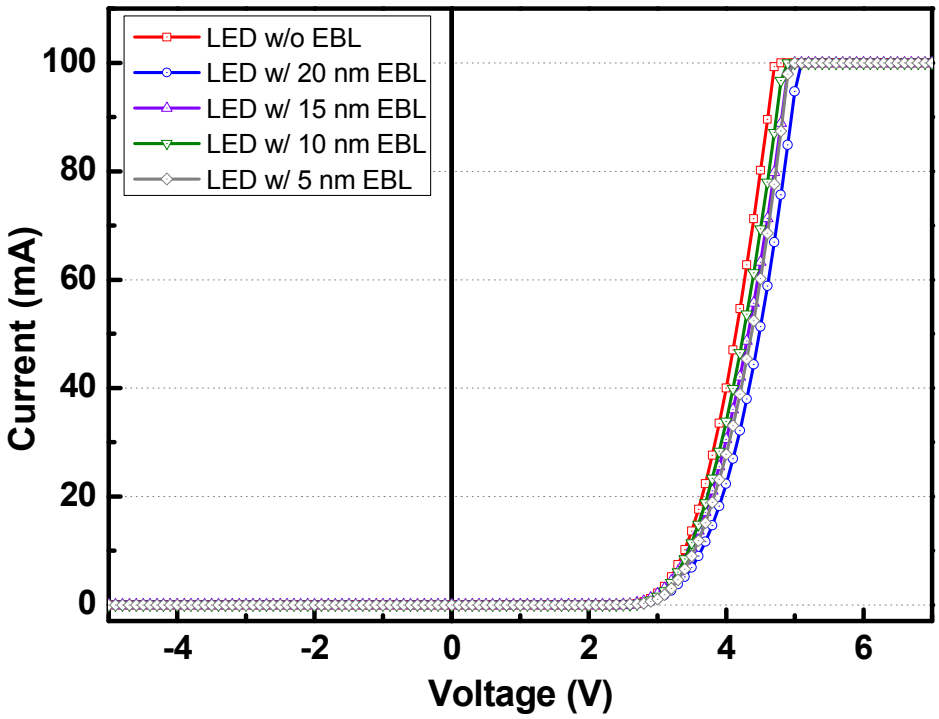

Figure 5-4. Current-voltage measurement results of the LEDs without an EBL and with $In_{0.19}Al_{0.81}N$ EBLs with different thickness from 5 nm to 20 nm.

In Figure 5-4, all LEDs show similar current-voltage behaviors with small voltage or current differences. The forward voltages at the injection current of 20 mA were measured to be 3.7 V for the LED without an EBL, and 3.7 to 3.9 V for all the LEDs with $In_{0.19}Al_{0.81}N$ EBLs regardless of their thickness. Also, all LEDs could flow more than 100 mA of current flow under the bias of 5V (the current could not be measured because of the current compliance of 4156C). These results indicate that the insertion of the $In_{0.19}Al_{0.81}N$ EBLs did not cause a significant extra voltage on the operation voltage of the LEDs. The observed voltage changes are limited to within 5% of the forward voltage of the LED without an EBL. Therefore, the electrical properties of the LED without an EBL and the LEDs with EBLs can be safely considered as comparable.

The electroluminescence spectra of the LEDs were measured with an on-wafer probing on the 350×350 μm^2 devices under an injection current ranging from 60 mA (corresponding to a current

density of J~49 A/cm^2) to 420 mA (J~343 A/cm^2). The pulse-mode current with a duty cycle of 10% and a pulse length of 10 msec. was supplied to the devices at room temperature during the measurement. The peak emission wavelengths of the LEDs appear at a very similar position of around 475 nm (data not shown). The light-emission characteristics of the LEDs were estimated by comparing the integrated EL intensity with the increasing injection current up to 460 mA, as shown in Figure 5-5.

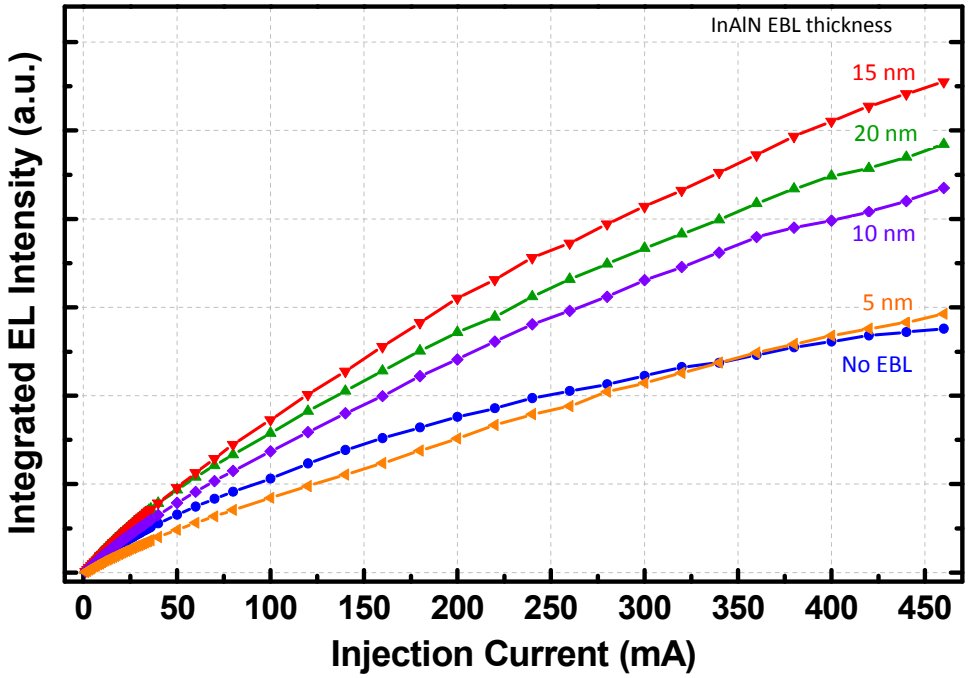

Figure 5-5. Integrated EL intensity vs. injection current density of the LEDs with $In_{0.19}Al_{0.81}N$ EBLs with various thicknesses.

In Figure 5-5, the LED without an EBL shows rather low integrated EL intensity compared to other LEDs with the EBLs. The LEDs with the $In_{0.19}Al_{0.81}N$ EBLs show much higher integrated EL intensity with a less saturation behavior at the high injection current region, confirming the electron-confinement effect and the low carrier spill-over of the $In_{0.19}Al_{0.81}N$ EBL that is observed in Chapter 4. The LED with a 15 nm $In_{0.19}Al_{0.81}N$ EBL shows the highest EL intensity, followed by the LEDs with a

20 nm EBL and with a 10 nm EBL. On the other hand, the LED with a 5 nm $In_{0.19}Al_{0.81}N$ EBL shows lower integrated EL intensity than the LED without an EBL at low current region. However, the LED with a 5 nm EBL has a smaller saturation behavior, and it surpasses the LED without an EBL at the high current region (> 350 mA). To observe the effect of the EBL thickness on the luminous performance of the LEDs more closely, the quantum efficiency of the LEDs are plotted with the injection current density in Figure 5-6.

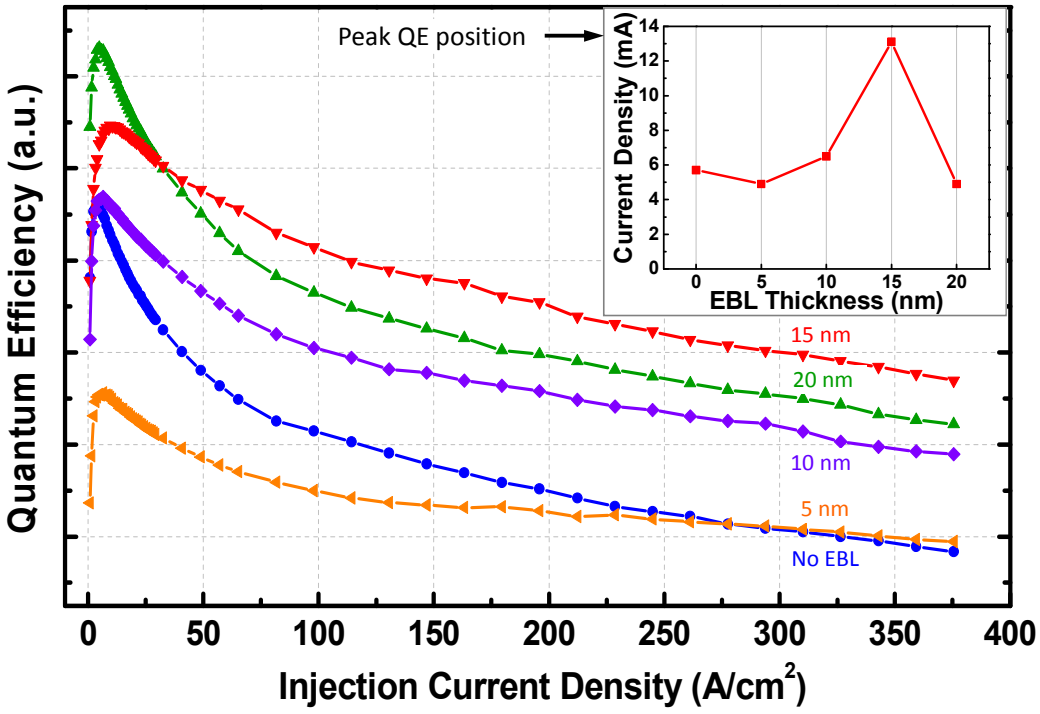

Figure 5-6. Quantum efficiency vs. injection current density of the LEDs with $In_{0.19}Al_{0.81}N$ EBLs with various thicknesses. Inset shows the injection current density at the peak quantum efficiency appears in each LED structure.

In Figure 5-6, all the LEDs show a typical quantum-efficiency behavior with an increasing injection current. The quantum efficiency increases with the current density under low injection conditions and then decreases under high injection conditions. However, several things need to be noted: First, the LED with a 5 nm EBL shows lower quantum efficiency than the LED without an

EBL except for the high current-density region. Also, the LED with a 20 nm EBL shows lower efficiency under high current injection than the LED with a 15 nm EBL. If only the electron-blocking effect is taken into account, these results, especially for the second observation, cannot be easily explained, because the insertion of the EBL or the increase of its thickness was supposed to suppress the carrier spill-over. In addition, the current density where the peak quantum efficiency appears has a clear trend with the EBL thickness, as shown in the inset of Figure 5-6. The peak quantum efficiency tends to appear at higher current density with a thicker EBL. However, the peak quantum efficiency of the LED with a 20 nm EBL does not follow this tendency, and it appears at a lower current density. The "peak" in the quantum efficiency was reported to occur at a relatively low current density dominated by the non-radiative recombination processes, especially the defect-related Shockley-Read-Hall (SRH) recombination, because other higher-order recombination processes are significant at higher current density[73]. However, since our LED structures share the same growth condition and crystalline quality in the GaN buffer and MQW active region, the radiative and non-radiative recombination parameters are expected to be same. Also, it was observed that the position of the peak efficiency is closely related with the carrier spill-over and the hole-injection efficiency[74,75,76]. The electrical properties of the *n*-type layers and the *p*-doped regions of the LEDs are shown to be very similar each other in the TLM measurement. Therefore, different carrier dynamics induced by the different $In_{0.19}Al_{0.81}N$ EBL structure is considered to be a more probable origin of the different peak-efficiency positions.

5.5 Modeling of the Quantum Efficiency

For a quantitative modeling of the quantum-efficiency behavior of the LEDs, we extended the model, well-known as the "ABC model", to include the carrier spill-over effect and the hole-blocking effect[77,78]. The "ABC model" assumes that the number of the carriers consumed via recombination processes is identical to the number of the carriers supplied by the current injection. When the

recombination region is much thinner than the diffusion length of the carriers inside a material structure, the recombination processes under the steady state are mainly consisted with Shockley-Read-Hall (SRH) non-radiative recombination, radiative recombination, and Auger non-radiative recombination. The rate of the carrier recombination in each process is described by the recombination probability and the density of the carrier. A typical expression of the "ABC model" is as follows:

$$An + Bn^2 + Cn^3 = J/qd \ , \qquad (5\text{-}1)$$

where n is the excess electron density, q is the electron charge, d is the thickness of the recombination region (active layer in case of a LED structure), and J is the injection-current density. The probability of the SRH, radiative, and Auger recombination processes are included in the equation as parameters of A, B, and C. When there are no other paths of the carrier loss, the representation of the internal quantum efficiency of the structure is very straightforward, as follows:

$$\eta_{int} = \frac{\tau_{eff}}{\tau_r} = Bn^2/(An + Bn^2 + Cn^3) \ . \qquad (5\text{-}2)$$

The values of A and B can be deduced from a trap density (N_t), a capture cross-section (σ), and a thermal velocity (ν_{th}) of the target material [79]. Assuming $N_t = 10^{16}$ cm^{-3}, $\sigma = 10^{-15}$ cm^2, and $\nu_{th} = 5\times10^6$ cm/s, the coefficient A is calculated to be $1/\tau_{nr} = N_t\sigma\nu_{th} = 5\times10^7$ s^{-1}, which is similar to other reports[80]. The value of the coefficient B also can be calculated with a process described in Ref. [81] to be $G/n_i^2 = 4.1\times10^{-9}$ cm^3 s^{-1} for GaN, where G is the generation rate per unit volume and n_i is the intrinsic carrier concentration. In case of InGaN, the coefficient B becomes around 1.2×10^{-10} cm^3 s^{-1}.

However, this model assumes that all the carriers are consumed by the recombination and do not consider the effect of the carrier loss via the spill-over. The carriers lost by the spill-over can be included into the model by introducing the spill-over current density, as follows[81]:

$$(J - J_{spillover})/qd = An + Bn^2 + Cn^3 + J_{spillover}/qt \text{ , and} \quad (5\text{-}3)$$

$$\eta_{int} = Bn^2/(An + Bn^2 + Cn^3 + J_{spillover}/qt) \text{ .} \quad (5\text{-}4)$$

In Equation 5-3 and 5-4, the amount of the spilled-over carriers are correlated with the spill-over current density $J_{spill\text{-}over}$ by using the diffusion length of the spilled carriers, t. An exact estimation of the absolute amount of the spilled-over carriers is very hard. Instead, the spill-over current density was assumed to be proportional to the injection current density with the following equation:

$$J_{spillover} = kJ^b \text{ .} \quad (5\text{-}5)$$

where k and b are constants controlling the amount of the spill-over current density, reflecting the electron-confinement capability of the material structure. On the other hand, the hole-blocking effect will cause an imbalance in the number of the electrons and holes in the active region. If the hole density is not comparable to that of the electrons, the rate of the radiative recombination may decrease even if enough number of electrons are present in the active region.

To represent the hole deficiency caused by the EBL, the ratio between the excess electron density and the excess hole density (carrier-density ratio) is described by a function of the injection-current density rather than just a constant. Under the same height of the hole barrier caused by the EBL, the relative density of the excess hole will change with the total injection-current density. Because the portion of the holes blocked by the EBL become smaller compared to the total number of the injected holes, the excess hole density is expected to be much lower than the excess electron

density at a low current density and becomes comparable to the electron density at a high current density. This behavior in the carrier-density ratio along with the injection-current density can be described by Fermi-Dirac distribution function. In this case, the carrier-density ratio is set to a function of the excess electron density, as follows:

$$f(\Delta n) = 1/(1 + \exp((F - \Delta n)/G)) \,, \tag{5-6}$$

where *F* and *G* are parameters to control the hole-blocking behavior. The parameters *F* and *G* have similar characteristics to the Fermi energy and the temperature in the original Fermi-Dirac distribution function. Therefore, the density of the excess holes is represented as follows:

$$\Delta p = \Delta n \cdot f(\Delta n) \,. \tag{5-7}$$

An example of the carrier-density ratio function and the resulting hole density are shown in Figure 5-7 along with the electron density. In Figure 5-7 (a), the carrier-density ratio represented by the function *f(Δn)* is very small in low electron-density region, and rapidly approaches 1.0 with the increase of the electron density. This curve represents the expected transient of the hole density that it will be similar to the electron density at a high injection-current density. The resulting hole density behavior along with the electron density is shown in Figure 5-7 (b). The curve plotted in Figure 5-7 (b) indicates that the imbalance between the hole density and the electron density is improved with the increase of the current density, and the hole density become similar to the electron density under a high injection-current density.

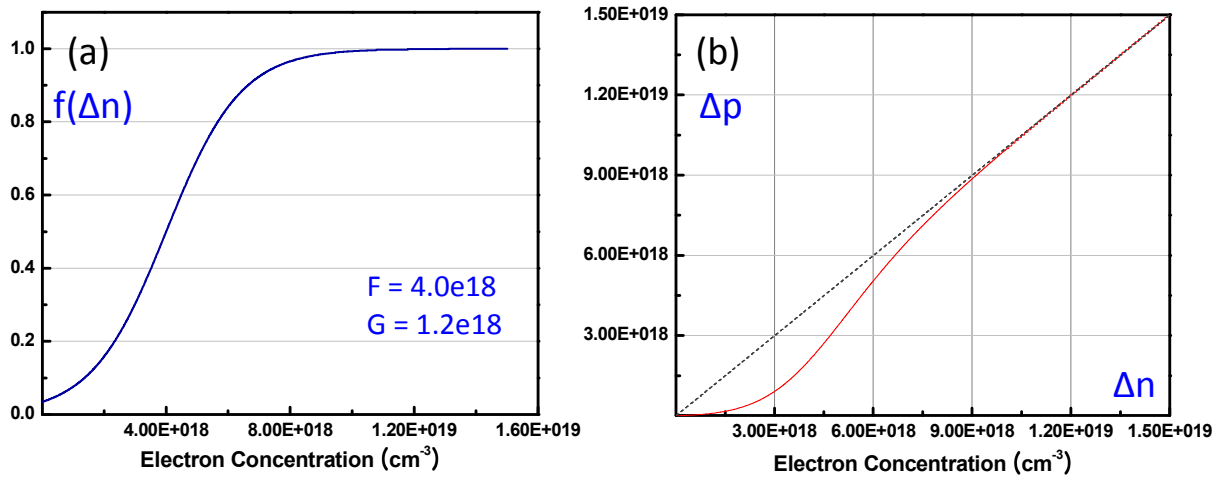

Figure 5-7. (a) The carrier-density ratio shown as a function of the electron density (b) the excess hole concentration obtained from the carrier-density ratio function

Also, the rate equations of the recombination processes shown in Equation 5-1 and 5-2 are simplified forms under the assumption that the hole density and the electron density are same. When the hole density and the electron density are not same, the rate equations should be expressed in their original forms that include the hole density, as follows:

$$U_{Auger} = C\Delta p(n_0 + \Delta n)\,, \tag{5-8}$$

$$U_{SRH} = 2A\Delta p\Delta n/(\Delta p + \Delta n)\,, \quad \text{and} \tag{5-9}$$

$$R = B\Delta p\Delta n\,. \tag{5-10}$$

Based on the "extended ABC model" discussed above, the transition of the quantum-efficiency curve under the different electron spill-over and the hole blocking conditions is simulated for a comparison. The recombination coefficients *A*, *B*, and *C* were fixed through the calculation process, and only the hole-blocking parameters *F*/*G* (in Equation 5-6) and the carrier spill-over parameter *k*/*b* (in Equation 5-5) are changed to adjust the hole density and the spill-over current density. The change of the quantum-efficiency curve along with the different spill-over current density is shown in Figure 5-8.

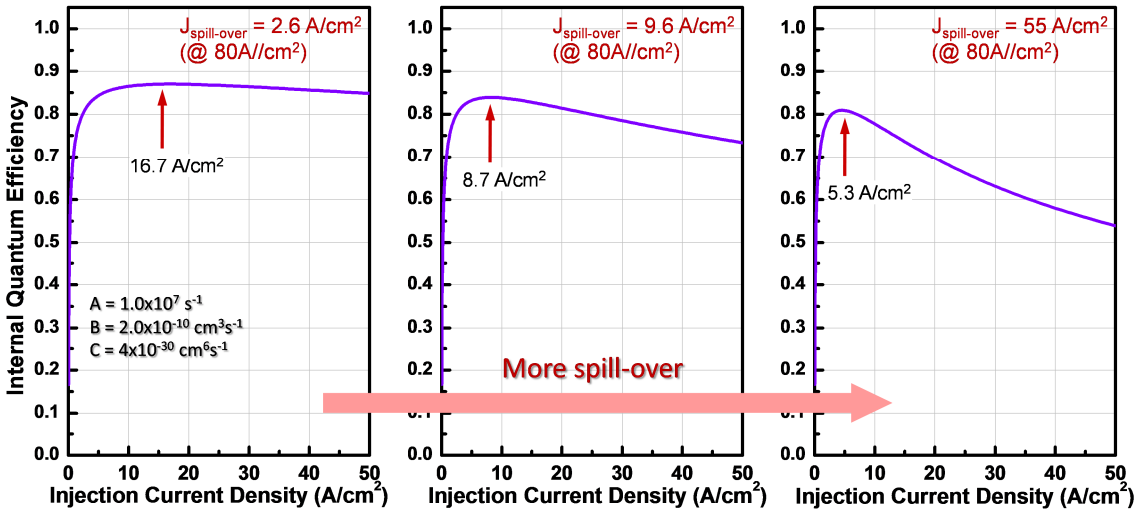

Figure 5-8. The transition of the calculated quantum-efficiency curve with the increase of the spill-over current density.

When there is no carrier spill-over, the peak quantum efficiency appears at the current density of 16.7 A/cm^2, as shown in Figure 5-8 (a). If the carrier spill-over is increased by setting larger values of the parameters *k* and *b*, the position of the peak efficiency shifts toward a lower current density (Figure 5-8 (b) and (c)). Also, the quantum-efficiency curves show a more rapid decrease of the efficiency under higher carrier spill-over conditions, making the shape of the curve sharper. The change of the quantum-efficiency curves caused by different values for the hole blocking effect is simulated by using similar process. The quantum-efficiency curves calculated by the model with different amount of the hole blocking under the same carrier spill-over condition are shown in Figure 5-9.

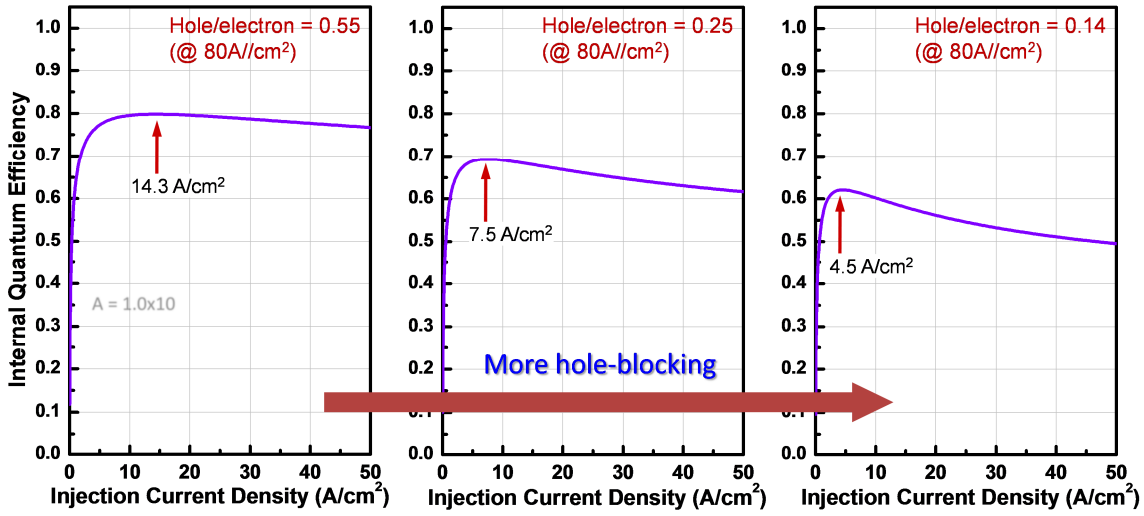

Figure 5-9. The transition of the calculated quantum-efficiency curve with the increase of the hole-blocking effect.

In Figure 5-9, the hole-blocking effect is increased (and hole-electron ratio is decreased) by changing the hole-density parameter *F* and *G*. The peak efficiency initially appears at 14.3 A/cm^2 under a relatively low hole-blocking effect (or a high hole-density condition) shifted to the lower current density with the increase of the hole-blocking effect (or decrease of the hole density). Also, it is clear that the quantum-efficiency curve with higher hole-blocking effect shows more rapid decrease in the efficiency at a high current density. These results indicate that a LED structure with a smaller spill-over current density will reach its peak quantum efficiency at higher current density. It is also predicted that a LED with a high hole-blocking effect will show a peak efficiency at a low current density with a large droop in the quantum-efficiency curve, even if the spill-over current of the structure is well suppressed.

The spill-over current density and the hole-blocking effect of the blue LEDs with different EBLs were analyzed by using the "extended ABC model" described above. The quantum-efficiency curves of the LEDs were numerically fitted through the quantum-efficiency model, and the fitting parameters were examined to estimate the spill-over current density and the hole density with respect

to the excess electron density. A numerical fitting result on the LED without an EBL according to the proposed model is shown in Figure 5-10.

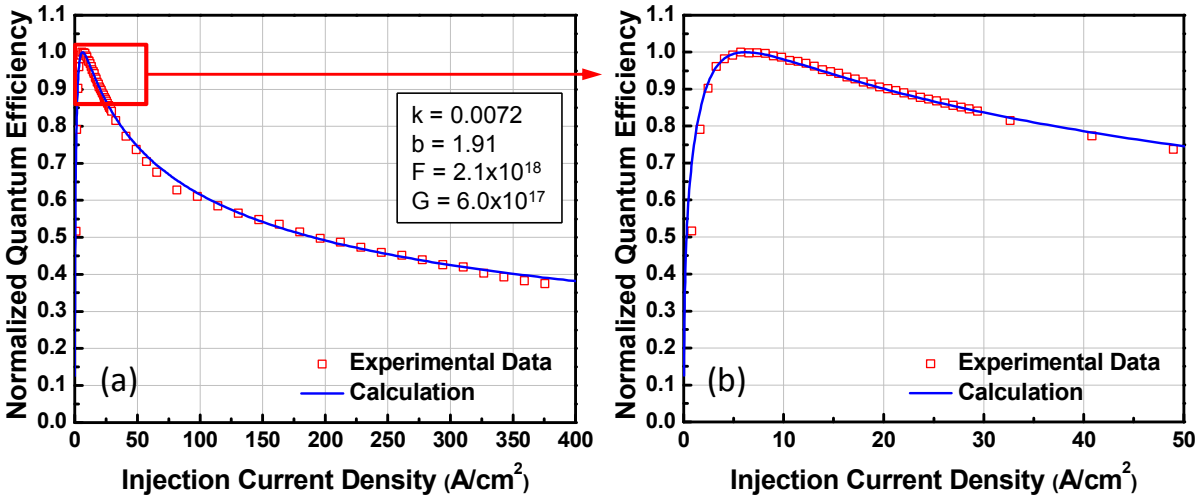

Figure 5-10. A numerical fitting result on the quantum-efficiency curve of the LED without an EBL by using the proposed "extended ABC model".

In Figure 5-10, the hollow squares represents the measured efficiency curve of the LED without an EBL, and the solid line is a fitting curve calculated by the quantum-efficiency model fed with an appropriate parameter sets. The fitting curve shows a very good agreement with the measured efficiency curve in all current density regions. From the numerical fitting of the efficiency curve, the hole-blocking parameters F/G and the spill-over parameters k/b are obtained to calculate and compare the amount of the spill-over current density and the ratio between the electron density and the hole density. During the numerical fitting on the LEDs with different EBLs, the recombination coefficients of A, B, and C are fixed, because the active region of all LEDs is identical. The transition of the spill-over current density and the carrier-density ratio at the injection-current density of 150 A/cm^2 and 300 A/cm^2 is plotted in Figure 5-11 along with the EBL thickness. The quantum-efficiencies of the LEDs

with different $In_{0.19}Al_{0.81}N$ EBL thicknesses at the same injection-current density is also shown in Figure 5-11 (b) and (d).

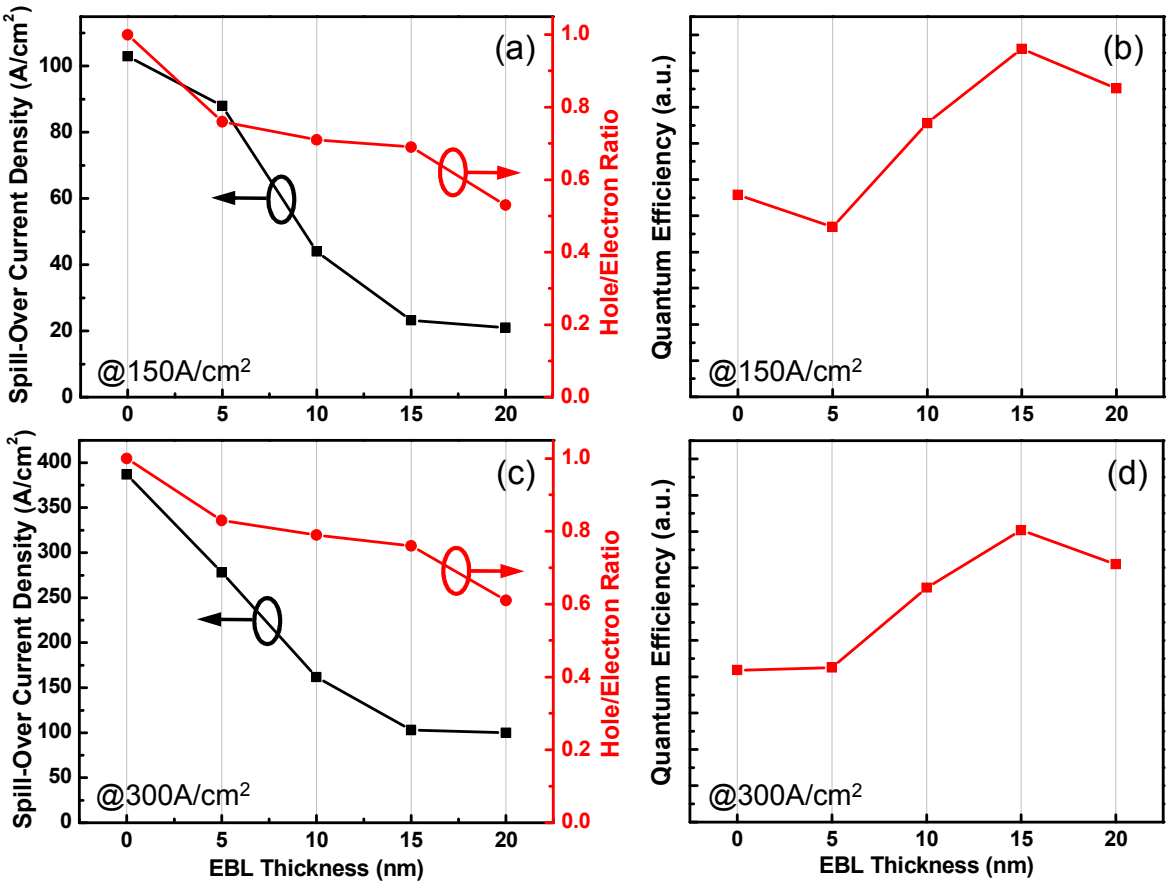

Figure 5-11. Calculated spill-over current density and hole density at injection-current densities of (a) 150 A/cm^2 and (c) 300 A/cm^2. The quantum efficiency of each LED structure at (b) 150 A/cm^2 and (d) 300 A/cm^2 are also shown.

The spill-over current density and the hole density show a similar trend in Figure 5-11 (a) and (c): they decrease with the increase of the EBL thickness. However, their transition does not overlap completely with each other. For example, the LED with a 20 nm $In_{0.19}Al_{0.81}N$ EBL has a slightly reduced spill-over current density but a much lower hole density (or much higher hole-blocking effect) than the LED with a 15 nm EBL at J = 150 A/cm^2. This prediction is consistent with the observation

shown in Figure 5-11 (b) that the LED with a 20 nm EBL has lower quantum efficiency than the LED with a 15 nm EBL at J = 150 A/cm^2. The observation that the LED with a 5 nm EBL has lower quantum efficiency than the LED without an EBL can be similarly explained by the calculation results that the LED with a 5 nm $In_{0.19}Al_{0.81}N$ EBL has a slightly lower spill-over current density and a much lower hole density than the LED without an EBL. Moreover, the calculation suggests that the LED with a 5 nm EBL has a significantly reduced spill-over current density compared to the LED without an EBL at the increased injection-current density of J = 300 A/cm^2. This prediction is supported by the similar or higher quantum efficiency of the LED with a 5 nm EBL over the LED without an EBL at high current-density region. Therefore, the spill-over current density and the hole density obtained by the model have good agreement with the quantum-efficiency measurement results. The highest efficiency of the LED with a 15 nm $In_{0.19}Al_{0.81}N$ EBL throughout all current-density region, which is observed in the curve, can be explained by its low spill-over current and relatively high hole density (or relatively low hole-blocking effect).

The multi-parameter fitting does not necessarily have a unique solution, and multiple sets of parameters that provide a good fitting on the quantum-efficiency curve may exist. Therefore, we carefully examined various sets of fitting parameters to ensure if they yield a similar results on the spill-over current density and the hole density. During the fitting process under the fixed *A*, *B*, and *C* values, all parameter sets that have a good agreement with the quantum efficiency yield a transition similar to the results shown in Figure 5-11 (a) and (c). Especially, the discrepancy between the spill-over current density and the hole density (much lower hole density and similar amount of spill-over current density) in the LED with a 5 nm EBL and the LED with a 20 nm EBL was predicted in all parameter sets. Although the entire parameter space was not tested, it seems that the quantum-efficiency measurement results have enough information to obtain the spill-over current density and the hole density along with the thickness of the $In_{0.19}Al_{0.81}N$ EBLs.

In conclusion, the quantum-efficiency curves of the LEDs with different $In_{0.19}Al_{0.81}N$ EBL thicknesses were analyzed by using a numerical model to obtain the electron spill-over and the hole-blocking factors. The "extended ABC model" could explain the highest quantum efficiency of the LED with a 15 nm $In_{0.19}Al_{0.81}N$ EBL is originated from the high electron-confinement effect and the relatively low hole-blocking effect of the 15 nm-thick EBL. The observation also suggests that the hole-blocking effect as well as the electron-confinement effect of the EBL should be considered to obtain high light output and efficiency performance from LEDs operated at high current densities.

5.6 Strain-engineered InAlN EBL for High Hole-Injection Efficiency

From the previous results with the quantum-efficiency model, it is obvious that the hole-blocking effect of the EBL significantly modifies the emission performance of the LED. The conventional EBL scheme has a strong trade-off effect between the performance improvement by the electron-confinement effect and the reduction of the radiative recombination by the hole-blocking effect. In many cases, the performance improvement of the EBL surpasses the impact of the hole deficiency caused by the insertion of the EBL. However, a new EBL structure that provides higher hole-injection efficiency while maintaining a high electron-confinement barrier is highly required for a further performance improvement of the LED.

The strain and polarization-field manipulation capability of the $In_xAl_{1-x}N$ layer provides a solution for an enhanced hole injection. An $In_{0.19}Al_{0.81}N$ layer is under the in-plane lattice-matching condition on a GaN layer with similar in-plane lattice constants of $In_{0.19}Al_{0.81}N$. However, if the indium composition in an $In_xAl_{1-x}N$ layer decreases below 19%, the layer experiences tensile strain, and the piezoelectric field will have a same direction to the spontaneous polarization field of the layer. On the contrary, if the indium composition of the $In_xAl_{1-x}N$ layer increases over lattice-matching regime and produces the compressive strain, the piezoelectric field will compensate the spontaneous polarization field and reduce the band bending of the $In_xAl_{1-x}N$ layer in the electronic band structure.

The strain-engineering technique in the $In_xAl_{1-x}N$ layer has been utilized in the InAlN/GaN HFET to realize an enhancement-mode operation by compensating the spontaneous polarization field and reducing the two-dimensional electron gas density [82]. Similarly, an $In_xAl_{1-x}N$ EBL with indium composition higher than 19% will have a less band bending with a smaller polarization field. The simulated band structures of the blue LEDs with $In_xAl_{1-x}N$ EBLs with different indium composition *x* from 0.19 to 0.24 are shown in Figure 5-12.

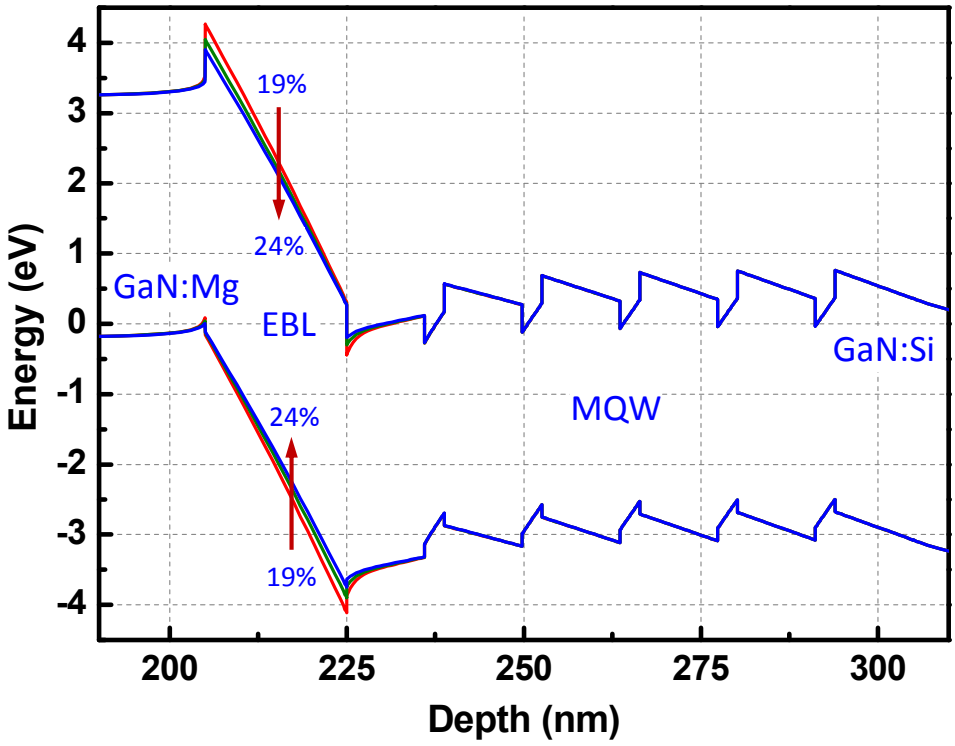

Figure 5-12. Band structure calculations of the blue LEDs with $In_xAl_{1-x}N$ EBLs with different indium composition *x* from 0.19 to 0.24.

A higher indium composition will reduce the bandgap of the $In_xAl_{1-x}N$ layer, thus the height of both the electron-blocking barrier and the hole-blocking barrier is decreased, as shown in Figure 5-12. However, because of the compressive strain and the reduced polarization, the effective height of the electron barrier at the MQW side remains almost unchanged, while the height of the hole barriers at

the *p*-type layer is greatly reduced with the increase of the indium composition. The effect of the reduced polarization field is more significant when the device is operating under a forward bias condition. The band structure simulations of the blue LED structures with $In_xAl_{1-x}N$ EBLs under a forward bias of 3V are shown in Figure 5-13.

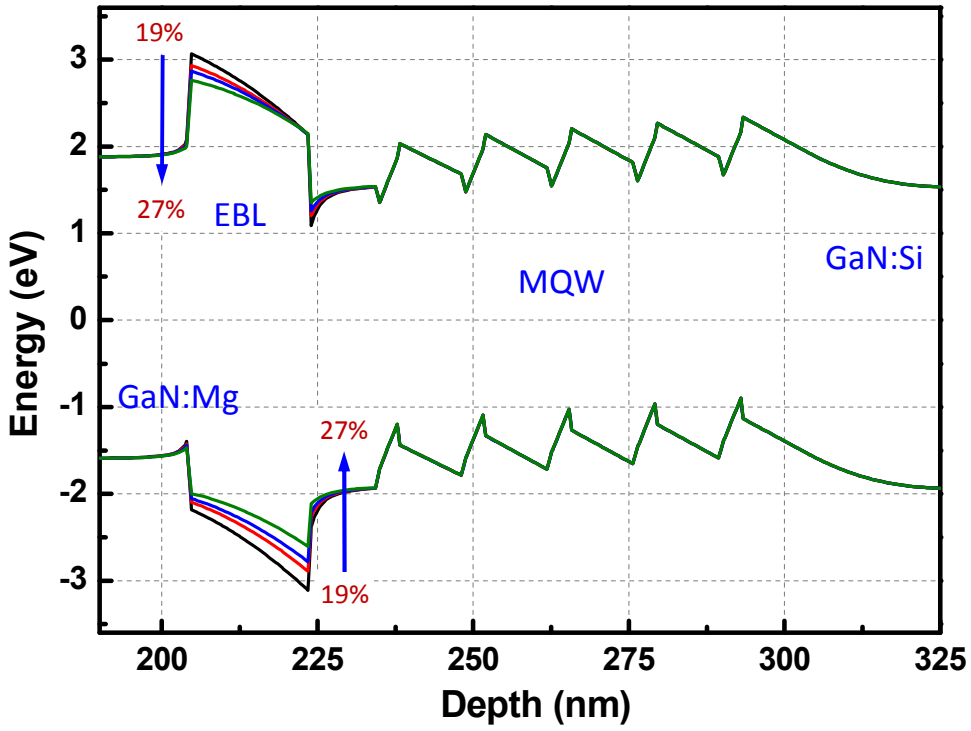

Figure 5-13. Band structure calculations of the blue LEDs with $In_xAl_{1-x}N$ EBLs with different indium composition *x* from 0.19 to 0.24 under the forward bias voltage of 3V.

In Figure 5-13, the effective height of the electron-confinement barrier of the EBL is maintained to be similar regardless of the indium composition and reduced bandgap of the $In_xAl_{1-x}N$ layer under the forward bias. However, the height of the hole barrier decreases rapidly with the increase of the indium composition. Therefore, an $In_{0.24}Al_{0.76}N$ EBL will provide a high electron-confinement effect with a higher hole-injection efficiency. For more detailed analysis on the hole and electron density in the

LED structure with a strain-engineered EBL, the excess hole density distribution under a 4V forward bias condition is calculated by using SiLENSe software and shown in Figure 5-14.

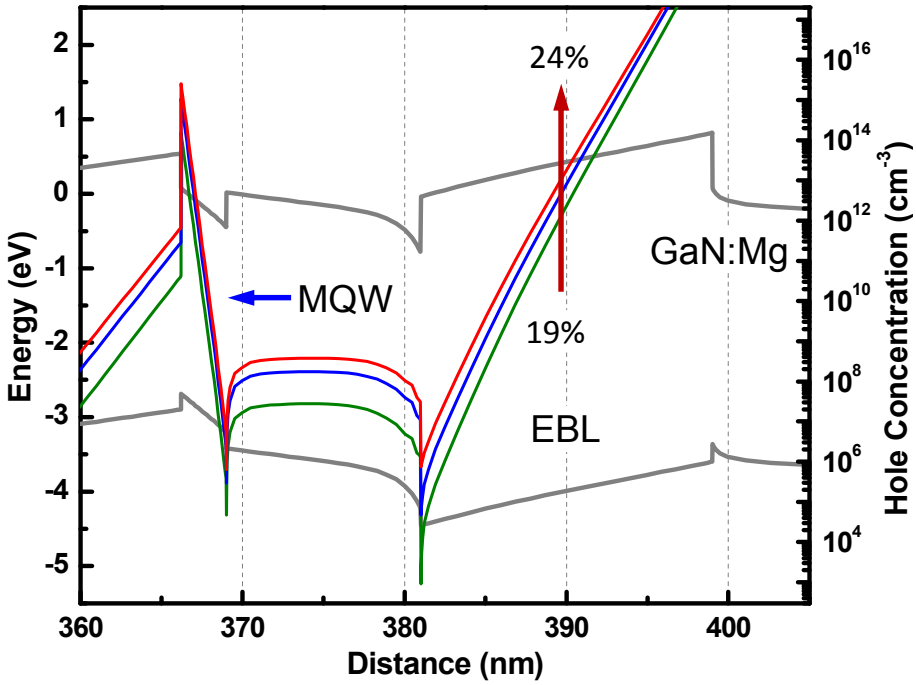

Figure 5-14. Calculated hole concentration of the LEDs with $In_xAl_{1-x}N$ EBLs with indium composition *x* from 0.19 to 0.24 under the forward bias voltage of 4V.

In the simulation result, a high hole concentration exists at the interface between the GaN:Mg layer and the $In_xAl_{1-x}N$ EBL because of a "well" in the valence band generated by the band offset between the EBL and the GaN:Mg layers. In the MQW region, most of hole is located at the QW region, while the hole concentration at the barrier region is very low. With the increase of the indium composition in the EBL, the hole concentration in the MQW region is observed to be increased. The electron concentration in the MQW region is, however, almost unchanged with the indium composition in the EBL. These results support the effect of the strain-engineering in the $In_xAl_{1-x}N$ EBL in enhancing the hole-injection efficiency without degrading the electron-confinement effect.

5.6 Growth and Fabrication of the Strain-engineered InAlN EBLs

As shown in Chapter 4, InAlN layers have many similarities with InGaN layers in terms of the growth conditions. The indium composition of the InAlN layer is enhanced by lowering the growth temperature, as shown in Figure 4-1. Therefore, we controlled the growth temperature to obtain $In_xAl_{1-x}N$ layers with higher indium composition. For a calibration and confirmation of the indium composition in the $In_xAl_{1-x}N$ layer, 100 nm-thick $In_xAl_{1-x}N$ test layers were grown on GaN/sapphire templates under different growth temperatures. The growth pressure was 300 Torr, and the growth temperature was changed from 845 ^oC down to 800 ^oC. The HR-XRD ω-2θ-scan results in (004) diffraction on the test samples are shown in Figure 5-15.

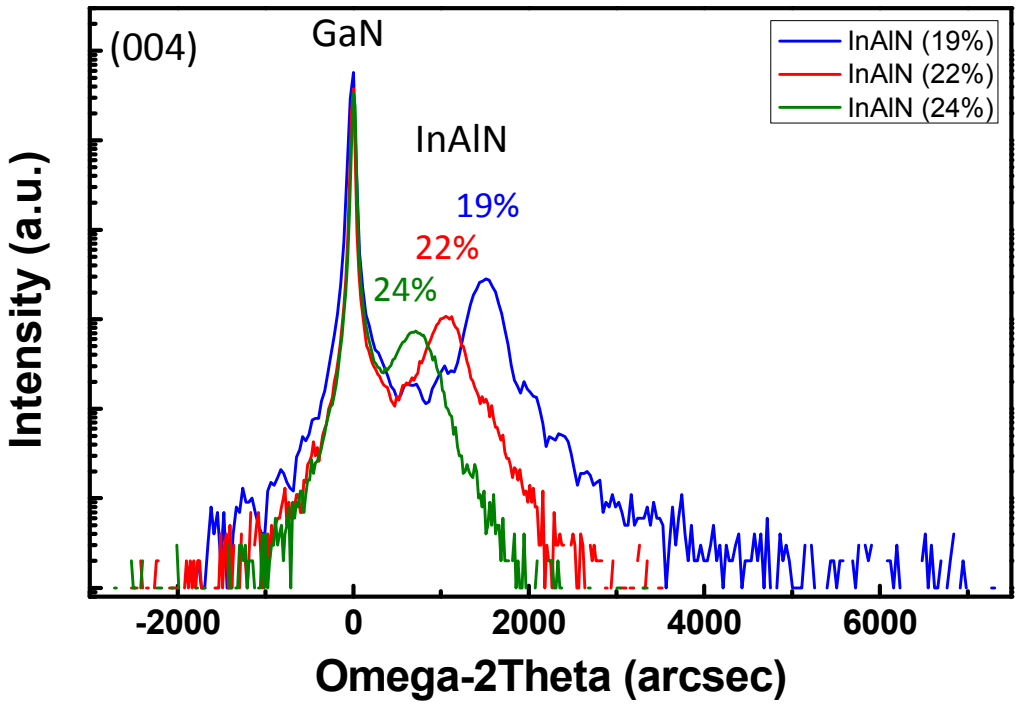

Figure 5-15. HR-XRD ω-2θ-scan results of the $In_xAl_{1-x}N$ test samples in (004) diffraction.

The peaks from the $In_xAl_{1-x}N$ layer grown at lower temperature appear at smaller ω angle, confirming that the increase of the vertical lattice constant with higher indium composition. The calculated indium composition of the layer grown at 800 ^oC is 24%, assuming that the layer is fully strained. The $In_xAl_{1-x}N$ layers grown by these conditions were employed in the standard blue LED structures as strain-engineered EBLs. The blue LED samples have layer structure and growth conditions very similar to the samples described in Chapter 4.3 and Chapter 5.3.

According to the previous growth results, an $In_xAl_{1-x}N$ layer grown at lower temperature tends to show rough surface morphology. The induced compressive strain of the $In_xAl_{1-x}N$ EBLs with higher indium composition is also a potential origin of the surface roughening. The surface images of the as-grown blue LEDs with and without strain-engineered $In_xAl_{1-x}N$ EBLs observed by AFM are shown in Figure 5-16.

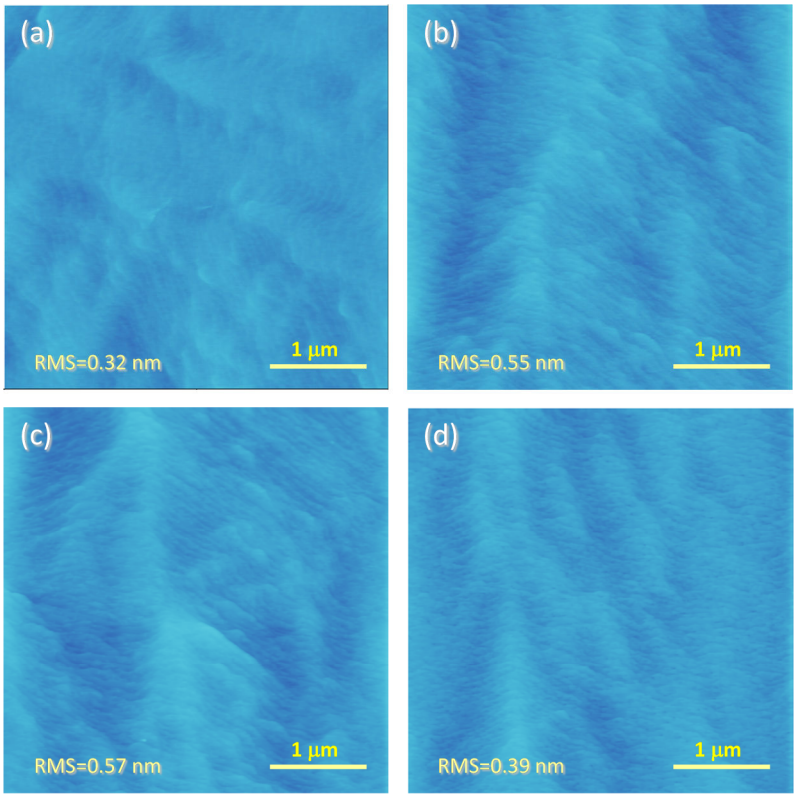

Figure 5-16. Surface morphology of the blue LEDs (a) without an EBL, (b) with an $In_{0.19}Al_{0.81}N$ EBL, (c) with an $In_{0.22}Al_{0.78}N$ EBL, and (d) with an $In_{0.24}Al_{0.76}N$ EBL.

The surfaces of the LEDs without and with EBLs show similar morphology and roughness regardless of the indium composition in the $In_xAl_{1-x}N$ EBLs. The relatively thin thickness (20 nm) of the $In_xAl_{1-x}N$ EBLs might suppress the significant roughening of the surface.

These LED structures were fabricated into 350×350 μm^2 devices by using a standard top-emitting chip process as described in Chapter 4.3. The fabricated devices have a very similar mesa definition and metal contact configurations to the device shown in Figure 4-13.

5.7 Characterization of the LEDs with Strain-engineered InAlN EBLs

The electroluminescence of the LEDs with strain-engineered $In_xAl_{1-x}N$ EBLs was measured with a pulse-mode injection current up to 460 mA (J~375 A/cm^2) at room temperature without any

forced cooling. The measured integrated EL intensity of the LEDs were plotted in Figure 5-17 along with the injection current.

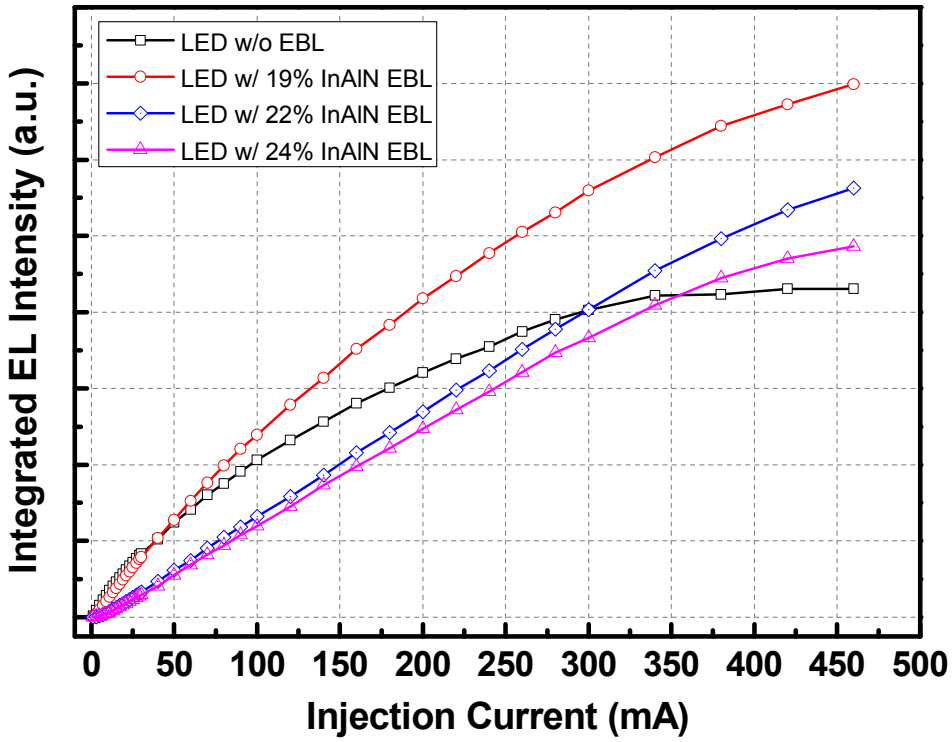

Figure 5-17. Integrated EL intensities of the LEDs without an EBL and with $In_xAl_{1-x}N$ EBLs with different indium composition *x* from 0.19 to 0.24 plotted along with the injection current.

In Figure 5-17, the LED without an EBL shows a significant saturation of the integrated EL intensity at the high injection current region. The LED shows a sub-linear increase of the integrated EL intensity even at low current region around *I*~150 mA, and the light output shows very little increase with the increase of the injection current at higher current region of *I*>350 mA. This severe efficiency droop behavior is very consistent with the previous measurement results on the LEDs without an EBL shown in Chapter 4.5 and Chapter 5.4. The behavior of the LED with an $In_{0.19}Al_{0.81}N$ EBL is also similar to the previous observations. The LED with an $In_{0.19}Al_{0.81}N$ EBL shows a slightly lower light

output than the LED without an EBL at I<50 mA, but it shows much steeper increase in the light output at the high current region because of its reduced carrier spill-over. As a result, the LED with an $In_{0.19}Al_{0.81}N$ EBL shows around 75% higher light output than the LED without an EBL at the injection current of 460 mA. On the other hand, the LED with an $In_{0.22}Al_{0.78}N$ EBL and the LED with an $In_{0.24}Al_{0.76}N$ EBL also show more linear increase of the EL intensity and 30% and 15% higher absolute light output than the LED without an EBL at the current of 460 mA, respectively. However, their absolute light output is lower than the LED with a lattice-matching $In_{0.19}Al_{0.81}N$ EBL in all current range, in spite of their very linear increase of the EL intensity. Because the insertion of the strain-engineered EBL with higher indium composition into the LED structure is expected to improve both absolute light output and the quantum efficiency, this measurement result is somehow surprising. The low integrated EL intensity of the LEDs with strain-engineered EBLs will be discussed later.

To extract the information on the electron-confinement effect and the hole-blocking effect, the quantum-efficiency curves of the LEDs are plotted in Fig 5-18.

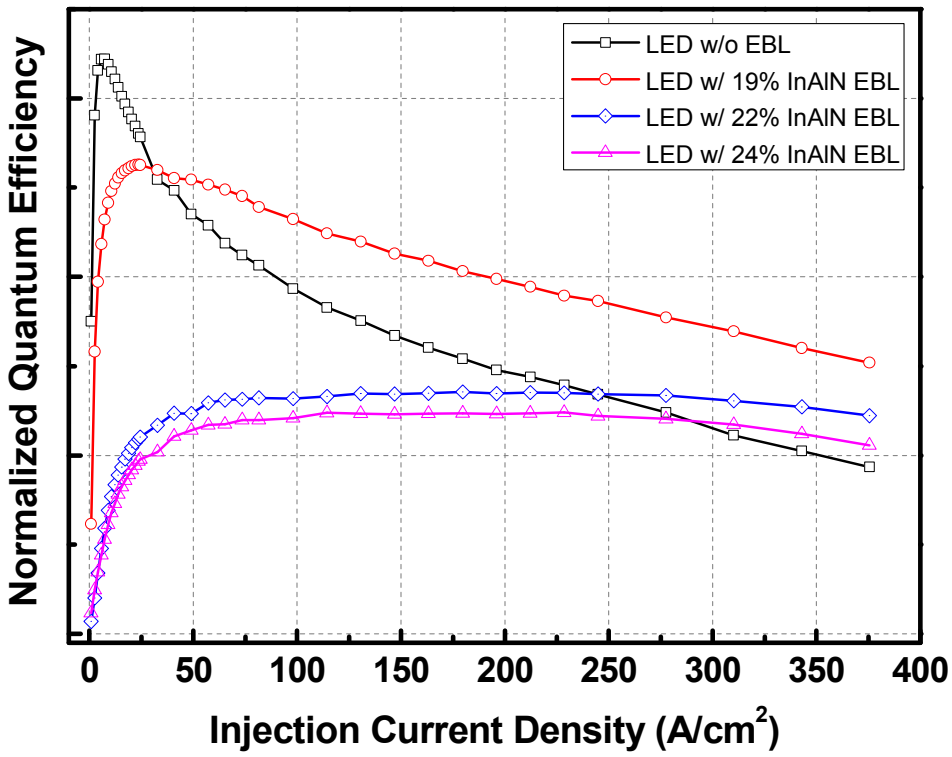

Figure 5-18. Quantum-efficiency curves of the LEDs without an EBL and with $In_xAl_{1-x}N$ EBLs with different indium composition *x* from 0.19 to 0.24 plotted along with the injection current density.

All the curves plotted in Figure 5-18 show a typical quantum-efficiency behavior with an injection current density. The quantum efficiencies of the LEDs increase with the current density increase under low current-injection conditions to reach its peak efficiency and decrease under high injection conditions. The LED without an EBL shows very high peak efficiency at a low current density (7.3 A/cm^2) but also shows a rapid decrease of the quantum efficiency at higher current densities suffering from a large efficiency droop. On the other hand, the absolute peak efficiency of the LED with an $In_{0.19}Al_{0.81}N$ EBL is lower than the LED without an EBL at a low current density. However, the peak efficiency of the LED with an $In_{0.19}Al_{0.81}N$ EBL appears at higher current density of 23.7 A/cm^2. Also, a much smaller efficiency droop of the LED leads to a much higher quantum efficiency at a high current density of 375 A/cm^2 over the LED without an EBL. The LEDs with an $In_{0.22}Al_{0.79}N$ EBL and

an $In_{0.24}Al_{0.76}N$ EBL show rather low quantum efficiency than the LED without an EBL at lower current density, as observed in the comparison of the integrated EL intensity in Figure 5-17. However, their efficiency droop is very small, and their peak efficiency appears at high current densities over 100 A/cm^2. As a result, the LEDs with an $In_{0.22}Al_{0.79}N$ EBL and an $In_{0.24}Al_{0.76}N$ EBL show more than 15% higher quantum efficiency compared to the LED without an EBL.

Because the active region and other layers of the blue LEDs were carefully maintained to be same during the growth process, the dramatic change in the quantum-efficiency curves might be originated from the different hole-injection efficiencies and electron-blocking effects of the EBLs. To analyze the hole blocking and the electron confinement characteristics of the EBLs, the quantum-efficiency model described in Chapter 5.5 is employed. As the material growth conditions and the layer structure of the blue LEDs are very similar to the previous LED samples in Chapter 5.4, similar values are used for recombination coefficients *A*, *B*, and *C*. The quantum-efficiency model with appropriate parameter sets provides a good fitting on the quantum-efficiency curves of the LEDs, as shown in Figure 5-19.

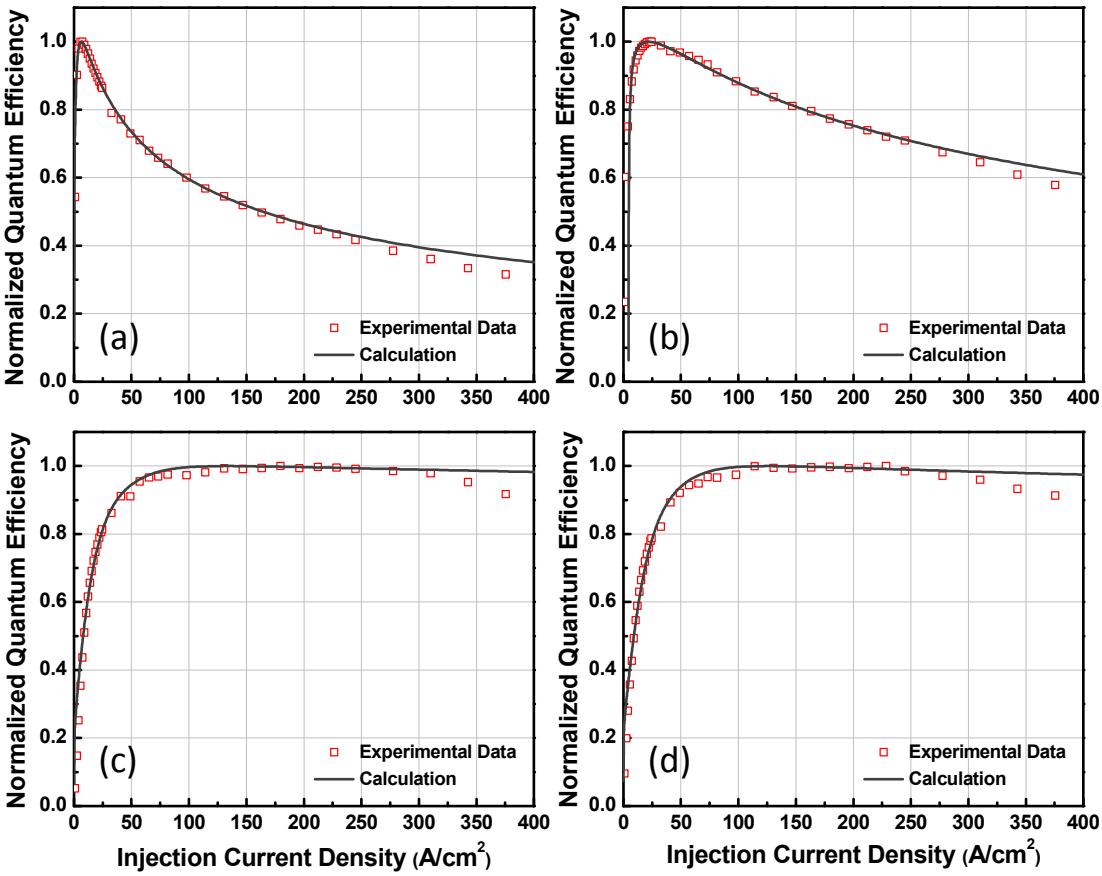

Figure 5-19. Numerical fitting results on the quantum-efficiency curves of the LEDs (a) without an EBL, (b) with an $In_{0.19}Al_{0.81}N$ EBL, (c) with an $In_{0.22}Al_{0.78}N$ EBL, and (d) with an $In_{0.24}Al_{0.76}N$ EBL by using the proposed "extended ABC model".

The spill-over current density and the carrier-density ratio at 150 A/cm^2 are calculated from the numerical fitting parameters and plotted in Figure 5-20.

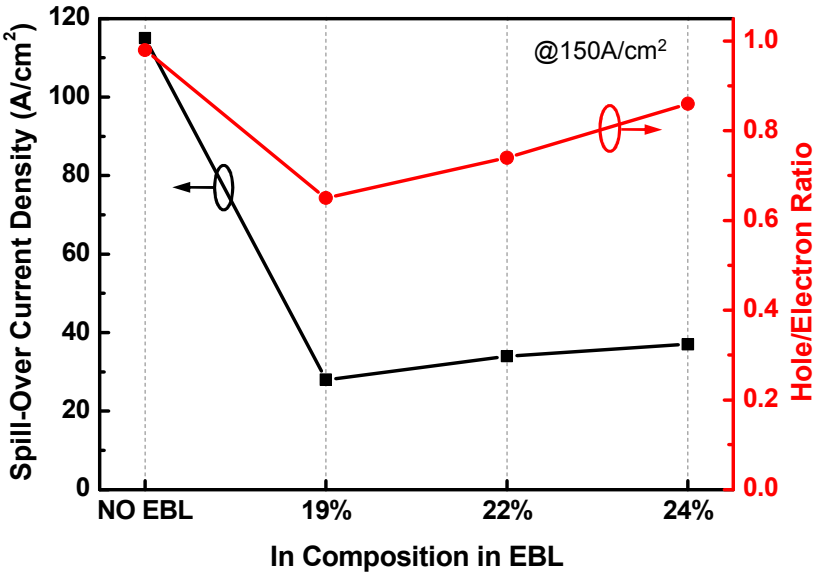

Figure 5-20. Calculated spill-over current density and hole density of the LEDs without an EBL and with strain-engineered $In_xAl_{1-x}N$ EBLs at injection-current densities of 150 A/cm^2.

The calculation results in Figure 5-20 show a very consistent trend with the previous results shown in Figure 5-11 in Chapter 5.4. According to the calculation, the LED without an EBL has a high spill-over current density and a high excess hole density with the lowest electron-confinement and hole-blocking effect. The insertion of the EBL could reduce the high spill-over current density dramatically, but it also brings a high hole barrier and a low hole density, as shown in the result of the LED with an $In_{0.19}Al_{0.81}N$ EBL. On the other hand, the LED with an $In_{0.22}Al_{0.78}N$ EBL shows a higher hole density than the LED with a lattice-matching $In_{0.19}Al_{0.81}N$ EBL because of narrower bandgap and lower hole-blocking barrier of the EBL. The calculation also suggests that the reduced bandgap of an $In_{0.22}Al_{0.78}N$ EBL increases the spill-over current, but the amount of the increase in the spill-over current is limited to 15% over the LED with an $In_{0.19}Al_{0.81}N$ EBL. This implies that the increased piezoelectric polarization and a reduced band bending can maintain the electron-confinement capability of the EBL, even if the bandgap of the EBL is reduced. The LED with a strain-engineered $In_{0.24}Al_{0.76}N$ EBL also

shows a similar trend: the hole density of the LED is higher than the LED with an $In_{0.22}Al_{0.78}N$ EBL, but the spill-over current density is well suppressed in spite of the narrower bandgap of the $In_{0.24}Al_{0.76}N$ EBL.

These results are well-matched with the trend of the peak efficiency positions which appear in the quantum-efficiency curves of the LEDs. When other parameters such as the recombination coefficients are fixed, the spill-over current density and the carrier-density ratio are two important factors in determining the peak position and the shape of the quantum-efficiency curve. The appearance of the peak efficiency at higher current density and smaller efficiency droop in the LEDs with $In_{0.22}Al_{0.78}N$ and $In_{0.24}Al_{0.76}N$ EBLs imply that the enhanced hole injection is more dominant than the decline in the electron-blocking effect. This supports the main idea of the strain-engineered $In_xAl_{1-x}N$ EBL that the electron-confinement effect is maintained under a forward bias by the reduced band bending while the hole-blocking barrier is reduced with its low indium composition is actually working.

However, the actual light output of the LEDs with the strain-engineered EBLs is lower than the LED with a lattice-matching $In_{0.19}Al_{0.81}N$ EBL. The EL measurement results are not consistent with the analysis results indicating that the LEDs with the strain-engineered EBLs have comparable electron-confinement effect and higher hole density. The proposed quantum-efficiency model works on the transition of the measured quantum-efficiency curve along with the current density to extract various parameters. Therefore, the model traces the trend of the relative values of the quantum efficiency at each current density, and the absolute value of the quantum efficiency is not considered in the analysis. The prediction of the actual light output by using the recombination-based model is very difficult, as the actual performance is determined not only by the ratio between the radiative and non-radiative recombination processes, but also by many parameters outside the active region. For example, if the electrical properties of the LEDs are not identical, then the luminous performance of the LEDs will be different even if the characteristics of the active region are same. In our growth

conditions, the indium composition of the $In_xAl_{1-x}N$ EBLs was increased by reducing the growth temperature. However, a lower growth temperature often degrades the layer quality, and especially, the electrical performance of the *p*-type doped layers via a generation of carbon impurities that compensate the active magnesium dopant. The current-voltage measurement results on the LED without an EBL and with $In_xAl_{1-x}N$ EBLs are shown in Figure 5-21.

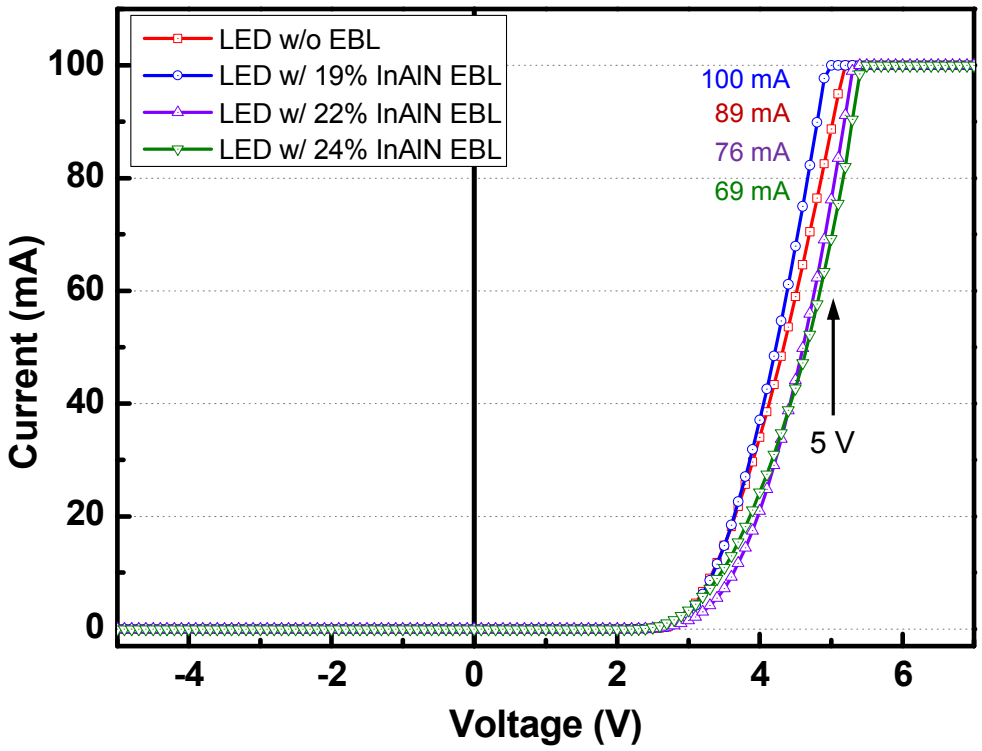

Figure 5-21. Current-voltage measurement results of the LEDs without an EBL and with $In_xAl_{1-x}N$ EBLs with different indium composition *x* from 0.19 to 0.24.

Unlike the current-voltage measurement results of the previously studied LEDs, the results in Figure 5-20 shows a large difference between the samples. Especially, the LEDs with strain-engineered $In_xAl_{1-x}N$ EBLs show much worse electrical properties. The LEDs with strain-engineered EBLs show 8% larger forward voltage at 20 mA than the LED without an EBL and the LED with a lattice-matching $In_{0.19}Al_{0.81}N$ EBL. The current flow at higher bias shows even worse result, showing around

30% lower current drive at the voltage of 5V. These results indicate that the different growth temperature of the $In_xAl_{1-x}N$ EBL caused a severe degradation in the conductivity and the quality of the *p*-type region. Therefore, a development of the growth condition to control the indium composition in the $In_xAl_{1-x}N$ layer without degrading the layer quality is necessary to demonstrate the performance enhancement of the LED with a strain-engineered $In_xAl_{1-x}N$ EBL.

5.8 Enhanced Emission Performance of the LED with a Graded InAlN EBL

The hole blocking of the EBL originates from a high energy barrier in the valence-band side formed by an EBL with a wide bandgap. Especially, a sharp spike of the valence band at the interface between the EBL and the last QW barrier creates an extra height to the hole barrier. One of the methods to remove this valence-band spike is the compositional grading at the interface. The compositional grading technique is a commonly used technique to remove the energy band discontinuity in many applications where a high carrier-injection efficiency is important, including InGaN/GaN HBTs [83,84] and visible-wavelength laser diodes [85]. For a LED structure with an $In_{0.19}Al_{0.81}N$ EBL, the compositional grading from the last barrier toward the EBL will achieve a tapered potential profile and mitigate the valence-band discontinuity. To achieve a tapered potential profile for the $In_xAl_{1-x}N$ EBLs, using InGaN last QW → InAlN EBL grading seems to be similar in terms of one Group III element exchange for the grading (*e.g.*, gallium ramping down, while aluminum ramping up for InGaN → InAlN grading). The compositional grading of InGaN → InAlN will be more controllable and technically less challenging than the grading of InGaN → AlGaN in case of the AlGaN EBL, since the InGaN → InAlN grading does not require a significant temperature ramping as opposed to the InGaN → AlGaN grading.

Band structure simulation results of an LED structure with an abrupt $In_{0.19}Al_{0.81}N$ EBL and a graded $In_{0.19}Al_{0.81}N$ EBL are shown in Figure 5-22. The alloy composition is graded from the last QW toward the $In_{0.19}Al_{0.81}N$ EBL by linearly decreasing the indium composition and increasing the

aluminum composition. The thickness of the EBL is set to 20 nm for both cases, and the thickness of the grading region is 10 nm.

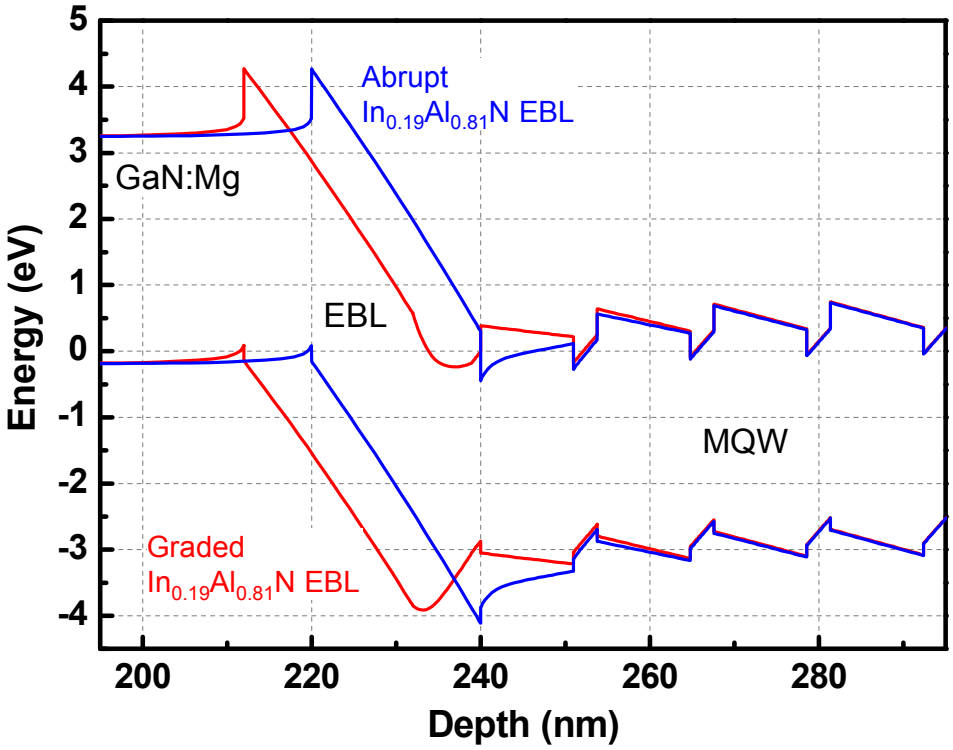

Figure 5-22. Calculated band structures of the blue LEDs with an abrupt $In_{0.19}Al_{0.81}N$ EBL and a graded $In_{0.19}Al_{0.81}N$ EBL at an equilibrium status.

The compositional grading from the last InGaN QW to the $In_{0.19}Al_{0.81}N$ EBL clearly transforms the sharp spike of the valence band at the interface between the EBL and the last QW into a rounded shape. Therefore, the effective height of the hole barrier is decreased, and the hole injection efficiency is expected to be enhanced. This will lead to a higher hole concentration in the active region. The hole concentration of the LED structures with an abrupt EBL and with a graded EBL under a forward bias of 3.5V is calculated and compared in Figure 5-23.

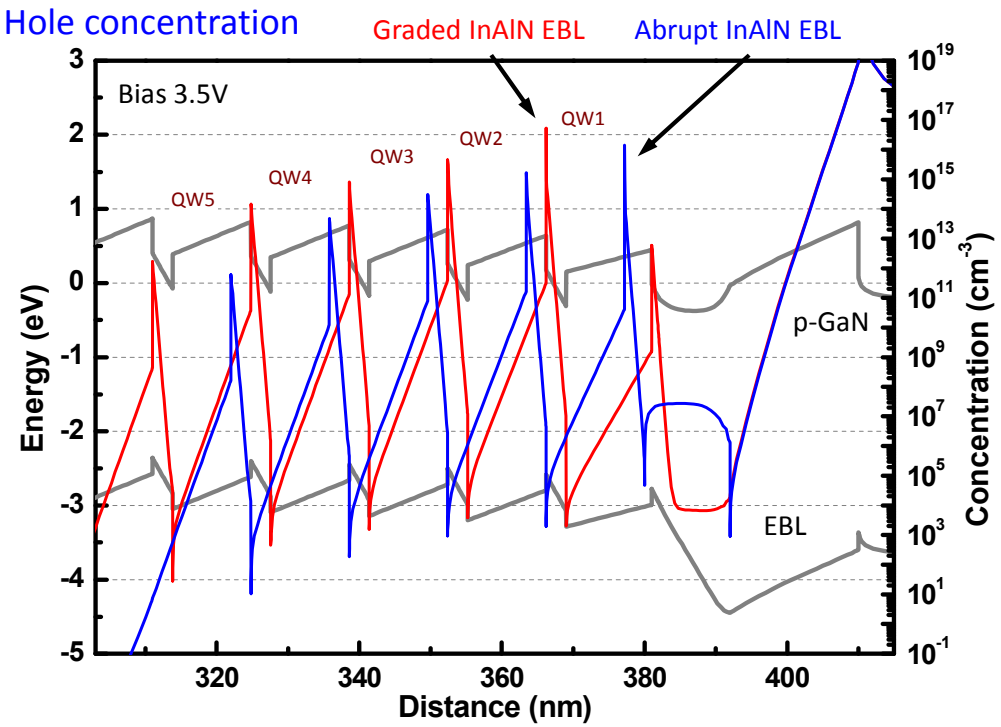

Figure 5-23. Calculated hole concentration of the LED with an abrupt $In_{0.19}Al_{0.81}N$ EBL and the LED with a graded $In_{0.19}Al_{0.81}N$ EBL under the forward bias voltage of 3.5V.

The hole concentration at the last QW is predicted to be much higher when a compositionally graded EBL is used. Moreover, the calculation predicts that the LED with a graded EBL will show much more uniform distribution of the hole concentration in the QWs compared to the LED structure with an abrupt EBL. A uniform distribution helps increasing the overall probability of the radiative recombination in QW, and leads to an improved emission performance of the LED.

The effect of the graded $In_{0.19}Al_{0.81}N$ EBLs was examined using the standard blue LED structures as an example. LED structures with various EBL schemes, including a LED without an EBL, a LED with an $In_{0.19}Al_{0.81}N$ EBL, and a LED with a graded $In_{0.19}Al_{0.81}N$ EBL were grown under the same growth conditions. In addition to these samples, an LED with a graded $In_{0.19}Al_{0.81}N$ EBL with thinner EBL thickness was also grown to further reduce the hole-blocking barrier. The thickness

of the EBLs was maintained to be 20 nm, except for the graded thin EBL whose thickness is 10 nm. The thickness of the graded region was set to 10 nm for all graded EBLs. The grown structures were fabricated into devices using a standard top-emitting chip process.

The electroluminescence measurement results of the LEDs measured on the 350×350 μm^2 devices were shown in Figure 5-24. The integrated EL intensity of the devices is plotted with the injection current up to 420 mA (360 A/cm^2).

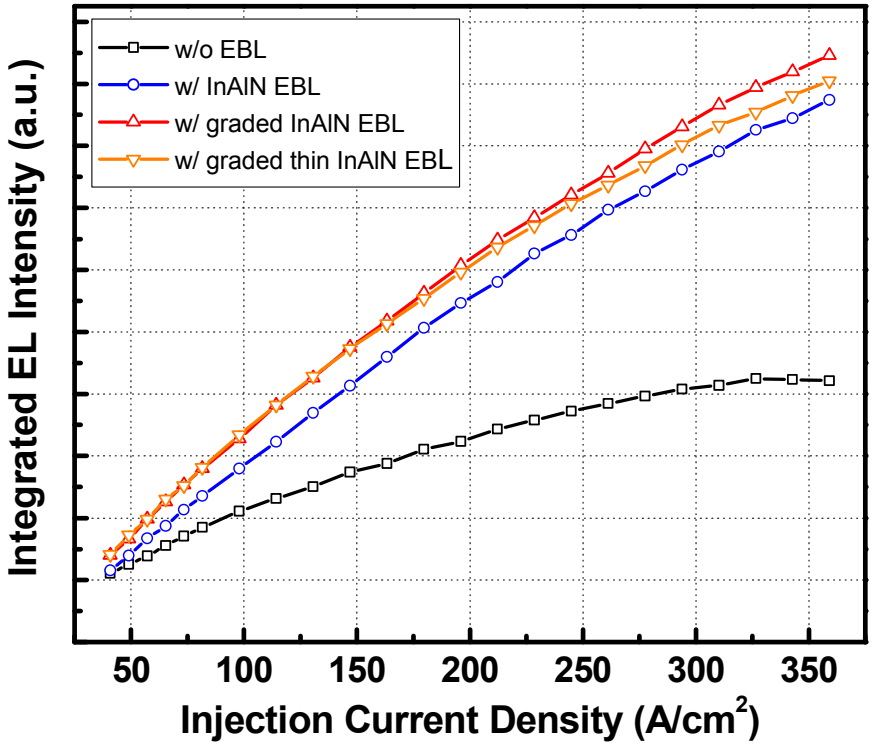

Figure 5-24. Integrated EL intensities of the LEDs without an EBL, with an abrupt $In_{0.19}Al_{0.81}N$ EBL, and with graded $In_{0.19}Al_{0.81}N$ EBLs plotted along with the injection current density.

In Figure 5-24, all LEDs with $In_{0.19}Al_{0.81}N$ EBLs show superior emission performance compared to the LED without an EBL. Especially, the LED with a graded thin $In_{0.19}Al_{0.81}N$ EBL and the LED with a

graded $In_{0.19}Al_{0.81}N$ EBL show a more linear increase of the light output than other samples at all current densities tested. As a result, the LED with a graded EBL shows an around 10% improved luminous performance over the LED with an abrupt $In_{0.19}Al_{0.81}N$ EBL at the current density of 360 A/cm^2. The LED with a graded thin EBL also shows higher performance than the LED with an abrupt EBL, but its EL intensity is lower than the LED with a graded EBL, and the slope of the light output increase is diminishing at high current density. Considering the thicker total thickness (the grading region and the EBL) of the graded EBL, and the previous results that the thicker EBL has a higher hole-blocking barrier, the compositional grading at the interface between the last QW and the EBL seems to deliver a significant enhancement in the hole-injection performance. Also, the lower performance of the graded thin EBL might originate from a smaller electron-confinement because of the thin EBL thickness. However, a quantitative analysis of the effect of the compositional grading on the hole injection and the electron-blocking effect is not performed. The results of the enhanced luminous performance of the LED with a graded EBL are still preliminary, and further studies with a numerical analysis method are required with more samples. Also, various EBL techniques introduced in Chapter 5 were examined separately but never combined with each other for further improvement of the LED performance. Their technical properties are not necessarily exclusive each other and employing multiple EBL strategies may promote their advantages while minimizing the drawbacks of each method. For example, the strain-engineered $In_xAl_{1-x}N$ EBL with higher indium composition can be combined with the grading technique for a high electron-confinement effect and a very low hole-blocking barrier. Therefore, further research on the effect of the integration of the multiple EBL scheme is required.

CHAPTER 6 SUMMARY

For past decade, the semiconductor optoelectronic devices such as light-emitting diodes (LEDs), laser diodes (LDs), and photodiodes (PDs) have become of a great commercial success with their dramatically improved performance. Among the various candidate material systems for the semiconductor optoelectronic devices, the Group III-nitride semiconductor system is the most promising for many applications as they have direct- and wide-bandgap nature, high intrinsic carrier mobility, and the capability of forming heterostructures. With an increasing demand on the mass production of high-quality materials and device structures, metalorganic chemical vapor phase deposition (MOCVD) has been a dominant growth technology for both academic and industrial applications because of its versatility and scalability.

In the growth of the Group III-nitride materials, foreign substrates whose lattice constants and thermal expansion coefficients are mismatched to those of the Group III-nitride materials have been widely employed because of lack of the native substrates such as free-standing bulk GaN or AlN substrates. However, the use of various foreign and native substrates in the growth process introduces several technical challenges that are generally not observed in other Group III-V semiconductors such as InP- and GaAs-based materials whose lattice constant, thermal-expansion coefficient, and thermal conductivity are similar each other. Significantly different physical properties of the substrates over the epitaxial layers often lead to inconsistent growth results. Especially, the different thermal conductivity and the thickness of the substrates result in the different growing-surface temperature of the epitaxial layer. The growth temperature is a critical factor in determining most process parameters, such as the quality, growth rate, and the composition of the layer. However, predicting the growing-surface temperature is not very straightforward, because the surface temperature during the layer growth depends on numerous parameters, including the thermal conductivity of the substrate and the

surface heat loss by the forced convection. Therefore, it is important to estimate the actual surface temperature for the growth of high-quality and well-controlled Group III-nitride materials on different substrates with different growth conditions. We performed a finite element method (FEM) calculation on the commonly used substrates of sapphire, SiC, Si, bulk GaN, and bulk AlN substrates under the different growth temperatures and different carrier gases.

According to the calculation results, the sapphire substrate and the bulk AlN substrate with the same thickness is expected to exhibit more than 10 ^{o}C difference in the growing-surface temperature under the typical AlGaN growth temperature of 1150 ^{o}C. It is also predicted that the temperature difference will become larger when the thickness difference of the substrates increases. The surface-temperature difference at a typical InGaN growth temperature of 780 ^{o}C is also calculated to be around 10 ^{o}C, although the difference is reduced when N_2 is used as a carrier gas. These results indicate that the use of different substrates can lead to a significant discrepancy in the layer quality and the alloy composition. The influence of the different substrates on the growth results was also experimentally confirmed by growing AlN/AlGaN superlattice (SL) structures simultaneously on a bulk AlN substrate and an AlN/sapphire template/substrate. The strain status and the composition of the layers were measured by reciprocal space mapping (RSM) to confirm that the layers grown on different substrates shows alloy composition difference of 15%.

The Group III-nitride-based LEDs are one of the most successful and important optoelectronic devices. They are expected to replace conventional light sources in displays and general lighting applications in near future. One of the critical technical challenges for the LEDs to be competitive in terms of the performance and manufacturing cost is the efficiency droop. Several causes were suggested as an origin of the efficiency droop, but the carrier spill-over theory is widely accepted by the industrial as well as the academic researchers as the most convincing primary origin of the efficiency-droop problem. The insertion of a wide-bandgap AlGaN material between the active region and the *p*-type hole-injection layer as an electron-blocking layer (EBL) is the most common technique

to reduce the carrier spill-over phenomena. However, the electron-confinement by a typical AlGaN EBL (with x_{Al}~0.2) is not sufficiently effective to solve the efficiency-droop problem, especially because of the additional polarization effects caused by the AlGaN. Also, an AlGaN EBL may not be compatible with all visible LEDs (especially for wavelengths in the green-red region) because of its relatively high optimum growth temperature. Therefore, we proposed InAlN as an alternative high-quality EBL material for a higher electron-confinement effect with its lower growth temperature, wider bandgap, and lattice-matching capability to GaN.

To confirm the performance improvement by the InAlN EBL, high quality InAlN layers with indium composition of 19% were grown by using MOCVD to be employed in the blue LED structures. The electroluminescence (EL) measurement results obtained by an on-wafer probing on the 350×350 μm^2 devices showed that the LED with an $In_{0.19}Al_{0.81}N$ EBL exhibits higher absolute EL intensity than the LED without an EBL and the LED with a conventional $Al_{0.2}Ga_{0.8}N$ EBL. In the quantum-efficiency plot of the LEDs, the LED with an $In_{0.19}Al_{0.81}N$ EBL shows the smallest efficiency droop and the highest absolute quantum efficiency at the current density of 360 A/cm^2 compared to the LED with an $Al_{0.2}Ga_{0.8}N$ EBL and the LED without an EBL. The performance enhancement of the LED with an $In_{0.19}Al_{0.81}N$ EBL over the LED without an EBL at high current density was around 100%. This observation indicates that the $In_{0.19}Al_{0.81}N$ EBL provides more effective electron-confinement and smaller carrier spill-over current over the conventional $Al_{0.2}Ga_{0.8}N$ EBL.

However, the $In_{0.19}Al_{0.81}N$ EBL with a wide bandgap is predicted to cause a high hole-blocking barrier in the valence-band, and the hole-blocking barrier leads to low hole-injection efficiency into the active region. The deficiency of the hole concentration in the active region is reported to be another major origin of the efficiency droop. Therefore, the hole-blocking effect of the $In_{0.19}Al_{0.81}N$ EBL is analyzed quantitatively with a quantum-efficiency model. For an analysis, the hole-blocking effect of the $In_{0.19}Al_{0.81}N$ EBL is controlled by changing the thickness of the $In_{0.19}Al_{0.81}N$ EBL. LEDs with $In_{0.19}Al_{0.81}N$ EBLs with different thicknesses were grown and fabricated for a

quantum-efficiency comparison. In the quantum-efficiency curves, the peak efficiency of the LEDs is observed to be shifted toward higher current density with the increase of the EBL thickness, except for the LED with a 20 nm $In_{0.19}Al_{0.81}N$ EBL. Also, the LED with a 15 nm $In_{0.19}Al_{0.81}N$ EBL shows higher light output than the LED with a 20 nm $In_{0.19}Al_{0.81}N$ EBL. To explain this observation, the "ABC model" is extended to include a carrier spill-over and the limited hole transport effect. The extended model is applied to the quantum-efficiency curves to obtain the amount of the carrier spill-over and the carrier-density ratio between the electron density and the hole density. The model explained that the highest measured quantum efficiency of the LED with a 15 nm $In_{0.19}Al_{0.81}N$ EBL was a result of the high electron-confinement effect and the relatively low hole-blocking effect of the 15 nm thick EBL. The observation also suggests that the hole-blocking effect as well as the electron-confinement effect of the EBL should be considered to obtain higher light output and efficiency performance from LEDs operated at high current densities.

To reduce the hole-blocking effect and enhance the hole-injection efficiency of the EBL, a strain-engineered $In_xAl_{1-x}N$ EBL is proposed. An $In_xAl_{1-x}N$ EBL with higher indium composition induces the compressive strain and the piezoelectric field that compensates the spontaneous polarization field and reduces the band bending. As a result, the effective height of the electron-blocking barrier is maintained to be same while the height of the hole-blocking barrier is decreased under a forward bias condition. The reduced hole-blocking effect of the strain-engineered $In_xAl_{1-x}N$ EBL is confirmed by measuring the light output of the LEDs with $In_xAl_{1-x}N$ EBLs with different indium composition from 19% to 24%. According to the analysis by using the quantum-efficiency model, the LEDs with strain-engineered $In_xAl_{1-x}N$ EBLs show higher hole density than the LED with an $In_{0.19}Al_{0.81}N$ EBL while maintaining a high electron-confinement effect and a low spill-over current density. These analysis results support that the strain-engineering technique is effective in reducing the hole-blocking barrier of the $In_xAl_{1-x}N$ EBL. However, the light output of the LEDs with strain-engineered $In_xAl_{1-x}N$ EBLs is observed to be lower than that of the LED with a lattice-matching

$In_{0.19}Al_{0.81}N$ EBL. The current-voltage measurement results on the LEDs imply that the electrical performance of the strain-engineered $In_xAl_{1-x}N$ EBLs is degraded because of their lower growth temperature. Therefore, an alternative growth condition for the $In_xAl_{1-x}N$ EBL with high electrical properties is necessary to demonstrate the performance enhancement of the LED with a strain-engineered $In_xAl_{1-x}N$ EBL.

Another strategy for reducing the hole-blocking barrier and improving the hole-injection efficiency is the compositionally graded EBL. The compositional grading approach has been employed in many device applications to remove the sharp bandgap discontinuity at a heterojunction. The grading from the last InGaN QW to the $In_{0.19}Al_{0.81}N$ EBL will remove the sharp spike in the valence band at the active region - EBL interface, significantly reducing the height of the hole-blocking barrier. In the EL measurement results, the LEDs with graded $In_{0.19}Al_{0.81}N$ EBLs show higher light output than the LED with an abrupt $In_{0.19}Al_{0.81}N$ EBL in spite of the thicker EBL thickness. This result indicates that the compositional grading between the last QW and the $In_{0.19}Al_{0.81}N$ EBL delivers a dramatic enhancement in the hole-injection efficiency. However, the results on the enhanced luminous performance of the LED with a graded EBL is still preliminary, and a quantitative analysis on the effect of the compositionally graded $In_{0.19}Al_{0.81}N$ EBL on the hole injection and the electron-blocking effect should be performed.

Various EBL techniques introduced in this work can be combined each other for a further improvement in the LED performance. Employment of multiple EBL strategies may promote their advantages while minimizing the drawbacks of each technique. For example, the strain-engineered $In_xAl_{1-x}N$ EBL with higher indium composition can be combined with the compositional grading technique for a high electron-confinement effect and a very low hole-blocking barrier. Therefore, further researches on the effect of the integration of the multiple EBL scheme is required.

REFERENCES

[1] B. M. Shi *et al.*, "Transition between wurtzite and zinc-blende GaN: An effect of deposition condition of molecular-beam epitaxy," *Appl. Phys. Lett.*, vol. 89, pp. 151921-1-151921-3, Aug. 2006.

[2] T. Hashimoto *et al.*, "Phase selection of microcrystalline GaN synthesized in supercritical ammonia," *J. Crystal Growth*, vol. 291, no. 1, pp. 100-106, Apr. 2006.

[3] S. Nakamura and S.F. Chichibu, *Introduction to Nitride Semiconductor Blue Laser and Light Emitting Diodes*, New York: Taylor & Francis, 2000, pp. 105-150.

[4] J. Wu, W. Walukiewicz et al., "Universal bandgap bowing in group-III nitride alloys," *Solid State Comm.*, vol. 127, pp. 411-414, Aug. 2003.

[5] I. Vurgaftman *et al.*, "Band parameters for III–V compound semiconductors and their alloys," *J. Appl. Phys.*, vol. 89, no. 11, pp. 5815-5875, Feb. 2001.

[6] W. Walukiewicz *et al.*, "Optical properties and electronic structure of InN and In-rich group III-nitride alloys," *J. Crystal Growth*, vol. 269, no.1, pp. 119-127, Aug. 2004.

[7] R. Goldhahn *et al.*, "Detailed analysis of the dielectric function for wurtzite InN and In-rich InAlN alloys," *phys. stat. sol.* (a), vol. 203, no. 1, pp. 42-49, Jan. 2006.

[8] W. Terashima *et al.*, "Growth and Characterization of AlInN Ternary Alloys in Whole Composition Range and Fabrication of InN/AlInN Multiple Quantum Wells by RF Molecular Beam Epitaxy," *Jpn. J. Appl. Phys.*, vol. 45, no. 21, pp. L539-L542, May 2006.

[9] R. E. Jones *et al.*, "Band gap bowing parameter of $In_{1-x}Al_xN$," *J. Appl. Phys.*, vol. 104, pp. 123501-1-123501-6, Dec. 2008.

[10] K. Wang *et al.*, "Optical energies of AlInN epilayers," *J. Appl. Phys.*, vol. 103, pp. 073510-1-073510-3, Apr. 2008.

[11] J.-F. Carlin *et al.*, "Progresses in III-nitride distributed Bragg reflectors and microcavities using AlInN/GaN materials," *phys. stat. sol.* (b), vol. 242, no. 11, pp. 2326-2344, Aug. 2005.

[12] O. Ambacher *et al.*, "Two-dimensional electron gases induced by spontaneous and piezoelectric polarization charges in N- and Ga-face AlGaN/GaN heterostructures," *J. Appl. Phys.*, vol. 85, no. 6, pp. 3222-3233, Dec. 1999.

[13] R. R. Reddy and S. Anjaneyulu, "Analysis of the Moss and Ravindra relations," *phys. stat. sol.* (b), vol. 174, no. 2, pp. K91-K93, Dec. 1992.

[14] H. Morkoç *et al.*, "Large-band-gap SIC, Ill-V nitride, and II-VI ZnSe-based semiconductor device technologies," *J. Appl. Phys.*, vol. 76, no. 3, pp. 1363-1398, Mar. 1994.

[15] A. F. Wright, "Elastic properties of zinc-blende and wurtzite AlN, GaN, and InN," *J. Appl. Phys.*, vol. 82, no. 6, pp. 2833-2839, Jun. 1997.

[16] H. M. Manasevit, "Single crystal gallium arsenide on insulating substrates," *Appl. Phys. Lett.*, vol.12, no. 4, pp. 156-159, Feb. 1968.

[17] B. Gil, "MOVPE growth of nitrides," in *Group III Nitride Semiconductor Compound Physics and Applications*, Oxford, UK: Oxford Science Publications, 1998, pp. 72-74.

[18] V. S. Ban, "Mass Spectrometric Studies of Vapor-Phase Crystal Growth," *J. Electrochem. Soc.*, vol. 119, no. 6, pp. 761-765, Jun. 1972.

[19] D. R. Gaskell, *Introduction to the Thermodynamics of Materials*. 3rd ed. New York: Tayor & Francis, 1995.

[20] H. Grothe and F. G. Boebel, "In-situ control of Ga(A1)As MBE layers by pyrometric interferometry," *J. Crystal Growth*, vol. 127, no. 1-4, pp. 1010-1013, Feb. 1993.

[21] LayTec AG., Berlin, Germany. *True Temperature measurements: the physical background* [Online]. Available:

http://www.laytec.de/fileadmin/bilder_dateien/pdf/Info_Notes/Info_Note_True_Temperature_20101216.pdf

[22] M. Belousov *et al.*, "In situ metrology advances in MOCVD growth of GaN-based materials," *J. Crystal Growth*, vol. 272, no. 1-4, pp. 94-99, Dec. 2004.

[23] R. Steins *et al.*, "Use of SiC band gap temperature dependence for absolute calibration of emissivity corrected pyrometers in III-nitride MOVPE," *J. Crystal Growth*, vol. 272, no. 1-4, pp. 81-86, Dec. 2004.

[24] J. R. Creighton *et al.*, "Emissivity-correcting near-UV pyrometry for group-III nitride OMVPE," *J. Crystal Growth*, vol. 287, no. 2, pp. 572-576, Jan. 2006.

[25] J. R. Creighton *et al.*, "Emissivity-correcting mid-infrared pyrometry for group-III nitride MOCVD temperature measurement and control," *J. Crystal Growth*, vol. 310, no. 6, pp. 1062-1068, Mar. 2008.

[26] V. Swaminathan and A. T. Macrander, *Materials Aspects of GaAs and InP Based Structures*. Englewood Cliffs, NJ: Prentice Hall, 1991, pp. 281-321.

[27] D. Baselt, "The Tip-Sample Interaction in Atomic Force Microscopy and Its Implications for Biological Applications," Ph.D. dissertation, Division of Chemistry and Chemical Engineering, Caltech., Pasadena, CA, 1993.

[28] *Dimension 3000 Scanning Probe Microscope Instruction Manual*, Digital Instruments, Santa Barbara, CA, 1994.

[29] W. Hageman *et al.*, "Growth of AIN on Etched 6H-SiC(0001) Substrates via MOCVD, " *phys. stat. sol.* (a), vol. 188, no. 2, pp. 783-787, Nov. 2001.

[30] C. S. Kim *et al.*, "Mg fluctuation in p-GaN layers and its effects on InGaN/GaN blue light-emitting diodes dependent on p-GaN growth temperature," *J. Electron. Mater.*, vol. 33, no. 5, pp. 445-449, May 2004.

[31] Z. Y. Fan *et al.*, "High temperature growth of AlN by plasma-enhanced molecular beam epitaxy," *Mater. Sci. Eng.* B, vol. 67, no. 1-2, pp. 80-87, Dec. 1999.

[32] Y. Ohba and A. Hatano, "Growth of High-Quality AlN and AlN/GaN/AlN Heterostructure on Sapphire Substrate," *Jpn. J. Appl. Phys.*, vol. 35, no. 8B, pp. L1013-L1015, Aug. 1996.

[33] S. M. Bedair *et al.*, "Growth and characterization of In-based nitride compounds," *J. Crystal Growth*, vol. 178, no. 1-2, pp. 32-44, Jun. 1997.

[34] N. B. Vargaftik, Y. K. Vinogradov, V. S. Yargin, *Handbook of Physical Properties of Liquids and Gases*. New York: Begell House, 1996.

[35] Kyocera Corp., Kyoto, Japan. *Single Crystal Sapphire* [Online]. Available: http://global.kyocera.com/prdct/fc/product/pdf/s_c_sapphire.pdf

[36] G. A. Slack *et al.*, "The intrinsic thermal conductivity of AIN," *J. Phys. Chem. Solids*, vol. 48, no. 7, pp. 641-647, Sept. 1987.

[37] J. F. Muth *et al.*, "Absorption Coefficient and Refractive Index of GaN, AIN and AlGaN Alloys," *MRS Internet J. Nitride Semicond. Res.*, vol. 4S1, pp. U510-U515, 1999.

[38] W. Smetana and R. Reicher, "A new measuring method to determine material spectral emissivity," *Meas. Sci. Technol.*, vol. 9, no. 5, pp. 797-802, Jan. 1998.

[39] M. D. Kamatagi *et al.*, "Thermal conductivity of GaN," *Diamond Relat. Mater.*, vol. 16, no. 1, pp. 98-106, May 2007.

[40] M. Hao *et al.*, "Infrared properties of bulk GaN," *Appl. Phys. Lett.*, vol.74, no. 19, pp. 2788-2790, Mar. 1999.

[41] A. Chatterjee *et al.*, "Junction Temperature Simulation of Gallium Nitride Green Light Emitting Diodes Using COMSOL," *Proceedings of the COMSOL Conference 2007*, Boston, MA, 2007.

[42] O. Nilsson *et al.*, "Determination of the thermal diffusivity and conductivity of monocrystalline silicon carbide (300-2300K)," *High Temp.-High Pressures*, vol. 29, no. 1, pp. 73-79, Nov. 1997.

[43] M. Namba, "Optical properties of silicon carbide," *J. Phys. Chem. Solids*, vol. 2, no. 4, pp. 339-340, Feb. 1957.

[44] C. P. Cagran *et al.*, "Temperature-Resolved Infrared Spectral Emissivity of SiC and Pt–10Rh for Temperatures up to 900°C," *Int. J. Thermophys.*, vol. 28, no. 2, pp. 581-597, Apr. 2007.

[45] R. Hull, *Properties of Crystalline Silicon.* London, UK: INSPEC, 1999.

[46] Tydex, St. Petersburg, Russia, *Silicon* [Online]. Available: http://www.tydexoptics.com/pdf/Si.pdf

[47] T. Sato, "Spectral Emissivity of Silicon," *Jpn. J. Appl. Phys.*, vol. 6, no. 3, pp. 339-347, Mar. 1967.

[48] J. H. Lienhard IV, and J. H. Lienhard V, *A Heat Transfer Textbook* 3rd ed. Cambridge: Philogiston Press, 2008.

[49] A. Koukitu *et al.*, "Thermodynamic study on the role of hydrogen during the MOVPE growth of group III nitrides," *J. Crystal Growth*, vol. 197, no. 1-2, pp. 99-105, Feb. 1999.

[50] The AlN wafers are prepared by Prof. Zlatko Sitar's Group at North Carolina State University.

[51] T. Mukai *et al.*, "Characteristics of InGaN-Based UV/Blue/Green/Amber/Red Light-Emitting Diodes," *Jpn. J. Appl. Phys.*, vol. 38, no. 7A, pp. 3976-3981, Jul. 1999.

[52] A. Y. Kim *et al.*, "Performance of High-Power AlInGaN Light Emitting Diodes," *phys. stat. sol*. (a), vol. 188, no. 1, pp. 15-21, Nov. 2001.

[53] Y. C. Shen *et al.*, "Auger recombination in InGaN measured by photoluminescence," *Appl. Phys. Lett.*, vol. 91, pp. 141101-1-141101-3, Oct. 2007.

[54] M. Maier *et al.*, "Reduced nonthermal rollover of wide-well GaInN light-emitting diodes," *Appl. Phys. Lett.*, vol. 94, pp. 041103-1-041103-3, Jan. 2009.

[55] K. T. Delaney *et al.*, "Auger recombination rates in nitrides from first principles," *Appl. Phys. Lett.*, vol. 94, pp. 191109-1-191109-3, May 2009.

[56] I. V. Rozhansky and D. A. Zakheim, "Analysis of processes limiting quantum efficiency of AlGaInN LEDs at high pumping," *phys. stat. sol.* (a) vol. 204, no. 1, pp. 227-230, Jan. 2007.

[57] M.-H. Kim *et al.*, "Origin of efficiency droop in GaN-based light-emitting diodes," *Appl. Phys. Lett.*, vol. 91, pp. 183507-1-183507-3, Oct. 2007.

[58] J. P. Liu *et al.*, "Barrier effect on hole transport and carrier distribution in InGaN/GaN multiple quantum well visible light-emitting diodes," *Appl. Phys. Lett.*, vol. 93, pp. 021102-1-021102-3, Jul. 2008.

[59] X. Ni *et al.*, "Reduction of efficiency droop in InGaN light emitting diodes by coupled quantum wells," *Appl. Phys. Lett.*, vol. 93, pp. 171113-1-171113-3, Oct. 2008.

[60] W. Lee *et al.*, "Effect of thermal annealing induced by p-type layer growth on blue and green LED performance," *J. Crystal Growth*, vol. 287, no. 2, pp. 577-581, Jan. 2006.

[61] J.-F. Carlin and M. Ilegems, "High-quality AlInN for high index contrast Bragg mirrors lattice matched to GaN," *Appl. Phys. Lett.*, vol. 83, no. 4, pp. 668-670, May 2003.

[62] J. Xie *et al.*, "High electron mobility in nearly lattice-matched AlInN/AlN/GaN heterostructure field effect transistors," *Appl. Phys. Lett.*, vol. 91, pp. 132116-1-132116-3, Sept. 2007.

[63] S. Choi *et al.*, "Threshold voltage control of InAlN/GaN heterostructure field-effect transistors for depletion- and enhancement-mode operation," *Appl. Phys. Lett.*, vol. 96, pp. 243506-1-243506-3, Jun. 2010.

[64] A. Castiglia *et al.*, "$Al_{0.83}In_{0.17}N$ lattice-matched to GaN used as an optical blocking layer in GaN-based edge emitting lasers," *Appl. Phys. Lett.*, vol. 94, pp. 193506-1-193506-3, May 2009.

[65] T. S. Oh *et al.*, "Growth and properties of Al-rich $In_xAl_{1-x}N$ ternary alloy grown on GaN template by metalorganic chemical vapour deposition," *J. Phys. D*, vol. 41, no. 9, pp. 095402.1-5, Apr. 2008.

[66] Q. Guo *et al.*, "Thermal stability of indium nitride single crystal films," *J. Appl. Phys.*, vol. 73, no. 11, pp. 7969-7971, Feb. 1993.

[67] K. Kishiro *et al.*, "Intersubband transition in $(GaN)_m/(AlN)_n$ superlattices in the wavelength range from 1.08 to 1.61 μm," *Appl. Phys. Lett.*, vol. 81, no. 7, pp. 1234-1236, Jun. 2002.

[68] K. Wang *et al.*, "Conduction band offset at the InN/GaN heterojunction," *Appl. Phys. Lett.*, vol. 91, pp. 232117-1-232117-2, Dec. 2007.

[69] J.-H. Ryou *et al.*, "Control of Quantum-Confined Stark Effect in InGaN-Based Quantum Wells," *IEEE J. Sel. Topics. Quantum Electron.*, vol. 15, no. 4, pp. 1080-1091, May 2009.

[70] S.-H. Han *et el.*, "Effect of electron blocking layer on efficiency droop in InGaN/GaN multiple quantum well light-emitting diodes," *Appl. Phys. Lett.*, vol. 94, pp. 231123-1-231123-3, Jun. 2009.

[71] A. M. Fischer *et al.*, "Effect of Growth Temperature on the Electron-Blocking Performance of InAlN Layers in Green Emitting Diodes," *Appl. Phys. Express*, vol. 3, pp. 031003-1-031003-3, Feb. 2010.

[72] Y. C. Shen *et al.*, "Optical cavity effects in InGaN/GaN quantum-well-heterostructure flip-chip light-emitting diodes," *Appl. Phys. Lett.*, vol. 82, pp. 2221-2223, Feb. 2003.

[73] Q. Dai *et al*., "Internal quantum efficiency and nonradiative recombination coefficient of GaInN/GaN multiple quantum wells with different dislocation densities," *Appl. Phys. Lett.* vol. 94, pp. 111109-1-111109-3, Mar. 2009.

[74] S.-C. Ling *et al.*, "Low efficiency droop in blue-green m-plane InGaN/GaN light emitting diodes," *Appl. Phys. Lett.* vol. 96, pp. 231101-1-231101-3, Jun. 2010.

[75] C. H. Wang *et al.*, "Hole injection and efficiency droop improvement in InGaN/GaN light-emitting diodes by band-engineered electron blocking layer," *Appl. Phys. Lett.* vol. 97, pp. 261103-1-261103-3, Dec. 2010.

[76] Y.-K. Kuo *et al.*, "Effect of P-Type Last Barrier on Efficiency Droop of Blue InGaN Light-Emitting Diodes," *IEEE J. Quantum Electron.* vol. 46, pp. 1214-1216, Aug. 2010.

[77] J. P. Bergman *et al*., "Temperature dependence of the minority carrier lifetime in GaAs/AlGaAs double heterostructures," *J. Appl. Phys.* vol. 78, no. 7, pp. 4808-4810, Jun. 1995.

[78] R. Olshansky *et al*., "Measurement of radiative and nonradiative recombination rates in InGaAsP and AlGaAs light sources," *IEEE J. Quantum Electron.* vol. 20, no. 8, pp. 838-854, Aug. 1984.

[79] X. Li *et al.*, "Effect of carrier spillover and Auger recombination on the efficiency droop in InGaN-based blue LED," *Superlattices Microstruct.*, vol. 47, no. 1, pp. 118-122, Jan. 2010.

[80] S. Jursenas *et al.*, "Luminescence decay in highly excited GaN grown by hydride vapor-phase epitaxy," *Appl. Phys. Lett.*, vol. 83, no. 1, pp. 66-68, May 2003.

[81] Ü. Özgür *et al.*, "GaN-Based Light-Emitting Diodes: Efficiency at High Injection Levels," *Proc. IEEE*, vol. 98, no. 7, pp. 1180-1196, May 2010.

[82] S. Choi *et al.*, "Threshold voltage control of InAlN/GaN heterostructure field-effect transistors for depletion- and enhancement-mode operation," *Appl. Phys. Lett.* vol. 96, pp. 243506-1-243506-3, Jun. 2010.

[83] T. Chung *et al.*, "Device operation of InGaN heterojunction bipolar transistors with a graded emitter-base design," *Appl. Phys. Lett.*, vol. 88, pp. 183501-1-183501-3, May 2006.

[84] A.T. Cheng *et al.*, "DC characteristics improvement of recessed gate GaN-based HFETs grown by MOCVD," *J. Crystal Growth*, vol. 298, pp. 848-851, Jan. 2007.

[85] Jianping Liu *et al*., "Performance characteristics of InAlGaN laser diodes depending on electron blocking layer and waveguiding layer design grown by metalorganic chemical vapor deposition," *J. Crystal Growth*, vol. 315, pp. 272-277, Jan. 2011.